Machinability of Single-phase Materials

Surface integrity and tool wear analysis

Olsson, Mike

2021

Document Version:
Publisher's PDF, also known as Version of record

Machinability of Single-phase Materials

Surface integrity and tool wear analysis

MIKE OLSSON
FACULTY OF ENGINEERING | LUND UNIVERSITY

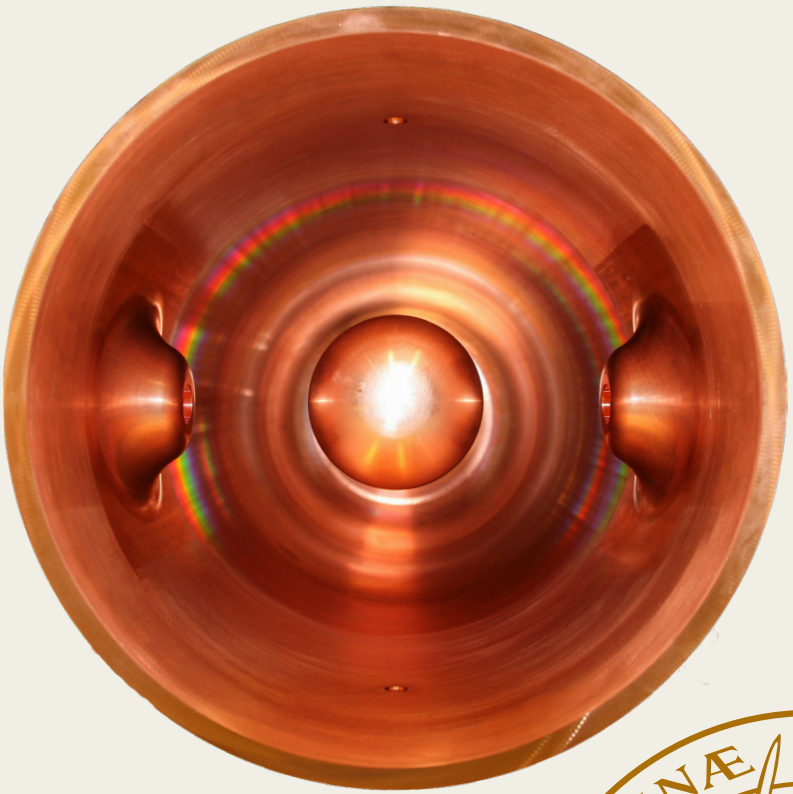

Machinability of Single-phase Materials

Surface integrity and tool wear analysis

Mike Olsson

LUND
UNIVERSITY

DOCTORAL DISSERTATION

by due permission of the Faculty of Engineering, Lund University, Sweden.
To be defended in lecture hall KC:A, KC-building, LTH, Naturvetarvägen 14 /Sölvegatan 39 A-C, Lund. 2021-06-11 at 09.00.

Faculty opponent
Associate Professor Giuliano Bissacco

Technical University of Denmark (DTU), Department of Mechanical Engineering,
Lyngby, Denmark

Organization	Document name
Division of Production and Materials Engineering Faculty of Engineering LUND UNIVERSITY	DOCTORAL DISSERTATION
	Date of issue 20210611
Author Mike Olsson	Sponsoring organization

Title and subtitle Machinability of single-phase materials – Surface integrity and tool wear analysis

Abstract:

The quality and performance of products are particularly important in sectors such as research facilities and in the nuclear, military and space industries. These sectors make use of high-performance materials that are uncommon in other contexts and therefore place high requirements on personnel, machines and tools. While tool manufacturers have readily available tool selection guides and cutting data recommendations for a wide range of materials, relying on many years of research, little information is available when selecting tools and cutting parameters for machining less common or exotic materials. Consequently, only a few highly specialized companies manufacture components using such materials.

The aim of this dissertation is to create a knowledge base on machining single-phase materials, specifically oxygen-free copper, niobium, and tungsten. It builds on an understanding of the difficulties in achieving the required surface quality and suggests useful tooling solutions and cutting parameters, as exemplified for a longitudinal turning machining operation. Different aspects of surface integrity such as subsurface deformation, surface defects and damage are discussed. Such analysis relied on extraction, polishing, and examination of the machined samples with nanoindentation and SEM microscopy.

Screening tests of several different tooling solutions for niobium and tungsten were also performed to evaluate machining performance and tool wear under different cutting conditions. Tool wear mechanisms were evaluated with SEM and TEM microscopy and further compared using the diffusion couple sample technique.

The results of the research presented in this dissertation highlight the difficulties in achieving the targeted surface quality and selecting tooling solutions for these single-phase materials, while also highlighting potential successful pathways for the machining processes. These results can be used to further evaluate tool selection or to develop new tooling solutions to improve the surface quality of the finished product at a reasonable performance and therefore cost.

Key words: Machinability, Oxygen-free copper, Niobium, Tungsten, Surface integrity, Tool wear

Classification system and/or index terms (if any)

Supplementary bibliographical information		**Language:** English
ISSN and key title		ISBN 978-91-7895-863-4 (print) ISBN 978-91-7895-864-1 (pdf)
Recipient's notes	**Number of pages** 104	Price
	Security classification	

Signature  Date 2021-04-16

Machinability of Single-phase Materials

Surface integrity and tool wear analysis

Mike Olsson

LUND
UNIVERSITY

Coverphoto by Mike Olsson

Faculty of Engineering
Department of Production and Materials Engineering

ISBN 978-91-7895-863-4 (print)
ISBN 978-91-7895-864-1 (pdf)

Printed in Sweden by Media-Tryck, Lund University
Lund 2021

Abstract

The quality and performance of products are particularly important in sectors such as research facilities and in the nuclear, military and space industries. These sectors make use of high-performance materials that are uncommon in other contexts and therefore place high requirements on personnel, machines and tools. While tool manufacturers have readily available tool selection guides and cutting data recommendations for a wide range of materials, relying on many years of research, little information is available when selecting tools and cutting parameters for machining less common or exotic materials. Consequently, only a few highly specialized companies manufacture components using such materials.

The aim of this dissertation is to create a knowledge base on machining single-phase materials, specifically oxygen-free copper, niobium, and tungsten. It builds on an understanding of the difficulties in achieving the required surface quality and suggests useful tooling solutions and cutting parameters, as exemplified for a longitudinal turning machining operation. Different aspects of surface integrity such as subsurface deformation, surface defects and damage are discussed. Such analysis relied on extraction, polishing, and examination of the machined samples with nanoindentation and SEM microscopy.

Screening tests of several different tooling solutions for niobium and tungsten were also performed to evaluate machining performance and tool wear under different cutting conditions. Tool wear mechanisms were evaluated with SEM and TEM microscopy and further compared using the diffusion couple sample technique.

The results of the research presented in this dissertation highlight the difficulties in achieving the targeted surface quality and selecting tooling solutions for these single-phase materials, while also highlighting potential successful pathways for the machining processes. These results can be used to further evaluate tool selection or to develop new tooling solutions to improve the surface quality of the finished product at a reasonable performance and therefore cost.

Keywords:

Machinability, Niobium, Tungsten, Oxygen-free copper, Surface integrity, Tool wear

Populärvetenskaplig sammanfattning

Sverige har historiskt sett varit en stark industrination under modern tid. Men under 2000-talet har sysselsättningen i svensk tillverkningsindustri och gruvnäring minskat från cirka 720.000 personer år 2000 [1] till cirka 480.000 personer år 2019 [2]. Men svensk industri utgör än idag en viktig funktion inom Sveriges ekonomi och är den sektor som bidrar mest till Sveriges BNP med 15 % av det totala värdet [3].

Med höga krav på kvalité och prestanda på en produkt ställer det även höga krav på funktionen av produkten. Dessa krav är oftast av särskild betydelse inom mer avancerade sektorer som forskningsanläggningar, rymd-, militär- och kärnkraftindustri samt för medicintekniska applikationer. Utvecklingen av nya och bättre material drivs ofta framåt utifrån kraven inom dessa sektorer, samtidigt som dessa avancerade material inte används i lika stor omfattning inom andra sektorer. När komponenter tillverkas i avancerade material, ställs det högre krav på både utrustning och verktyg samtidigt som personalens kompetensbehov ökar. Verktygsrekommendationer och skärparametrar går att finna i leverantörernas databaser för de flesta konventionella materialen. Databaserna bygger på flera års forskning och tester vid industrin och akademin. I detta arbete genomförs experimentella studier av olika verktygs- och materialkombinationer för att täcka in de väsentligaste applikationsområdena. Med hänsyn till det omfattande arbetet är databaserna begränsade till att omfatta de mest förkommande materialtyperna. Rekommendationerna är bristfälliga för mer nischade material, vilket leder till att mindre förtag undviker att offerera tillverkning av sådana produkter och därmed begränsas tillverkningen till ett fåtal ytterst specialiserade företag.

Målet med arbetet som presenteras i denna avhandling är att finna lämpliga verktyg och skärparametrar för att uppnå de ytkrav som ställs på en produkt vid bearbetning av primärt oxidfri koppar, niob och volfram.

Resultaten i avhandlingen behandlar uppkomsten av ytdefekter och problematiken kring spån- och gradbildning, val av skärparametrar för att uppnå en viss ytkvalité, samt val av lämpliga verktyg för att minimera verktygsförslitningen vid bearbetning av enfasiga material. Resultaten skall ligga till grund för vidare utvärdering av andra lämpliga verktyg, förbättrad verktygslivslängd samt ytkvalité på slutprodukten. Kunskapen kan leda till att fler tillverkningsföretag har möjlighet att ge offerter och producera komponenter i nämnda svårbearbetade material. Sammantaget skall arbetet bidra till ett kunskapslyft för företagen och där produktionskostnaden kan reduceras och bestämmas på förhand med en högre säkerhet.

Nyckelord:

Skärbarhet, Oxidfri koppar, Niob, Volfram, Ytintegritet, Verktygsförslitning

Acknowledgement

When I look back to when I was a master student in the third grade, there was a seminar to present the different topics of specializations, which was later available to choose for the next two years. I remember that I was somehow fascinating about how someone was able to talk so much about metal chips. Even though the talk caught my attention I was never intended to proceed with any courses related to it, I mean how interesting could it be? Well here I am, several years later I have summarized my research I have made the past years, which also includes talking about metal chips. However, now I understand that the field of metal cutting is a very wide field that includes many different aspects and not only metal chips. I must say that it has been very fascinating to dig deeper into the field that I sometimes had to be stopped and start write up on all the information that had been extracted.

First of all I would like to thank my supervisor Dr. Volodymyr Bushlya, without his support and mentorship I doubt that I would have gone the whole way to write a PhD dissertation. I also would like to express my gratitude to Prof. Jan-Eric Ståhl, who somehow tricked me into the field of metal cutting even though his first talk about metal chips did not fully convince me. I think that they will agree upon about the PhD journey that I have made, have somehow not been the most straightforward but I thank them both for letting this happen.

I would like to thank my co-supervisor John Weisend, adjunct Prof. at the Division of Production and Materials Engineering, Lund University and Group Leader Specialized Technical Service at European Spallation Source (ESS). Your expertise and support related to accelerator technology have been very appreciated throughout this research.

I would like to thank my colleagues at the Division of Production and Materials Engineering, Lund University. I would like to give a special thank you to Ville Akujärvi, Filip Lenrick and Henrik Persson for their help and contribution to the experiments made and further analysis. I would also like to express my gratitude to all the co-authors that have contributed to papers.

My research would not have been possible without the financial support from Produktion2030, Vinnova, Tillväxtverket and the Sustainable Production Initiative Cooperation between Chalmers and Lund University. I would also like to acknowledge the support from Seco Tools AB, Fagersta.

Finally, I would like to give a special thanks to my family and friends for their valuable support throughout this PhD journey.

Appended Publications

This dissertation is based on the work presented in the following publications. The publications will be referred to in the text with Roman numerals.

I *Effect of feed on sub-surface deformation and yield strength of oxygen-free pitch copper in machining*
Olsson M., Bushlya V., Zhou J., Ståhl J-E.
Procedia CIRP, 45, (2016) 103 – 106

II *FE simulation and experimental verification of side-flow and burr formation in machining of oxygen-free copper*
Olsson M., Persson H., Agmell M., Bushlya V., Ståhl J-E.
Procedia CIRP, 72, (2018) 1427 – 1432

III *Surface roughness and sub-surface deformation measurements in machining of niobium*
Olsson M., Persson H., Bushlya V., Ståhl J-E.
Procedia CIRP, 71, (2018) 413 – 417

IV *Study of wear mechanisms of cemented carbide tools during machining of single-phase niobium*
Olsson M., Lenrick F., M´Saoubi R., Larsson H., Markström A., Petrusha I., Ståhl J-E., Bushlya V.
Wear, 450-451, (2020) 203244

V *Evaluation of tool wear mechanisms and tool performance in machining single-phase tungsten*
Olsson M., Bushlya V., Lenrick F., Ståhl J-E.
International Journal of Refractory Metals and Hard Materials, 94, (2021) 105379

VI *Cryogenic and hybrid induction-assisted machining strategies as alternatives for conventional machining of refractory tungsten and niobium*
Olsson M., Akujärvi V., Bushlya V., Ståhl J-E.
International Journal of Refractory Metals and Hard Materials, 97, (2021) 105520

Authors Contribution

I Olsson performed the experimental tests and wrote a major part of the work. Zhou assisted with nanoindentation. Bushlya performed SEM imaging, planning and writing. Ståhl planned the experimental work.

II Olsson performed the experimental tests and wrote a major part of the work. Persson performed experimental tests including high speed filming. Agmell contributed with FE-simulations and writing. Bushlya planned and contributed to writing of the final paper.

III Olsson planned, performed experimental tests, nanoindentation and wrote a major part of the work. Persson assisted in the experimental tests. Bushlya performed SEM imaging, planned and contributed to writing of the final paper.

IV Olsson planned, performed experimental tests, assisted in SEM and TEM imaging and contributed to the writing. Lenrick performed TEM imaging and contributed to writing of the paper. M´Saoubi contributed to writing and thermal imaging experiment. Larsson and Markström performed Thermo Calc and Dictra calculations and writing. Petrusha performed diffusion couples experiment and writing. Bushlya performed SEM imaging, planned and contributed to writing of the paper.

V Olsson planned, performed experimental tests, assisted in SEM and TEM imaging and wrote a major part of the work. Lenrick performed TEM imaging. Bushlya performed SEM imaging, planned and contributed to writing of the final paper.

VI Olsson planned, performed experimental tests, assisted in SEM imaging and wrote a major part of the work. Akujärvi assisted in the experimental tests with the induction heating system, performed Comsol Multiphysics simulations and contributed to writing. Bushlya performed SEM imaging, planned and contributed to writing of the final paper.

List of symbols and abbrevations

a_p	Depth of cut	mm
b_1	Theoretical chip width	mm
BUE	Built-up edge	-
BUL	Built-up layer	-
CAM	Computer aided manufacturing	-
CC	Cemented carbide	-
Cr	Cutting resistance	N/mm^2
CVD	Chemical vapour deposition	-
DBTT	Ductile to brittle transistion temperature	-
DGM	Driving force	N
DRX	Dynamic recrystallization	-
f	Feed	mm/rev
F_c	Main cutting force	N
F_f	Feed force	N
F_p	Passive force	N
FE	Finite element	-
FIB	Focused ion beam	-
h_1	Theoretical chip thickness	mm
HAADF	High-angle annular dark-field	-
HP	High pressure (coolant condition)	-
HP-HT	High pressure – high temperature	-
HSS	High-speed steel	-
IAM	Induction heated assistant machining	-
l	Cutting length	m
l_{clc}	Critical contact length	mm
L_m	Workpiece length	mm
LN_2	Liquid nitrogen	-
MRR	Metal removing rate	cm^3/min
Nb	Niobium	-
OFC	Oxygen-free copper	-
P_c	Cutting power from the primary cutting force	W
cBN	cubic boron nitride	-
PCD	Polycrystalline diamond	-
PVD	Physical vapour deposition	-
r	Nose radius	mm
r_β	Edge radius	µm
R_a	Arithmetic mean surface roughness	µm
R_{max} (R_t)	Maximum peak-to-valley surface roughness	µm
$R_{p\ 0.2}$	Yield stress at 0.2 % plastic deformation	MPa
R_z	Mean peak-to-valley surface roughness	µm
SEM	Scanning electron microscope	-
SI	Surface integrity	-
SPM	Single-phase metals	-
STEM	Scanning transmission electron microscopy	-
TEM	Transmission electron microscope	-
TPL	Tool protective layer	-
VB_{max}	Tool life criterion	µm
v_c	Cutting speed	m/min
W	Tungsten	-

XEDS	Energy-dispersive x-ray spectroscopy	-
ε_I	Width of the deformation zone in zone I	mm
ε_{II}	Width of the deformation zone in zone II	mm
ε_{III}	Width of the deformation zone in zone III	mm
α	Clearance angle	°
β	Wedge angle	°
ε	Included angle	°
κ	Major cutting edge angle	°
κ_b	Minor cutting edge angle	°
λ	Inclination angle	°
γ	Rake angle	°

Table of Contents

1 Introduction

Ever since the Industrial Revolution, industrial production has affected our lives in many ways. It has been estimated that over 80 % of the products manufactured today have been machined in some way before completion [4]. The total global machine tool consumption in 2019 was estimated to be approximately US$ 82.1B (metal cutting and forming) [5], with the EU's portion being around 36 % [6].

The machining process can be defined as material removal from a workpiece by plastic deformation with a cutting tool, in the form of a chip [7]. The constant development of new products with improved materials and production processes puts high requirements on the tooling industry. Ongoing research in the field of metal cutting is required to reduce the cost of production requirements by promoting longer tool life, and so meeting the requirements of end users.

1.1 Background and Objective

Research in machining initially focused simply on the basic ability to use different techniques to manufacture specific components. As knowledge of the area grew, the focus was broadened to include cost reduction and higher product quality after machining. These are still major concerns, for technological advances, including new machining methods, new tools, and new materials, pose new demands requiring new research.

A typical material subjected to machining is normally an alloy containing different elements, with the exact composition dependent on the mechanical properties required by the design and manufacturing requirements of the product. Single-phase metals (SPM) are less commonly used because they offer limited advantages in terms of mechanical properties and production routines. Their use is driven by special needs for properties that are not only related to mechanical properties. Metals are normally available in polycrystalline form, often relaying on certain strengthening mechanisms (e.g. solute strengthening, phase transformations, precipitation, etc.). In case of SPM, the metals are devoid of such strengthening mechanisms thus making the metal more ductile and less strong, yet this deficiency is compensated by unique thermal, physical, chemical and other properties.

Technological advances have resulted in the construction of large infrastructure such as synchrotrons, neutron facilities, and fusion reactor testing facilities. SPM materials have a central role in the functioning of these facilities and the requirements for tolerances and surface quality are high. For example, copper and niobium are used in the construction of accelerator components and magnets and tungsten is used as a target material for neutrons and to shield components from extreme temperatures. Copper is also being evaluated as a suitable metal for constructing canisters intended for long-term storage of spent nuclear waste deep in bedrock for thousands of years.

SPM metals were first worked by humans hundreds of years ago or, in the case of copper, thousands of years ago. Copper and niobium are highly ductile in a single-phase state and present similar challenges in machinability. Tungsten however, is the opposite: it is brittle in the single-phase state, and so presents different challenges in terms of machinability. Despite a long presence of these metals in our lives, only limited research has been conducted on the machinability of all three metals, and especially niobium and tungsten, which makes it difficult to find recommendations for suitable tools and cutting data. The objective of the research reported in this dissertation is to investigate conventional cutting tools and find suitable cutting parameters for turning single-phase copper, niobium, and tungsten. Subsequently, a search for alternative methods was pursued if conventional methods were not satisfactory. In the process of testing different tooling solutions, the focus has been on evaluating the surface integrity of the machined surface to achieve the high quality required for accelerator components. Tool wear and wear mechanisms have also been evaluated to find suitable tools for the machining operations and so reduce production costs.

1.2 Hypotheses

The following hypotheses, based on previous publications, were established for this research study:

- Adequate design of machining strategy will facilitate meeting the high demands on material properties and surface integrity when machining single-phase metals.
- Available tooling solutions will make it possible to achieve acceptable machinability and wear rates, as defined by component manufacturers.
- Novel machining and coolant approaches offer better control over machining outcomes (quality and performance).

1.3 Research Questions

Based on the hypotheses the following research questions were formulated:

RQ1. Can the parameter requirements related to surface integrity of components for radiation research facilities be met with conventional machining?

RQ2. Is there a conventional machining strategy that allows refractory metals to be machined productively?

RQ3. Can alternative machining strategies (e.g., advanced tooling, advanced cooling, and hybrid processes) overcome the limitations of conventional machining?

1.4 Scope and Limitations

A machining process includes several different input variables, including workpiece material, tooling solutions, and cutting parameters. Of the almost infinite possible combinations of these parameters, only a limited number can be studied. Thus, only a limited range of selected machining parameters is discussed and validated in this dissertation. The following limitations were accepted in this research:

- A machining process can consist of several different machining operations. However, only longitudinal turning operations have been considered .
- The research has been limited to machining three different workpiece materials of high purity: oxygen-free copper, niobium, and tungsten.

1.5 Methodology

The methodologies used in the different studies reported on in this dissertation varied slightly depending on the research needed for the specific materials. These materials were selected for study based on identified demand for components manufactured using these specific materials at research facilities such as MAX IV and ESS in Lund. There was a lack of local competence to manufacture components with such SPMs. Contact with tool manufacturers confirmed the lack of information when machining Nb and W, for which no tooling solutions or cutting parameters recommendations are available.

Once the research problems had been established, a thorough literature review was conducted, combined with discussions with persons in key positions at different research facilities. This was combined with study visits to the following research facilities: CERN, MAX IV, ESS, XFEL, FAIR, ITER, SNS, Diamond, and Fermilab. In some cases, study visits took place at the same time as conferences and workshops. Discussions were held with participating companies related to building large research infrastructures and component manufacturing. This was done to improve the understanding of the problems and to investigate whether the hypotheses related to the problems had previously been explored or published.

An empirical (experimental) approach was selected for the trajectory of research within the dissertation. Starting from the *a priori* and *a posteriori* knowledge types of Immanuel Kant [8], it is possible to argue that *a priori* knowledge can be synthesized from a sufficiently large number of facts through inductive reasoning to create a general truth. Obviously, arriving at a general truth on the subject of this dissertation – machining single-phase materials – is highly desirable. However, the results of the literature analysis, interviews, and site visits confirmed a severe lack of factual data about machining SPM, which makes the synthesis of a coherent knowledge base very difficult. Instead, the experimental studies conducted in this dissertation are viewed as concrete steps on the way to building the empirical base needed for successful synthesis by the next generation of researchers.

Experimental studies were performed in a laboratory environment, and in some cases complemented by work at companies. The selection of tooling solutions and cutting parameters influencing the machining process was investigated in the laboratory. Screening experiments were used in the initial tests during machining Nb and W to minimize the number of tests. According to Montgomery [9], screening experiments are a part of fractional factorial design, which is used to identify the factors that have a large effect. Extended tests were later performed on selected parameters. In general the experimental studies followed the fractional factorial design, although variations of the design process occurred. In addition, tests and measurements were usually repeated, depending on the experiment. Figure 1.1 shows the experimental methods used and the research scope.

After formulating the research questions, the impact of cutting conditions and strategies on surface integrity and tool wear was investigated. Emphasis was placed on the analysis of phenomena leading to the observed product quality and tool wear. It was found that the most efficient path for investigating the behavior of tool and workpiece materials in the machining process is through modeling and material characterization (microscopy and spectroscopy). Further information on the experimental studies is presented in section 3.1.

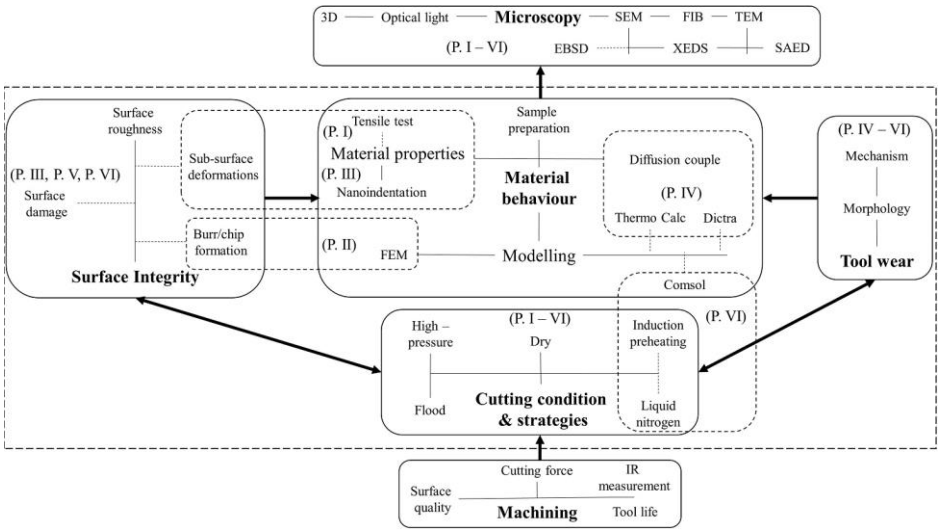

Figure 1.1. Schematic of experimental methods used, highlighted research scope, and publications presenting the related research. Notation: P.III, P.I, and others = Paper III, Paper I, and other papers.

Complementary tests for selected materials were also performed at companies to transfer technology from a laboratory to a production environment. This was accompanied by external validation of the results obtained.

1.6 Outline of the Dissertation

This dissertation has the following structure:

Chapter 1: Introduction

Introduces the research topic, hypothesis, research questions, and the limitations of the study.

Chapter 2: Mechanics of Metal Cutting

Brief introduction to different aspects of metal cutting and process and machinability parameters. It also discusses the materials studied.

Chapter 3: Machinability Study

This chapter is focused on the research area and presents and discusses the results of the author's research.

Chapter 4: Summary and Conclusions

Summarizes and presents the final conclusions of this research.

2 Mechanics of Metal Cutting

A wide range of material combinations and process parameters influence machinability. And the machinability term itself is characterized by a family of parameters including surface integrity, tool deterioration, chip control, burr formation and others. So many combinations of parameters and cases are possible when investigating the machinability of a material that machinability can be difficult to quantify. However, machinability studies do create better understanding of the difficulties in machining a particular material, which becomes useful information for manufacturing a product in a long run. The following section will introduce fundamental information about machining processes and factors influencing the machinability of a workpiece material.

2.1 Machining Process

The development of modern machines and machine tools began early in the twentieth century when machines were fitted with individual electrical engines. Taylor and White introduced a high-speed steel (HSS) cutting tool that was superior to any other cutting tools available at the time. In 1926 the introduction of cemented carbide cutting tools by the Krupps Company in Germany enabled a further increase in cutting speeds compared to HSS. The 1950s saw the introduction of numerically controlled machines that were operated by computer programs. A computer-controlled machined allowed the parts produced to have more complex shapes [10]. In the 1970s, the introduction of computer aided manufacturing (CAM) allowed the product development phase to be integrated with the product manufacturing process [11].

In a machining process, a cutting tool plastically deforms the being cut material so that a certain amount of material is removed from the workpiece in the form of a chip. There are various methods of machining including turning, milling, drilling, boring, shaping, broaching, reaming and others. In these processes, one or more cutting edges are involved and the machining can be continuous or intermittent, depending on the method [11]. This dissertation focuses on a continuous longitudinal turning process as it is a simplified yet most common process, using a single cutting tool that is clamped in a fixed toolholder.

2.2 Cutting Data

The basic operation of a turning process includes several different cutting data parameters. The cutting speed v_c, Figure 2.1, is defined as the rate at which the uncut surface of the workpiece passes the cutting tool, usually specified in m/min. In longitudinal turning, feed f (Figure 2.1) is defined as the axial movement of the tool in one revolution of the workpiece, usually specified in mm/rev. The cutting depth a_p, Figure 2.1, in longitudinal turning is the radial feed of the tool in relation to the surface prior to machining. The thickness of the metal removed is measured in mm. The combination of these three cutting parameters gives the rate of metal removal (MRR) from the workpiece [7].

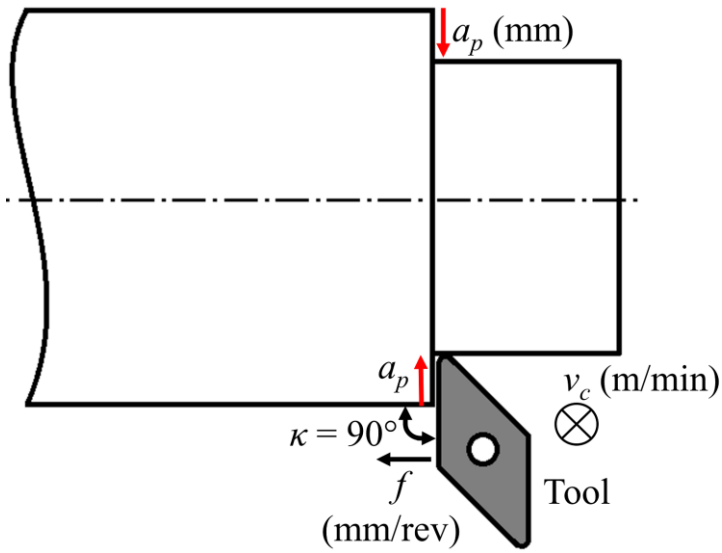

Figure 2.1. Illustration of cutting parameters a_p, v_c and κ in a turning process.

2.3 Tool Geometry

Tool geometry refers to the different macro and microgeometries that define the form and dimensions of the tools and the different angles related to the tool and setup. Macrogeometry involves the major geometric characteristics, while microgeometry concerns the form of the cutting edge or edge line. The edge radius r_β, is the radius of the cutting edge of the tool, which may vary along different sections. In a cutting process several different angles are involved (Figure 2.2), depending on the tool, toolholder, and setup conditions. The nose radius r is the

rounding of the tool tip, and together with the feed it determines the theoretical surface roughness. The angle between a plane perpendicular to the new surface and the rake face of the tool is called the rake angle γ. The rake angle influences the chip radius, among other phenomena, during the machining process. The size of the rake angle and clearance angle α vary depending on the tool attachment in the toolholder or its position. The clearance angle α is the angle between a plane parallel to the new machined surface and the clearance (flank) face of the tool. The major cutting edge angle κ and minor cutting edge angle κ_b depend on the geometry of the cutting edge and its position in the toolholder [11].

Together with conventional tool insert shapes, the geometry can be modified to enhance the performance of the tool. By introducing a chamfered edge, as a microgeometry parameter, the strength of the cutting edge can be improved. A cutting edge with wiper geometry increases the axial engagement of the tool with the machined surface, which can improve the surface roughness at increased feeds.

The cutting geometry can change during the cutting process as workpiece material adheres to the tool insert by forming built-up layers (BUL) and built-up edges (BUE). BUE can increase the rake angle and the inclination angle during the cutting process. BUL can enhance the tool life as a tool protective layer, but it can also increase the cutting edge radius [11]. However, the adhered material can also increase the tool wear rate, as discussed in 2.3.1.

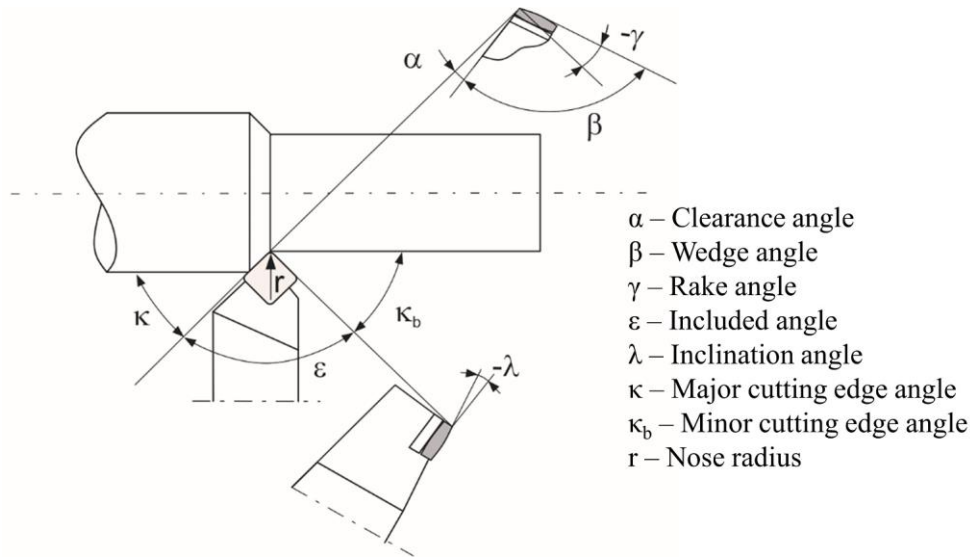

Figure 2.2. Illustration of different cutting angles describing the tool geometry in relation to the workpiece during conventional turning process, adapted from Vieregge [12] and later published by Ståhl [11].

2.4 Machinability

"Machinability" is a common term used to describe the ease of producibility of a certain workpiece material in a machining process. However, there is no universal definition of this term, and it may be used differently in different contexts. Measures of machinability are often discussed in terms of numbers such as the cost per machined component, quality of the finished product, or MRR. The problem is that these measures also differ depending on the type of operation and the parameters involved; for example turning compared to milling, the tool material used, cutting data, or the tool geometry. A workpiece material might be easy to produce in milling operations but difficult in turning operations. The machinability of a material depends on several factors such as its composition, microstructure, heat treatment, and properties [7]. Shaw [13] defined machinability using three main aspects: 1) tool life, 2) surface finish, and 3) power consumed in a process. Workpiece materials could also be classified in three categories depending on their machinability: 1) easy-to-machine materials, 2) ordinary wrought steels and cast irons, and 3) difficult-to-machine materials. The definition of machinability according to Trent and Wright [7] is slightly different: 1) tool life, 2) limiting rate of metal removal, 3) cutting forces, 4) surface finish, and 5) chip shape. Ståhl [11] later added environmental factors to the definition of machinability. These factors are connected to the material recycling process and the working environment while processing the material. Several attempts have been made to compare the machinability of different materials by quantifying different values for comparison [14-17]. However, there is still no method that is generally accepted. Historically, extensive research has been done to evaluate the machinability of different materials under different conditions [18-21], which also includes sustainability [22].

2.4.1 Tool deterioration

Tool deterioration or wear is a result of process loads acting on the tool that geometrically change the cutting edge. This tool wear can affect the MRR as well as the dimensional accuracy and the surface finish of the product [7]. In industrial machining operations it is thus important to predict or control the time when worn-out tools should be replaced. Prediction is possible because tool wear is often a stable process; however, there are cases when it results in unpredicted failure of a tool. Process temperature has a major influence on the rate of tool wear. An increase in process temperature may make the difference between controlled stable tool wear rate and spontaneous tool breakage.

The progression of tool wear depends on various parameters or mechanisms that change the load distribution on the cutting edges [11]. Understanding these and being able to predict tool life during machining is beneficial to understanding the

cutting conditions and developing a tool change strategy to maximize MRR or minimize part cost. Taylor's equation is well-known for describing the theoretical tool life during machining [23]. This equation was later extended by Kronenberg [24] and Colding [25, 26] to include more cutting data parameters. Archard formulated wear process in a physics-based wear model that describes the sliding wear between two bodies in contact [27].

Tool wear depends on several different factors such as cutting conditions, workpiece and tool material, tool geometry, and others. When combinations of several types of tool wear occur, modeling tool wear becomes difficult.

Tool deterioration depends on different mechanisms, which are classified into different categories:

1. Abrasive wear

   Abrasive wear is a process in which hard particles come in contact with a surface, abrading it and changing the dimensions of the tool and subsequently the machined part [28]. The hard particles may be contained in the chip or may be the result of a chemical reaction between the chips and the cutting fluid. Abrasive wear is in general the cause of flank and notch wear, but may also cause crater wear [10].

2. Adhesive wear

   Adhesive wear occurs when two asperities are in contact. Regardless of the smoothness of two surfaces, they will only be in contact at certain points. The local pressure at these points is generally very high and exceeds the yield point of the softer of the two materials. With increased process temperature, minute welds are formed at these points. In the course of sliding motion, these welds are sheared and fractions of the softer material stick to the welds, resulting in pluck-out of particles [29].

3. Oxidative wear

   Oxide layers are formed on surfaces at elevated temperature. These oxide layers thicken over time and then break up and are removed as wear particles. This wear process contributes to formation of notch wear and crater wear [30].

4. Diffusional wear

   Diffusional wear is also driven by high process temperatures, the rapid flow rate of workpiece material, and the solubility of different phases of the tool material in the flowing metal close to the tool. The diffusion wear process occurs when atoms from the tool diffuse into the flow of material or when workpiece material atoms diffuse into the tool material surface layers,

reacting with and weakening the surface. The wear process is accelerated at higher cutting speeds due to the higher process temperatures [7].

5. Fatigue wear

   Fatigue wear occurs when two surfaces in contact slide under high pressure and interlock. The repeated loading and unloading of these surfaces cause cyclic stress. In combination with high process temperatures, the surfaces are subjected to fatigue wear. The result is surface cracks that enhance wear out the surface or even breakage [13].

Different categories of tool deterioration exist and occur at different locations on the tool, as shown in Figure 2.3.

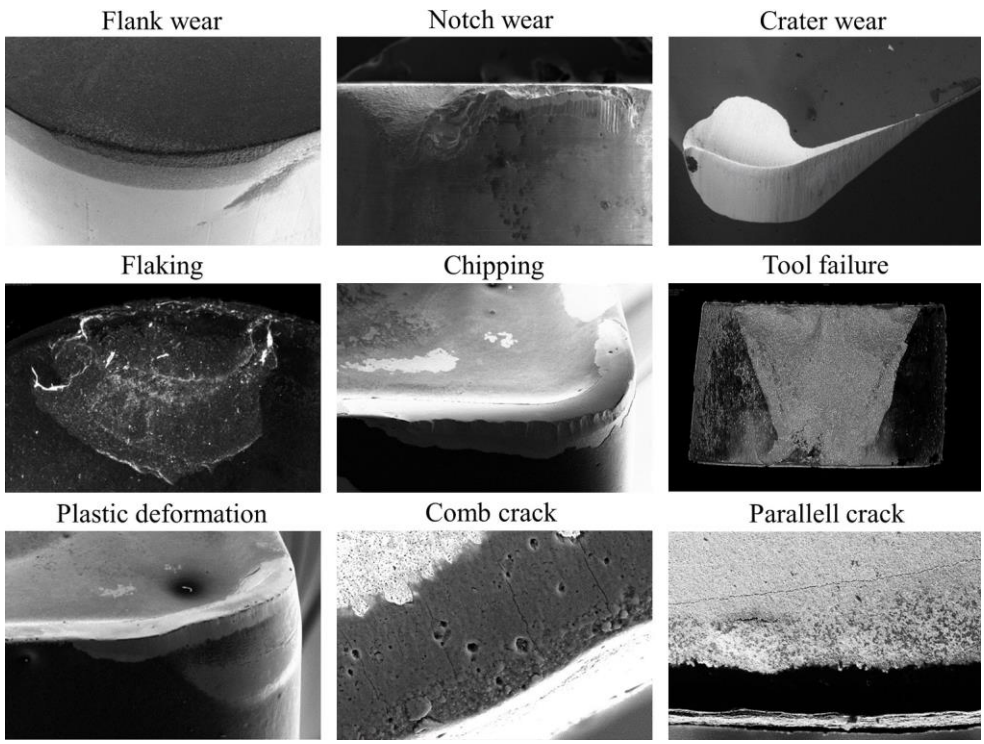

Figure 2.3. Examples of different types of tool deterioration, after Schultheiss [31].

2.4.2 Surface integrity

The quality of a machined surface has a significant impact on product performance, reliability, and longevity. Surface changes such as mechanical, metallurgical, and

chemical alterations affect the surface quality in a very small surface layer [32]. The term surface integrity (SI), introduced by Field and Kahles [33, 34], is used to indicate the quality of a machined surface or subsurface. According to Field and Kahles, SI is defined as: "The inherent or enhanced condition of a surface produced in a machining or other surface operation."

Parameters included in the term relate to essential information such as the topography and microhardness of the surface and variations in its macro- and microstructure. Field and Kahles developed an experimental procedure using three different data sets to collect data about and evaluate a machined surface (Table 2.1). Modern production of components using advanced material and alloys imposes high demands for the machined surface and dimensional accuracy, making it important to achieve SI requirements. Controlling the SI requirements usually adds cost, which makes it important to identify the problem and what manufacturing process needs to be considered, depending on the product. To achieve the necessary SI requirements in a machining process, two different aspects must be controlled. The first is surface texture, which includes the topography of the surface, or more specifically, the surface roughness. The second aspect involves surface metallurgy and includes the aspects of surface layer produced during machining.

Surface roughness is one of the most common SI parameters used in industry to evaluate the quality of a machined product. Various standards are used to measure surface roughness. The most commonly used parameter is the arithmetic mean surface roughness R_a along the workpiece length L_m, see Equation 2.1 [11].

$$R_a = \frac{1}{L_m} \cdot \int_0^{L_m} |y| \cdot d_x \tag{2.1}$$

The mean peak-to-valley within a sampling length R_z and maximum peak-to-valley R_{max} (R_t) are also used [10, 35]. Several different parameters related to the material, cutting tool, machining operation, and process characteristics influence the surface roughness of a product [10]. Process temperature is an important parameter that influences some of the SI parameters such as BUE, resulting from adhered and deposited workpiece layers. BUE is formed when workpiece material is successively accumulated near the edge line of a tool, which usually occurs in a narrow process window depending on the composite temperature. When the BUE reaches a critical size, the accumulated material separates from the tool and is transported away from the cutting zone by the chip material or is deposited on the machined surface. If the BUE is deposited on the newly machined surface, this will negatively affect the surface roughness. The generation of BUE can be minimized by controlling the process temperature, which can be achieved by changing parameters such as cutting speed, theoretical chip thickness, or cutting tool geometry [11].

Table 2.1. Experimental procedure to approach SI problems [34].

Minimum SI data set	Standard SI data set	Extended SI data set
1. Surface finish 2. Macrostructures (10x or less) a. Macrocracks b. Macroetch indications 3. Microstructure a. Microcracks b. Plastic deformation c. Phase transformations d. Intergranular attack e. Pits, tears, laps, and protrusions f. Built-up edge g. Melted and redeposited layers h. Selective etching 4. Microhardness	1. Minimum surface integrity data set 2. Fatigue tests (screening) 3. Stress corrosion tests 4. Residual stress and distortion	1. Standard SI data set 2. Fatigue tests (extended to obtain design data) 3. Additional mechanics tests a. Tensile b. Stress rupture c. Creep d. Other specific tests (e.g. bearing performance, sliding friction evaluation, sealing properties of surfaces)

2.4.3 Cutting forces

Forces are generated when a chip is formed and the material is cut off in a cutting process. These forces influence the process in different ways and determine the machine power required as well as the loads on the bearings, tool, and machine structure. The forces are the source of vibrations and increases in cutting temperature. Measured cutting forces can be used to compare the machinability of materials and in real-time monitoring of tool wear and failure [10]. Cutting forces are primarily dependent on the theoretical chip thickness h_1 and chip width b_1 (collectively representing chip area). Other parameters such as cutting speed and tool geometry also influence the cutting forces. The resultant force in longitudinal turning can be divided into three orthogonal cutting forces or force components, as shown in Figure 2.4. The force component acting on the rake face of the tool or in tangential direction is called the main cutting force F_c. The component acting in the axial direction is called the feed force F_f. The third component is called the passive force F_p and pushes the tool in the radial direction away from the workpiece [11]. In a milling operation, the forces acting on the tool are defined as T-direction force (tangential), equivalent to the main cutting force; A-direction force (axial), corresponding to the feed force; and R-direction force (radial), equivalent to the passive force.

Most forces can be modeled in terms of linear force dependence by extrapolating to the theoretical chip thickness h_1. This applies in particular for a cutting tool with constant rake angle γ and a contact length that exceeds the critical contact length l_{clc} (Equation 2.2).

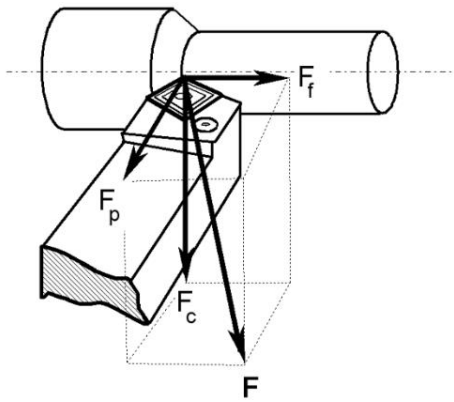

Figure 2.4. Cutting force components during a conventional turning operation and the resultant cutting force *F*, adapted from [36].

$$F_c = C_2 + C_1 h_1$$
$$F_f = D_2 + D_1 h_1 \quad (2.2)$$
$$F_p = E_2 + E_1 h_1$$

Power consumption in a cutting process can be described as the energy consumed to produce a certain volume of chips. The cutting resistance of a material is a way to describe the machinability of a material and is one of the different factors that influence power consumption in a cutting process. The cutting resistance of a material is the force required per total chip area to machine a specific workpiece material (Equation 2.3).

$$Cr = \frac{F_c}{h_1 b} \quad (2.3)$$

The cutting resistance is dependent on the cutting tool involved, specifically its geometry, and the influence of tool wear. The cutting resistance can be expressed using the parameters Cr_1 and Cr_2, which describe the load and energy consumption on the rake face (Cr_1) and on the clearance (Cr_2) (Equation 2.4). As the flank wear land develops on the clearance face, the contact between the tool and workpiece increases, which increases Cr_2. The cutting resistance can be seen as a process parameter and changes depending on the cutting process involved. Furthermore, Cr_1 can be seen as representing a material characteristic, while Cr_2 is linked to the process and microgeometry of the tool.

$$Cr = Cr_1 + \frac{Cr_2}{h_1} \quad (2.4)$$

The power consumption can be calculated if the magnitude of the cutting forces, cutting speeds, and feed speeds are known (Equation 2.5). Usually, the energy consumption is closely linked to v_c and can be simplified.

$$P_t = v_f F_f + v_p F_p + v_c F_c \approx P_c = v_c F_c \tag{2.5}$$

If the value of the cutting resistance is known, the power consumption can be calculated as Equation 2.6.

$$P_c = v_c F_c = v_c h_1 b_1 C r \tag{2.6}$$

When taking the efficiency of the motor η into account, the total power involved in the cutting process can be expressed as Equation 2.7 [11].

$$P_m \approx \frac{P_c}{\eta} \tag{2.7}$$

2.4.4 Chip control

In the late 1930s, chip formation was divided into three categories and described in terms of the following types [37]:

- Discontinuous or segmented chip
- Continuous steady state chip
- Continuous chip with built-up edge

The type of chips produced have a practical influence on the machining process as regards [13]:

- Personal safety
- Possible damage to equipment and product
- Handling and disposal of chips after machining
- Cutting forces, temperatures, and tool life

Chip control or chip breakability is important to manage chip formation in a cutting process. In general, short chips are desirable because it is easier to remove them from the cutting zone. Long, continuous chips have a tendency to be caught against and nest around the workpiece material, resulting in chip hammering and destruction of the machined surface. Table 2.2 shows how chips are classified. Chip breaking is achieved by inducing chip curl, which causes periodic fracture due to excessive strain in the chip. Chip breaking can be controlled by introducing a chip breaker on the cutting tool, increasing the feed, or enhancing the brittleness of the

workpiece [13]. Cutting fluid also affects chip breakability. Greater chip curl is achieved by introducing a cutting fluid that reduces the contact length between the chip and the tool interface [38]. Chip control has been emphasized lately due to the development of a higher degree of automated machining that improves product quality and material removal rates. Jawahir and van Lutterveld presented an extensive review of chip control in metal cutting and listed parameters influencing efficient chip breaking and chip disposal (Figure 2.5) [39]. Jawahir et al. discussed the effects of chip flow on tool wear. The effect of the chip breaker groove geometry on tool wear could be an important consideration compared to other wear factors [40].

Table 2.2. Classification of different chip types [41].

Curling		Favorable	Unfavorable	
Straight	1 Ribbon chips	1.2 Short 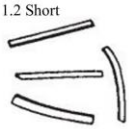		1.1 Long/1.3 Snarled 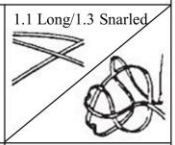
Mainly up-curling	2 Tubular chips	2.2 Short 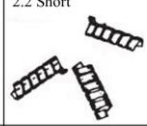	2.1 Long 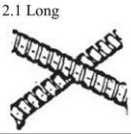	2.3 Snarled 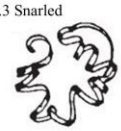
	3 Spiral chips		3.1 Flat/3.2 Conical 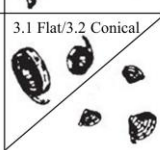	
Mainly side-curling	4 Washer type chips	4.2 Short 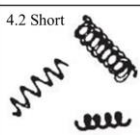	4.1 Long 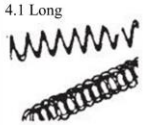	4.3 Snarled 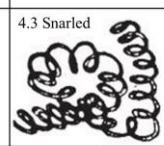
Up- and side-curling	5 Conical helical chips	5.2 Short 	5.1 Long 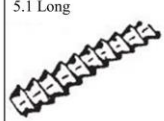	5.3 Snarled 
	6 Arc chips	6.2 Loose/6.1 Con. 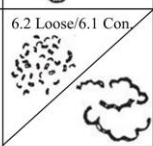		
	7-8 Natural broken chips	7 Elemental 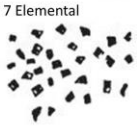		8 Needle 

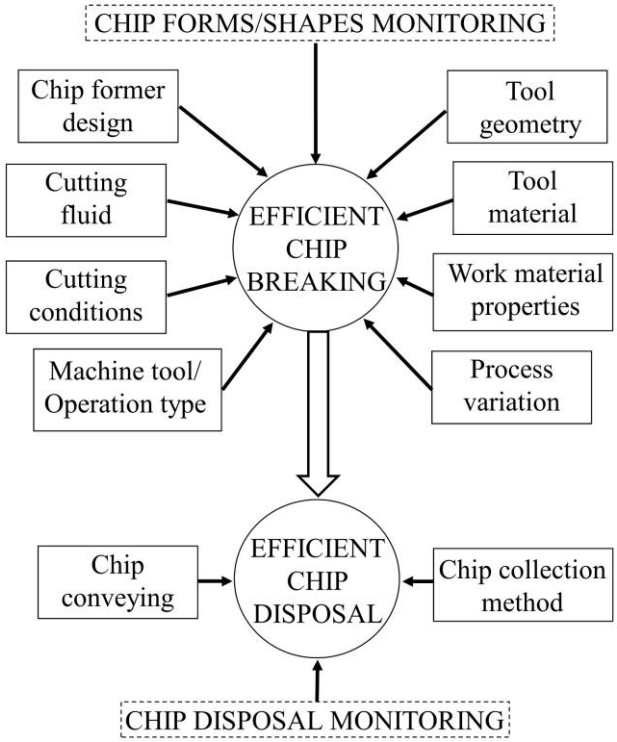

Figure 2.5. Parameters influencing efficient chip breaking and chip disposal [39].

2.4.5 Burr formation

Burrs are mainly formed at the end of a cut and are highly undesirable. A burr is a partially formed chip, created at the surface along the workpiece, which is too weak to support the forces involved in creating a complete chip. A burr extends over the intended surface and makes the handling process and assembly operations more difficult [42]. Pekelharing was the first to describe the connection between chip formation process and the mechanism of burr formation in metal cutting [43]. Gillespie and Blotter published the first fundamental work relating to burr formation [44, 45]. They introduced four categories of burr formation: Poisson burr, rollover burr, cutoff burr, and tear burr (Figure 2.6). Poisson burrs appear when the material tends to bulge to the sides during compression, until permanent plastic deformation occurs. Rollover burr is also known as exit burr because it is usually formed at the end of the cut when the chip is bent rather than sheared off. Tear burr appears when the material tends to tear off from the workpiece instead of shearing off. Cutoff burr appears when workpiece separation occurs from the raw material before the separation cut is finished [44].

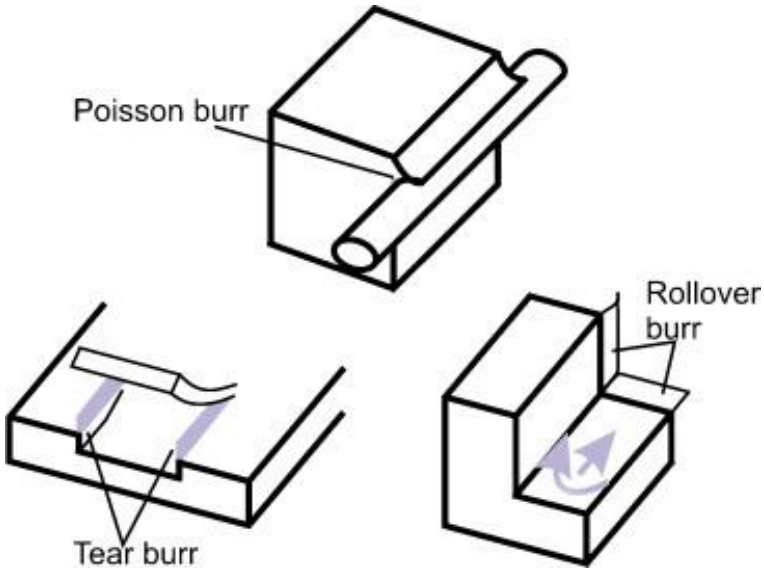

Figure 2.6. Different types of burr formations [44].

2.5 Deformation Zones

In a cutting process, the major part of the energy provided is converted to heat through plastic deformation and friction. The energy provided is directed into three zones where material deformation occurs. Each of the three deformation zones is exposed to a rise in temperature that is proportional to the volume of the geometric extension of the zone and the amount of converted energy. The primary deformation zone (1) extends from the tip or edge line of the cutting tool to the intersection between the surface of the undeformed workpiece and the deformed chip. In this region the material is sheared off and removed in the form of a chip. In the secondary deformation zone (2), the deformed chip is transported from the primary cutting zone along the rake face of the tool. In the tertiary deformation zone (3), the cutting tool moves over the newly machined surface and the workpiece surface slides in contact with the clearance face of the cutting tool. The position and width of the deformation zones ε_I in the shear plane, ε_{II} in the deformed chip and ε_{III} in the newly machined surface, are illustrated in Figure 2.7. In the cutting process, the deformation width ε_I has a direct effect on the deformation speed. The deformation widths of ε_{II} and ε_{III} have a strong effect on the lifetime of the cutting tool through tool wear process. Depending on the volume of these deformation zones, the cutting tool can suffer from rapid wear if these small zones rise in temperature due to heat concentration [11].

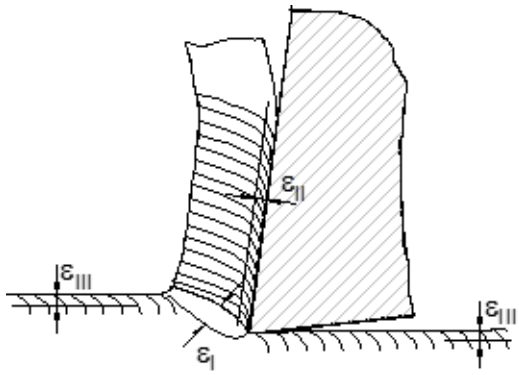

Figure 2.7. Illustration of deformation zones ε_I, ε_{II} and ε_{III} [11].

2.6 Single-phase and Refractory Metals

Throughout this dissertation, the phrase "single-phase metal" refers to the purity or the single-crystal structure of the metal. The workpiece materials used in the experiments have a purity of ≥ 99.7 %. The use of SPM is limited in normal production, and it is mainly used for specialized products such as components for particle accelerators. These components place high demands on tolerances and surface roughness because they have to function in a clean ultra-high vacuum environment at cryogenic temperatures of 2–4 K. The required surface roughness (R_a) values of these components are usually below 0.8 µm and even below 0.1 µm. These requirements increase the cost of components significantly, especially when producing components in materials that are difficult to machine. Although a wide selection of materials are used in these facilities, this thesis sets the primarily focus on copper, niobium, and tungsten. Copper and niobium are soft, ductile, strain-hardening materials that are challenging to machine due to continuous chips, chip welds, and damage to surfaces, resulting in poor surface quality. Tungsten, on the other hand, is brittle and a much harder metal. Brittle fracture occurs during machining and the resulting surface quality is also poor. These challenges can be difficult to overcome because surface quality is of the utmost importance. Niobium and tungsten belong to the group of refractory metals, which are characterized by a higher melting point than platinum (> 1772 °C). Niobium and tungsten also have a BCC crystal structure, and in a certain temperature range, these metals undergo a ductile to brittle transition (DBTT) resulting in increased ductility (reduction in area) and a decrease in yield and tensile strength, which may be favorable or unfavorable for the surface generation and tool wear. The following section will present a brief introduction to these three materials focusing on parameters that potentially influence their machinability.

2.6.1 Oxygen-free copper

Copper (Cu) is one of the first metals ever used by humans because it is one of the few metals that can naturally occur in a usable metallic form. Historically, it has mainly been used as an alloy in brass or bronze, for example, in decorative or building materials. Today, Cu is one of the most common metals used in commercial products, ranked third after steel and aluminum. It has excellent electrical and thermal conductivity and high resistance to corrosion. It is therefore used in electrical wires and circuits and in pipes, for example in heating systems, air conditioning, gas lines and drinking water [46]. It is also used in components for particle accelerators such as cavities (Figure 2.8a) or magnets.

Cu is a soft and ductile metal that is difficult to machine because the surface is prone to chip welds, burrs, and smearing of the machined surface. The chip formed is long and continuous, and chip breakers on the cutting tool have little effect. Sharp cutting tools are recommended. On the positive side, tool wear is comparatively low [46, 47]. Selected material properties are shown in Table 2.3 and the microstructure of Cu is shown in Figure 2.8b.

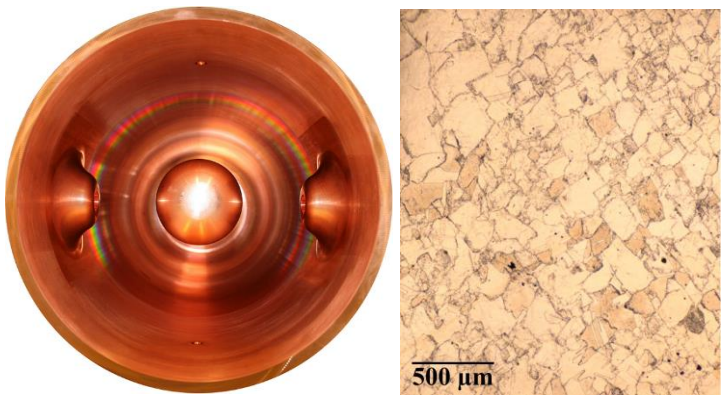

Figure 2.8. (a) Accelerator cavity in oxygen free copper (OFC); (b) microstructure of OFC.

Table 2.3 Selected material properties for annealed copper, typical values [48].

Designation	Hardness [HV]	Yield Strength [N/mm^2]	Ultimate Tensile Strength [N/mm^2]	Elongation at Break [%]	Thermal Conductivity [W/m-K]
Copper	50	33.3	210	60	398 @ 27 °C

2.6.2 Niobium

Niobium (Nb) or columbium (as it was called at its discovery) belongs to the group of refractory metals that have a higher melting point than platinum (> 1772 °C). The element was discovered by Charles Hatchett in 1801, but it would be more than a

century before any practical use was made of it. Consumption of Nb increased in the 1930s when it was used as an alloy addition to stainless steel and superalloys. The use of Nb in superalloys increased during the Cold War in the late 1950s and the early 1960s when space and missile defense programs were launched [49]. Nb is corrosion-resistant and exhibits superconductive properties and so is used to manufacture superconducting cavities (Figure 2.9) as well as magnets for particle accelerators. At present, the primary sectors consuming Nb are construction, automotive, and oil and gas. Adding 50–60 grams of Nb per ton is enough to produce high-grade steel with increased strength and durability and lower weight. The addition of US $9 worth of Nb to a car leads to a 100 kg weight reduction and ongoing fuel savings of one liter per 200 km [50].

In high-purity form, niobium is also used for manufacture of nozzle for missile and space lunch vehicles and other military applications. Therefore, there is very limited information about tools and cutting conditions for machining pure Nb in public domain. However, the machinability of Nb is comparable to that of soft and ductile copper [51], which leads to surface defects such as adhesion, built-up edges, side-flow, and burr formation. Table 2.4 shows selected material properties. The microstructure of Nb is shown in Figure 2.10.

Figure 2.9. Accelerator cavity in Nb.

Table 2.4 Selected material properties for annealed niobium, typical values [48].

Designation	Hardness [HV]	Yield Strength [N/mm²]	Ultimate Tensile Strength [N/mm²]	Elongation at Break [%]	Thermal Conductivity [W/m-K]
Niobium	80	207	300	30	52.3 @ 20 °C

2.6.3 Tungsten

Tungsten (W) belongs to the group of refractory metals and is distinguished by its high density (19.3 g/cm^3) and by having the highest melting temperature (3422 °C) of all metals. It has high strength at high temperatures, resistance to wear, and good electrical and heat conductivity. It was initially known as wolfram, but the origin of that name is unclear. It probably dates back to tin mining in Germany in the Middle

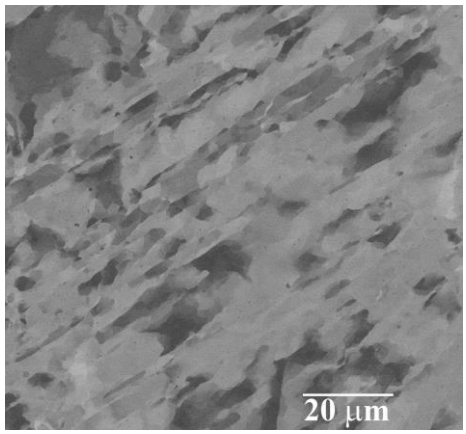

Figure 2.10. Microstructure of high-purity niobium.

Ages, for the tin ore included the mineral (Fe, Mn)WO_4. The word "tungsten" comes from the Swedish words *tung sten* (heavy rock). W was discovered as a part of a mineral by Cronstedt in 1755 and Scheele in 1781. However, it was two Spanish scientists who first described the isolation of the element. After its discovery, W was little used until the late nineteenth and early twentieth century when it came into use as an alloy for high strength steels. With the discovery of ductile W that could be used as a filament in light bulbs, the use of W increased rapidly. W also came to be used in special tool steels and tungsten carbides for use in cutting tools. With the introduction of space programs, the use of W also extended to nozzles of rocket motors and protective shields for space vehicles for high temperature use [52]. Figure 2.11a shows a prototype of a component used in a research facility and manufactured in single-phase W.

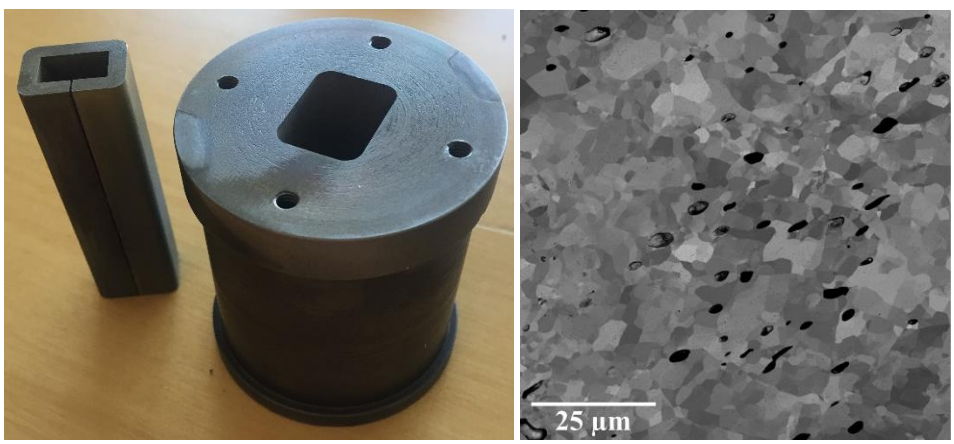

Figure 2.11. (a) Prototype of component in a research facility manufactured in W; (b) microstructure of high-purity W.

As with Nb, machinability information about pure W is limited, yet it is generally accepted that W is a difficult-to-machine material. Unlike Nb and Cu, the metal is brittle and hard, which results in chipping of machined parts at unsupported surfaces and rapid tool wear during machining [53]. Selected material properties are shown in Table 2.5. The microstructure of W is shown in Figure 2.11b.

Table 2.5 Selected material properties for tungsten, typical values [48].

Designation	Hardness [HV]	Yield Strength [N/mm^2]	Ultimate Tensile Strength [N/mm^2]	Elongation at Break [%]	Thermal Conductivity [W/m-K]
Tungsten	310	750	980	0.2	163.3

3 Machinability Study

The following sections present a machinability study of selected single-phase metals. The focus area of the research is presented and the results are described and analyzed.

3.1 Experimental Study

The experimental studies were limited to longitudinal machining in a lathe. ISO CNMG-, CNGA-, CCMW- or CCGA120408 tool geometries were used in Papers I and III–VI. The tool was clamped in a DCLNL or PCLNL-Jet toolholder, providing -6° back and -6° side rake angles and a 95° major cutting edge angle. The cutting fluid used was Cimstar 501-02. In Paper II a triangular TPUN160308 tool was clamped in a R175.2-3225-16 toolholder with 0° back and -6° side rake angle. Cutting forces were recorded with a piezoelectric Kistler 9129-AA dynamometer, and surface roughness was measured with a Mahrsurf PS1 profilometer. Samples of the machined surface were cut out with a wire-EDM, mounted in epoxy for further preparation, and polished with a diamond (3μm and 1 μm) and SiO_2 suspension. Nanoindentation was performed on a NanoTest Vantage system with the load range 1 to 200 mN using a Berkovich diamond indenter with a 120 nm tip radius.

Different types of microscopy techniques were used depending on the results required. An Alicona 3D light microscope was used for general imaging and 3D topography measurement of the machined surface and tool wear. Tool wear was also measured in an Olympus SZX7 optical microscope. Scanning electron microscopy (SEM) images were acquired using a Tescan Mira3 equipped with a field emission gun and an Oxford XEDS detector. A focus ion beam (FIB) lift-out technique was performed in a FEI Nova NanoLab 600 dual beam FIB/SEM. Transmission electron microscopy (TEM) was performed in a JEOL 3000F equipped with a field emission gun and Oxford XEDS detector.

Finite element (FE) simulations of burr formation were performed for different cutting parameters of the case of machining of OFC. Abaqus v6.12-3 was used for the simulations. The FE formulation used was Euler-Lagrangian (CEL) [54]. A constitutive model was used to describe the plastic behavior of the workpiece using

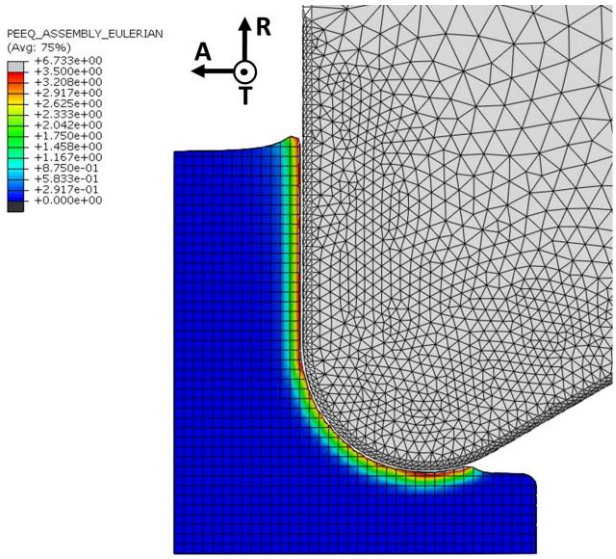

Figure 3.1. FE modeling of burr formation during machining of OFC.

Johnson-Cook plasticity [55]. Due to limited computational power, simulations were limited to one revolution of the workpiece. Figure 3.1 shows an example of the results from FE simulation. Further details of the FE modeling process can be found in Paper II [56].

The diffusion couple method was used to study the interaction between Nb and cemented carbide (CC) under static conditions of high pressure and temperature (HP-HT) similar to those of the machining process. A round polycrystalline diamond (PCD) tool insert (PCD top layer and CC bottom layer) of 6.35 mm in diameter was placed in a cylindrical Nb capsule surrounded by a special high-pressure assembly to ensure uniform pressure and heating of the Nb capsule. The assembly was placed in a toroidal high-pressure apparatus HPAT-30 (Figure 3.2), and was heated to 1000 °C under 2 GPa pressure for 10 min. The temperature field within the HP-HT assembly was calculated using an electrical-thermal coupling implemented in FE software according to [57]. Further information on the diffusion couple setup can be found in Paper IV [58].

The cryogenic distribution system consists of a Cryostor 60 dewar supplied by Statebourne cryogenics with a 2.8 bar working pressure, 60 liter storage capacity, and an integrated pressure system (Figure 3.3a). The dewar was connected to a subcooler, a copper coil submerged in liquid nitrogen (LN_2), to reduce the fraction of gas in the LN_2 stream during transportation to the outlet nozzle. The cryogenic machining setup is shown in Figure 3.3b.

Figure 3.2. Toroidal high-pressure cell used for HP-HT treatment of the diffusion couple sample.

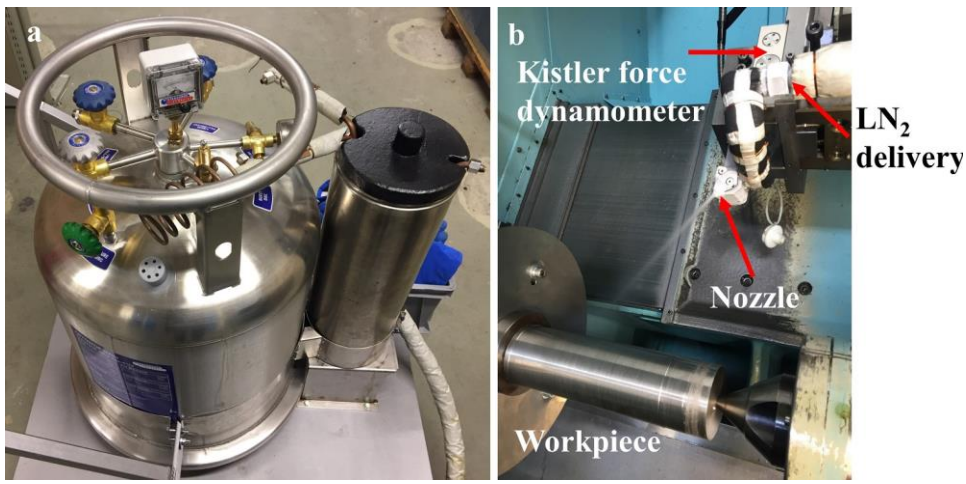

Figure 3.3. (a) Cryogenic distribution system; (b) Cryogenic machining setup.

An induction heating system was used to preheat the workpiece before machining. The system consists of a water-cooled copper coil with ten windings that is configured for continuous operation of about 140 A_{rms} coil current at 20 kHz, corresponding to 1.2 kW of active power heat. The copper coil was mounted on a stand for easier installation in the lathe. Figure 3.4 shows the machining setup. The temperature was measured using a FLIR ThermaCAM T360 IR camera and thermocouples.

Heating a W workpiece clamped in a lathe was simulated in Comsol Multiphysics to understand the heat transfer prior to experimental studies of induction-assisted machining (IAM). The simulations were divided into two parts: the induction heating of the W workpiece and the subsequent cool down. The results of the simulations of the heat distribution within the W workpiece at different time intervals are presented in Figure 3.5, where 0 mm indicates the center of the copper coil in the axial direction, reflecting the highest temperature during heating of the workpiece (Figure 3.5a). Figure 3.5b shows that the highest temperature is at the free end of the workpiece and the coolest section is at the clamped end during cool down. Further information about the induction heating process, simulations, and identification of the process temperature is available in [59].

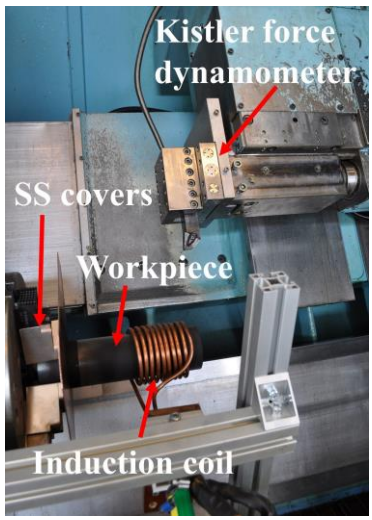

Figure 3.4. Induction preheating setup for hybrid thermally assisted machining of W.

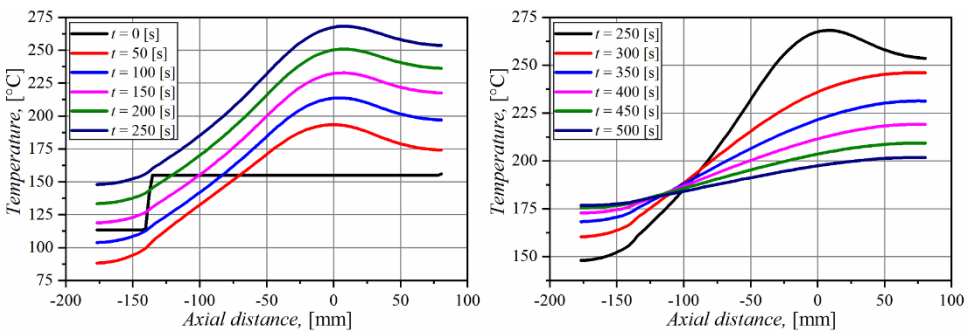

Figure 3.5. (a) Simulation of heat distribution during induction heating at different time intervals; (b) simulation of the cooling process of the W workpiece.

3.2 Product Quality and Surface Topography

Components produced for accelerators in research facilities usually have high demands for quality related to product functionality. These special requirements limit the choice of materials and therefore the use of uncommon material is more frequent in such facilities. The use of SPM leads to various challenges during machining and to quality-related problems, which will be discussed in the following section.

The surface topography and quality of a product are strongly connected to surface integrity (SI) parameters. These parameters depend on material properties of the workpiece and the selection of tools and cutting parameters during machining. The quality of the machined surface is mainly associated with surface roughness, as it is easier or more effective to measure than other parameters. Methods of surface roughness measurements are usually nondestructive compared to other SI parameters related to the subsurface information. Surface roughness is the most frequently used parameter in industry to evaluate the quality of a product.

3.2.1 Influence of burr and chip formation on product quality

The influence of burr and chip formation on quality of the machined workpiece is dependent on material properties related to ductility or brittleness. Ductile materials such as OFC and Nb form continuous chips, which can tangle around the workpiece and damage the machined surface (see Figure 3.6). Ductile materials also tend to push uncut material ahead of the tool (Figure 3.7a) or bulge on the sides, forming unwanted burrs. This is bad for dimensional accuracy and handling, and requires extra attention to the product to remove these burrs. Brittle material, on the other hand, usually creates short chips, which is desirable in the machining process. However, the high brittleness when machining W can result in burrs at unsupported edges (chipping) (see Figure 3.7b). Hashimura et al. [60] analyzed burr formation with FE simulations and identified eight stages of the burr formation process when comparing ductile and brittle materials. Toropov et al. performed FE simulations and studied the degree of burr formation in relation to tool geometry and cutting parameters [61-64].

Production costs can be reduced by minimizing burr formation or problems with chips during machining. Problems with chip re-weld or material redeposition are clearly shown in the top part of Figure 3.6. An attempt was made to reduce the degree of chip re-weld by submerging the OFC rod in LN_2 before machining with similar cutting parameters and tool. The result can be seen in the bottom half of the picture where the material redeposition have been reduced to a minimum. Similar results have been seen in studies comparing different coolant methods and LN_2

coolant [65, 66]. A different example of excessive pile-up of material in front of the tool, known as radial/Poisson burr (Figure 3.7a) is strongly related to cutting parameters and selection of tool/geometry. Machado et al. studied the influence of cutting parameters on the formation of exit burrs when machining carbon steel AISI1045. The thickness and height of the burr is affected by the cutting speed, feed rate, entering angle, and depth of cut [61].

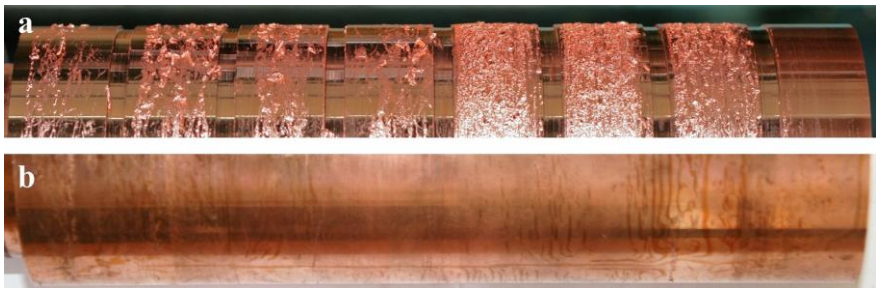

Figure 3.6. Surface of OFC workpiece exposed to chip re-weld and material redeposition (top view) and OFC workpiece submerged in LN_2 before machining (bottom view).

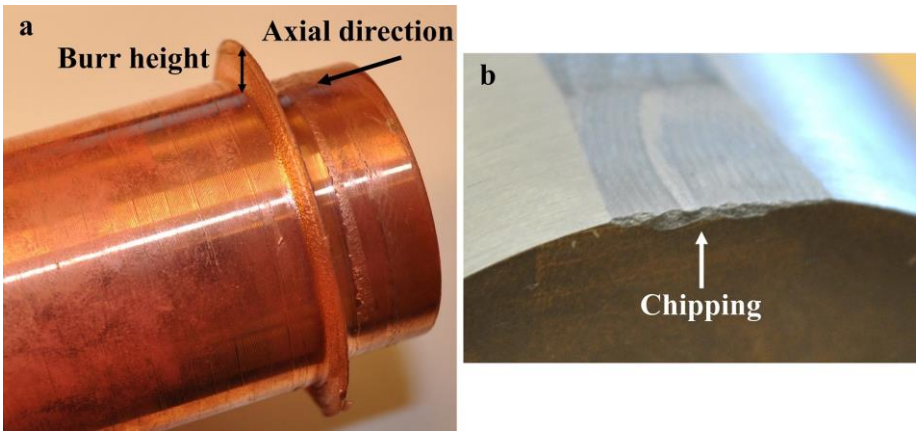

Figure 3.7. (a) Excessive radial burr formation during machining; (b) chipping of unsupported edge.

Burr formation in the cutting process of OFC was studied in Paper II [56] by using high-speed footage at 9300 fps. From an experimental test at v_c = 150 m/min and f = 0.2 mm/rev, burr formation can be divided into different stages. Burr initiation is shown in Figure 3.8.1. The burr continues to grow until a maximum is reached in Figure 3.8.3. In the next step (Figure 3.8.4), the burr and chip become entangled with each other, and the chip removes the burr from the surface and transports it away from the cutting zone, at which stage the process starts over again. The high-speed footage shows that the burr formation depends on the chip curl closest to the

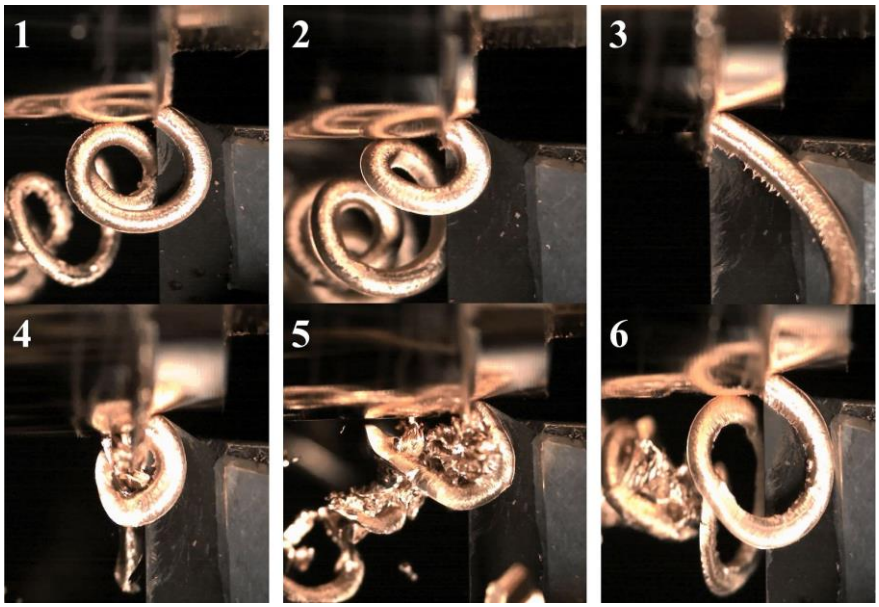

Figure 3.8. Different stages of burr formation when machining OFC.

cutting zone. At feed $f = 0.2$ mm/rev, the chip curl is further away from the cutting zone and the burr is not removed as frequently as at $f = 0.35$ mm/rev. However, the burr formation is more intense at $f = 0.35$ mm/rev. This was also seen in the individual cutting case in the experimental studies where the burr was partially removed at the time when the cutting process was halted after the tool was removed, resulting in a need for repeated tests to ensure that the burr had not been removed from the workpiece.

FE simulation of the influence of cutting parameters on burr formation during machining OFC material was performed. The cutting parameters used in the FE simulations and experimental verifications are shown in Table 3.1.

Table 3.1. FE simulation cutting parameters.

Parameter	Value
f (mm/rev)	0.06, 0.2, 0.35
a_p (mm)	0.5, 1, 2
κ (°)	90, 80, 70

The burr height and width could be determined by counting the number of pixels of the affected elements in the FE simulations, as seen in the bumps in Figure 3.9. FE simulations show that burr height may double, depending on the selection of major cutting edge angle and cutting depth (Figure 3.10a and b). The feed rate has only a minor impact on burr height.

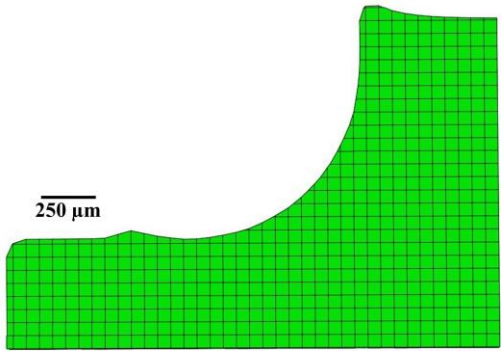

Figure 3.9. FE simulation of burr height for OFC at a_p = 1 mm, f = 0.35 mm/rev, and κ = 90°.

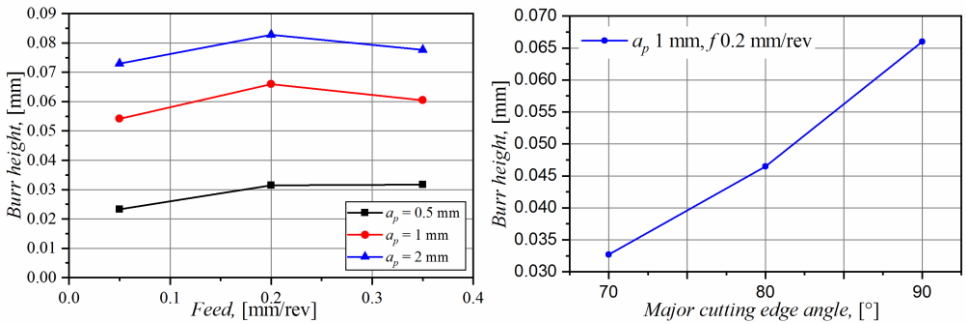

Figure 3.10. (a) FE simulations of radial burr height at different feeds; (b) radial burr height at different major cutting edge angles.

The experimental tests show that all the tested parameters influence the degree of burr formation (see Figure 3.11a and b). Figure 3.11a shows there is a significant increase in the burr height between a_p = 0.5 mm to 1 and 2 mm depending on the cutting depth. At cutting depths of 1 and 2 mm, there is a local minimum at f = 0.2 mm/rev. When comparing the FE simulations and experimental results, the influence of cutting depth is similar, although the burr height from the FE simulations is exceptionally small. Small burr heights and deviation of the feed results can be related to the different conditions as the FE simulations only consider one revolution. In the simulations, only the initiation of the burr is considered compared to the fully developed burr in the machining tests.

Burr formation in the radial direction is closely connected to the generated burr thickness. Cross sections of samples machined at f = 0.2 mm/rev and a_p = 0.5 mm and 2 mm show differences in burr thickness (Figure 3.12). At cutting depth 0.5 mm (Figure 3.12a), the burr thickness and height are not as visible as at a_p = 2 mm, where the burr thickness is 0.55 mm (Figure 3.12b). The burr thickness is larger

than the feed f = 0.2 mm/rev, which means that the burr formed at the current revolution will not be removed by the next revolution. Measurements of burr thickness on the other samples also show higher values compared to the corresponding feed. When the burr thickness from the previous revolution is less than the corresponding feed, the burr formation can be cut off in the next revolution [62].

The results from different major cutting edges angle reveal a significant increase in burr height between κ = 70° and 80° (Figure 3.13). Examining the cross sections of the different machined samples, only a small burr height of 0.066 mm exists at κ = 70°, and no burr thickness is visible. At κ = 70° the direction of the burr is directed toward the uncut surface and the resultant force (A-R direction) compresses the material instead of pushing it aside. FE simulations support the trend of increasing burr height with increasing major cutting edge angle, although the experimental result at κ = 80° is higher.

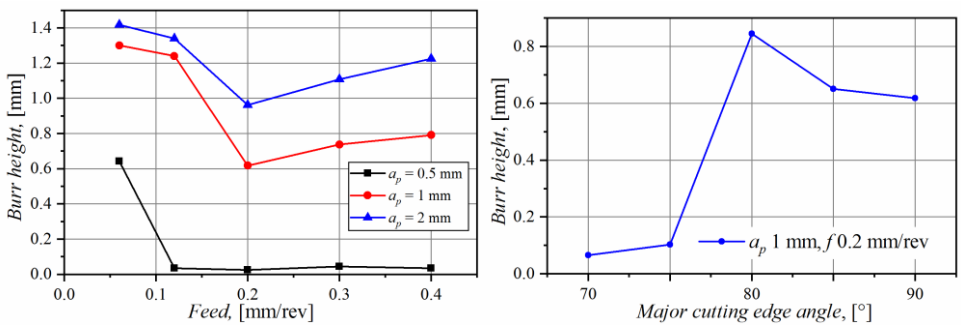

Figure 3.11. (a) Experimental results of radial burr formation at different feeds; (b) radial burr formation depending on the major cutting edge angle.

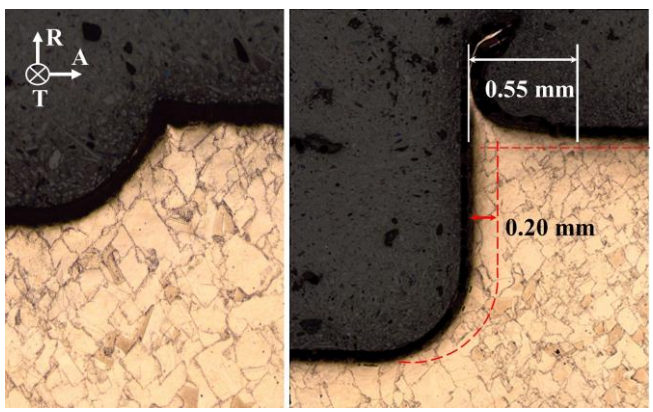

Figure 3.12. Burr formation at feed f = 0.2 mm/rev, (a) a_p = 0.5 mm and (b) a_p = 2 mm.

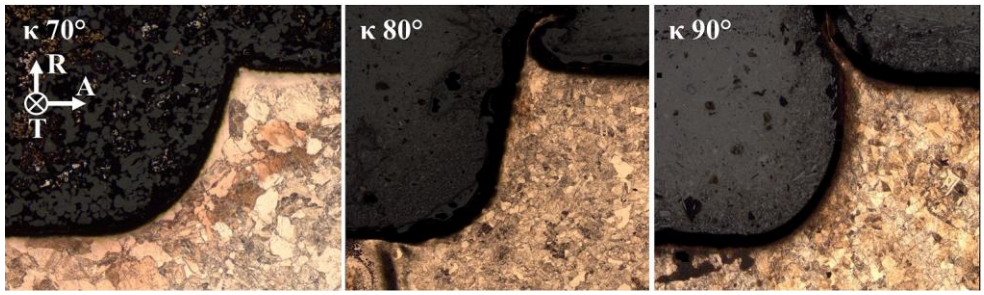

Figure 3.13. Cross sections of samples machined at different major cutting edge angles κ = 70°, 80° and 90°, with a_p = 1 mm and f = 0.2 mm/rev.

3.2.2 Generated surface topography

In the design process, values of surface roughness R_a are often specified on the drawings as a quantitative value to measure product quality. R_a values are specified depending on different aspects and conditions related to material properties, the functionality of the product, size, or aesthetic appearance. Machining SPM comes with various challenges and achieving the specified surface roughness can be difficult.

Equations for calculating surface roughness R_a during machining have been published by several authors [67-71]. The equations are in general based on experimental data with numerical adaption. Puhasmägi [72] proposed a model divided into three different machining cases depending on a combination of feed and tool nose radius. The model is limited to surfaces generated by the nose radius of the cutting tool. One of the machining model cases was further used to express an approximate analytical equation for R_a (Equation 3.1) where r is the tool nose radius [73].

$$R_a = 0.77 \cdot \left(1 - \frac{\frac{f}{2r}}{\arcsin\left(\frac{f}{2r}\right)}\right) \cdot r \qquad 3.1$$

Published equations can be used as a general expectation of the surface roughness. However, experimental results and calculated values deviate due to defects such as BUE and side-flow, damage to the tool, and vibrations.

In particle accelerators, components made for the accelerator have the highest requirements on the machined surface. OFC and Nb are frequently used in these structures, and the requirements of the surface roughness for the most critical components range from R_a = 0.05–0.8 µm.

3.2.2.1 Copper

Papers I and II present the influence of cutting parameters on material properties [74] and burr formation [56] during machining of OFC. However, surface topography and especially surface roughness were not discussed in detail. Machining tests focusing on surface roughness were performed but in a different context, with the focus on the production of prototype OFC components in collaboration with local manufacturing industries. Machining tests showed that the targeted value of R_a = 0.4 µm surface roughness was consistently met. These successful tests were performed with uncoated tools with a nose radius r = 0.2 mm with VCGT and DCGT geometry at cutting speeds v_c = 75–400 m/min, feed f = 0.01–0.05 mm/rev, and cutting depth a_p = 0.05–0.1 mm. The results show that cutting speed has less influence on the resulting surface roughness than the feed and cutting depth have. Two of the major problems in machining OFC are controlling the continuous chip and having a tool sharp (small edge radius r_β) enough to cut off the material and so avoid problems with burr formation and re-welding on the cut surface. An uncoated tool with a small nose radius performs very well at very low feeds and cutting depths when cutting OFC. At these cutting conditions, the maximal theoretical chip thickness is low, and due to the low cutting depth and feed, the chip is not directed toward the newly cut surface and is less prone to tangle around the workpiece. Moreover, the temperature of the chip is lower due to the small thickness of the chip, which minimizes re-welding of debris and results in a better surface quality.

It is worth mentioning that machining tests with a single-crystal diamond tool with a nose radius of r = 0.8 mm and edge radius $r_\beta \leq 0.5$ µm, machined at the same parameters mentioned above, resulted in a surface roughness below R_a = 0.1 µm.

3.2.2.2 Niobium

Paper III [75] reports on experimental tests measuring surface roughness R_a with four different tooling solutions, which were selected based on pre-screening of six different tooling solutions. However, due to severe tool wear of polycrystalline cubic boron nitride (CBN 170) and single-crystal diamond, these tools were excluded from further testing. After further screening, two tooling solutions, PCD and TiAlN – TiSiN coated carbide tools, were selected for extended tests with different cutting parameters. The results from the extended tests are shown in Figure 3.14 and are compared to the theoretical surface roughness calculated according to Equation 3.1. The PCD tool shows mixed results, with the best results obtained for a low cutting speed of v_c = 55 m/min and at a higher cutting speed of v_c = 100 m/min. Figure 3.14a shows the best obtained surface roughness is R_a = 0.46 µm at v_c = 55 m/min and f = 0.025 mm/rev. For the TiAlN – TiSiN coated tool, the surface roughness decreased with increasing cutting speed (Figure 3.14b). Despite better surface roughness results, the PCD tool suffered from rapid tool wear and

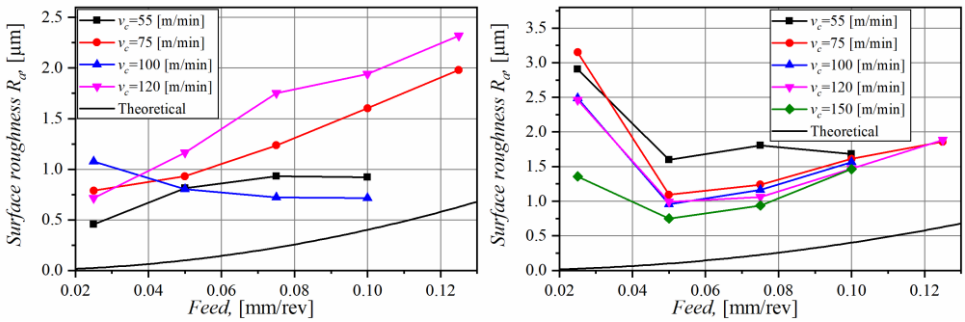

Figure 3.14. (a) Surface roughness at different cutting speeds and feeds for (a) PCD and (b) TiAlN – TiSiN tools.

spontaneous breakage. The experimental roughness measurements are higher than the theoretical surface roughness due to various types of surface damage on the machined surface.

Paper VI [59] reports on extended machining tests under different cutting conditions and evaluation of the resultant surface roughness. The cutting conditions included flood and high pressure (HP) and liquid nitrogen (LN_2) coolants. The cutting speed was also increased as higher cutting speed supported better surface quality. The tools tested in the study were TiAlN – TiSiN coated and uncoated cemented carbide. When flood and HP coolant were used, both tools showed a decrease in surface roughness at cutting speeds exceeding v_c = 150 m/min. The best results were achieved at cutting speeds v_c = 225–250 m/min and feed f = 0.075 mm/rev (see Figure 3.15 and Figure 3.16). Using LN_2 did not significantly improve the surface roughness compared to other cutting conditions, see Figure 3.17. The results indicate that it may be possible to machine Nb with a surface roughness close to R_a = 0.4 µm with coated and uncoated CC tools using flood or HP coolant.

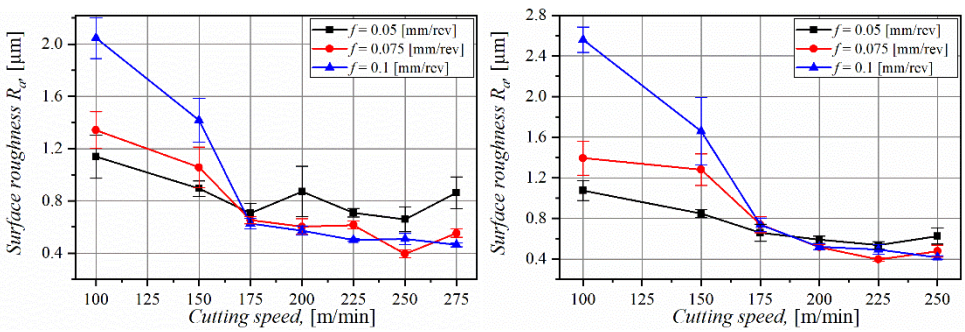

Figure 3.15. Surface roughness R_a for uncoated CC tool, depending on cutting speeds and feeds under (a) flood coolant and (b) HP coolant supply.

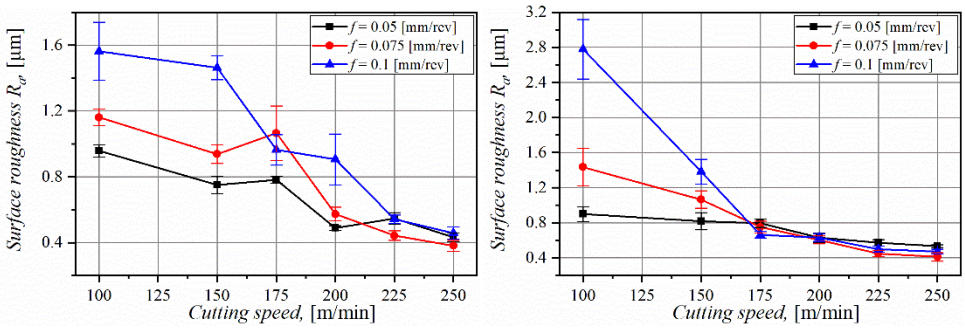

Figure 3.16. Surface roughness R_a for TiAlN – TiSiN coated CC tool, depending on cutting speeds and feeds under (a) flood coolant and (b) HP coolant supply.

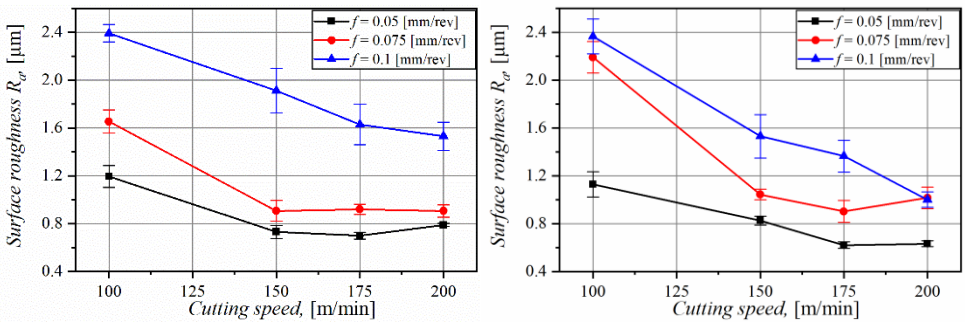

Figure 3.17. Surface roughness R_a depending on cutting speeds and feeds under LN_2 coolant supply when machining with (a) TiAlN – TiSiN coated CC and (b) uncoated CC tool.

3.2.2.3 Tungsten

Tool wear mechanisms during machining of W were the main focus of Papers V [76] and VI [59]. However, surface roughness was also measured to evaluate the surface quality as a function of the wear of the tool. PCD and TiAlN – TiSiN coated CC tools were used in the experiments. The cutting speed was varied while the cutting depth (a_p = 0.3 mm) and feed (f = 0.075 mm/rev) were held constant. In general, the results showed wide variation in surface roughness with cutting length depending on the tool used and different cutting conditions. Figure 3.18 shows that there was a rapid increase in surface roughness from unworn to semi-worn state with the PCD tool. The surface roughness was better when cutting at higher cutting speeds, which were also associated with longer tool life. Figure 3.19a shows the results when using HP coolant, and Figure 3.19b shows the results when using LN_2 coolant. The best surface roughness was achieved with HP coolant; however, HP coolant and flood coolant also yielded the shortest tool life. LN_2 coolant yielded a longer tool life, but the variation in surface roughness was larger. The overall results of the surface roughness from the different cutting conditions range from R_a 1.4–

2.0 µm. These results are rather high considering the mild cutting parameters. However, components made from W for accelerators have a higher limit on surface roughness than OFC and Nb components.

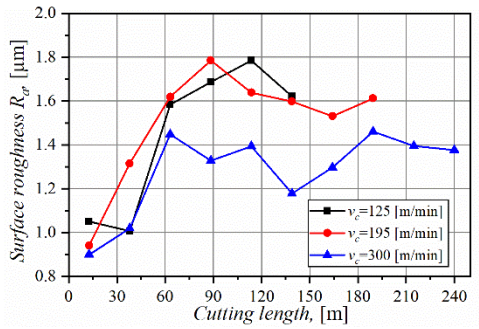

Figure 3.18. Surface roughness, R_a, of the machined surface as a function of cutting length for PCD with HP coolant and different cutting speeds.

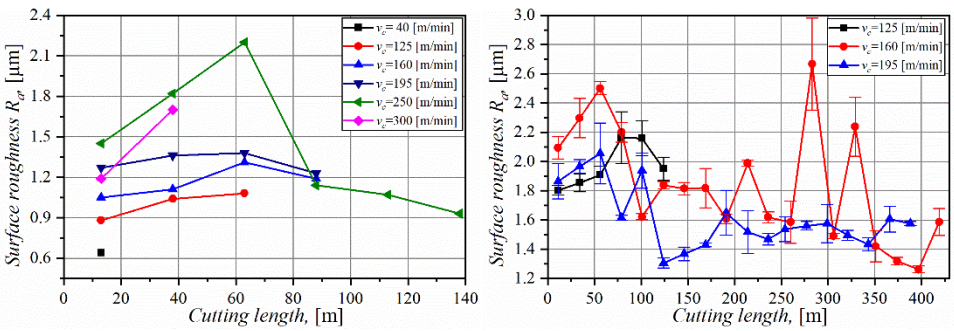

Figure 3.19. Surface roughness, R_a, of the machined surface as a function of cutting length for TiAlN - TiSiN at different cutting speeds for (a) HP coolant and (b) LN_2 coolant.

3.2.3 Surface damage

Machining SPM is challenging due to the extreme ductility or brittleness of the material. Surface damage occurs during machining has a negative effect on the resulting quality. There are different types of surface damage, such as tears, laps, side-flow, redeposited metal, and BUE [33]. The extent of surface damage is closely linked to process parameters, the use of cutting fluid, the tools used, and tool wear, as has been demonstrated when machining Inconel 718 [77-80].

Different types of surface damage appear on the machined surface of ductile material such as OFC and Nb. Samples of the machined surface were cut out with wire EDM, and cross sections in the speed direction were mounted and polished before microscopy. Figure 3.20 shows different types of surface damage on the

surface after machining Nb with HP coolant. Side-flow (Figure 3.20a) produces burrs on the feed mark ridges and is highly dependent on tool wear, cutting speed, feed, type of tool, and nose radius [13]. Side-flow is driven by two mechanisms. The first is a minimum chip thickness effect where uncut material is plowed under and aside the cutting edge. The second is that as tool wear increases, material can flow through the notch on the minor cutting edge to the side of the tool [81]. Tears (Figure 3.20b) appear as small depressions in the surface and occur when the adhesion between the tool flank side and the surface is high enough to tear off material from the surface [82]. Material redeposition or debris was found on the machined surface, which affects the surface quality negatively (Figure 3.20c–d). Pull-out material that is not transported away from the cutting zone with the chip can adhere to the cutting surface [80]. Adhered particles of the residual chip or tool due to elevated process temperatures have also been reported [83]. BUE was found on the machined surface when machining Nb and W, despite the common notion that SPM are not prone to forming BUE [7]. BUE formation from machining of Nb can be seen on the machined surface in Figure 3.21a. This is confirmed by an additional cross-section image (Figure 3.21b). BUE was formed during machining with both PCD and TiAlN – TiSiN coated CC tools.

Under HP coolant supply, BUE formation on the machined surface was more pronounced during machining of W compared to Nb. Figure 3.22a shows a section of the machined surface generated with an unworn PCD tool at v_c = 195 m/min. Uniform feed tracks and the minor presence of surface cracks can be seen in the image. Figure 3.22b shows the machined surface from the same PCD tool in a wornstate, just before reaching VB_{max} = 300 µm. The surface is covered by BUE,

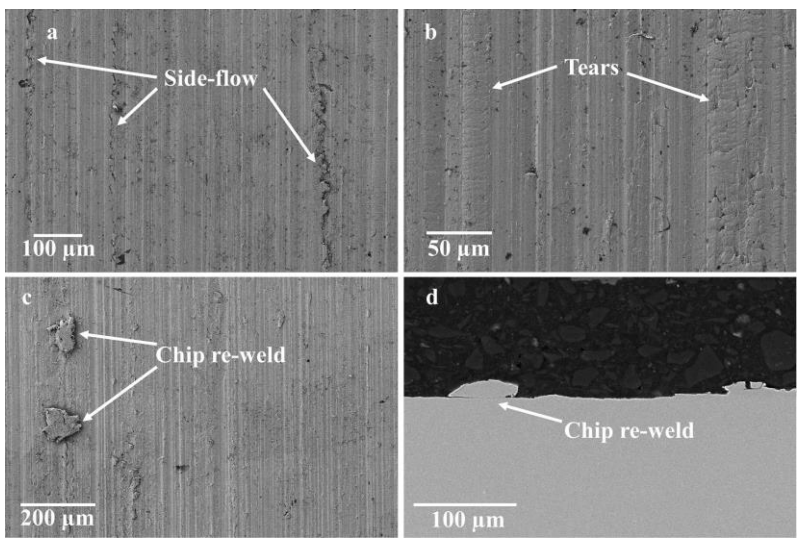

Figure 3.20. Surface defects such as side-flow, tears, and chip re-weld generated by machining.

which explains the rapid increase in surface roughness seen in Figure 3.18. Analysis of the BUEs and surrounding surface reveals a combination of W ductile and brittle deformation mechanisms in the machined surface that can be seen by the typical cleavage surfaces (black rectangle) in Figure 3.22c. A cross section of the machined surface in the speed direction is shown in Figure 3.22d, where BUE heights of up to five micrometers are observed.

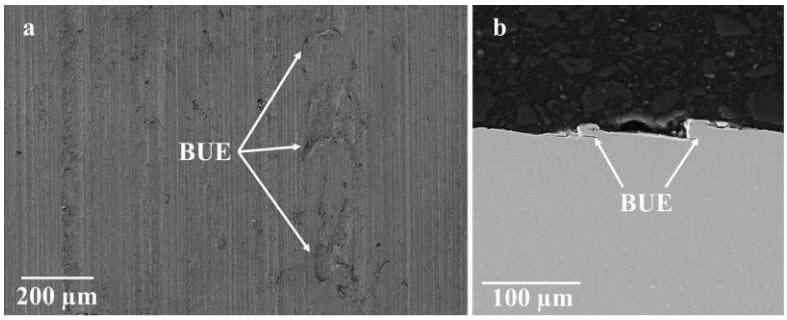

Figure 3.21. BUE defects generated at the machined surface.

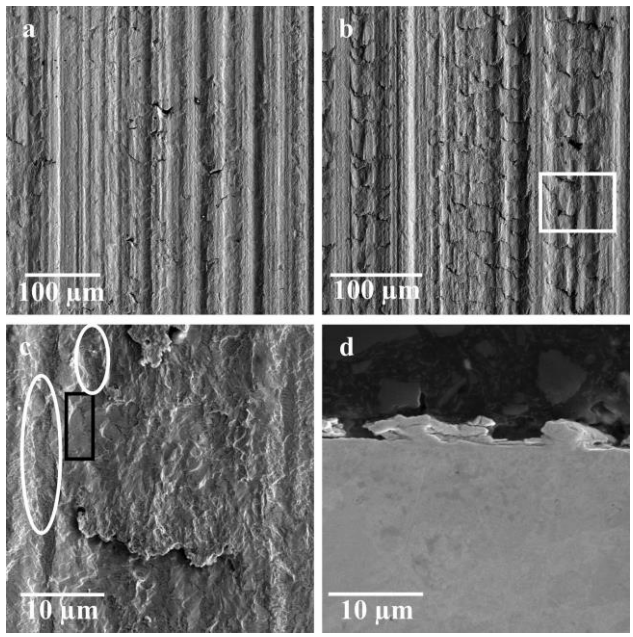

Figure 3.22. SEM images of W surface machined with a PCD tool at v_c = 195 m/min. (a) Machining with unworn tool; (b) BUE formation when machining with a worn tool; (c) BUE surface revealing ductile (white ellipses) and brittle fracture (black rectangle) of W; (d) cross-section view of BUE in the speed direction.

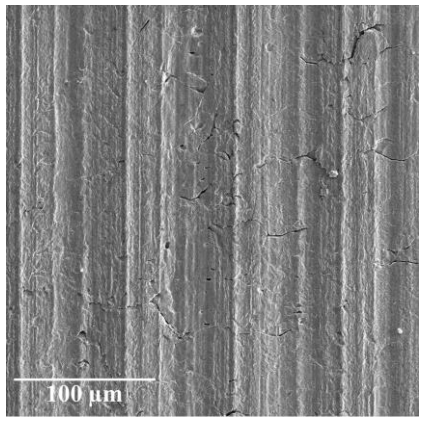

Figure 3.23. Resulting surface for PCD tool at v_c = 300 m/min.

Increasing the cutting speed to v_c = 300 m/min resulted in decreased generation of BUE on the machined surface during cutting with PCD tools. This change is reflected in the improved surface quality seen in Figure 3.23 for higher cutting speeds.

Machining W with TiAlN – TiSiN coated CC tools also led to the presence of BUE, but to a much greater extent. The BUEs are continuously built and broken within the feed tracks (Figure 3.24a). The lower thermal conductivity of the CC tool compared to PCD leads to lower heat dissipation during machining, which can affect BUE formation. Furthermore, abrasion marks can be seen on the top surface of the BUEs, most likely caused by rubbing of the tool's minor cutting edge resulting in rapid tool wear (Figure 3.24b).

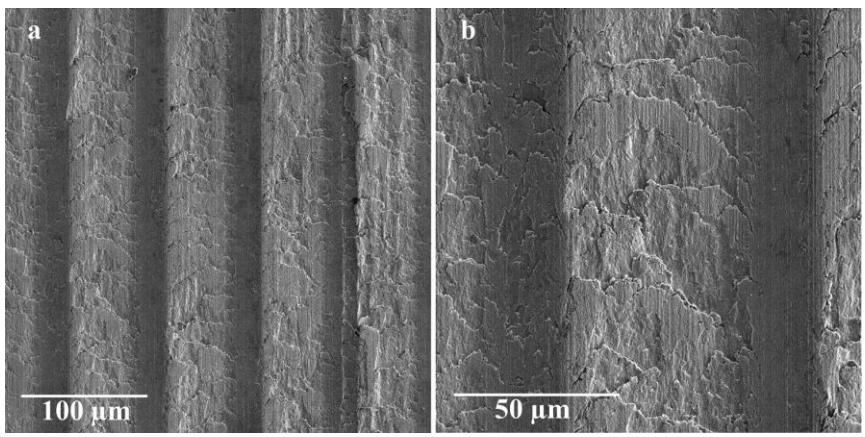

Figure 3.24. (a) SEM image of the machined surface with a TiAlN - TiSiN coated tool at HP condition (v_c = 250 m/min) and (b) detailed view of BUE formation on the machined surface.

Machining W in dry and heated cutting conditions results in an increase in BUE formation on the machined surface compared to HP conditions. Machining a preheated workpiece (Figure 3.25a–b) results in a higher degree of BUE on the surface compared to dry conditions (Figure 3.26a–b). During machining, the formation of BUE in a region is dependent on the process temperature [11]. In the case of dry and especially preheated cutting conditions of W, the increase in BUE formation on the surface indicates that the cutting process is closer to the local maxima of the BUE region than under cooler cutting conditions when HP coolant is used. After the BUE region, the flow zone is entered with a decrease in BUE formation. However, the flow zone is never entered when machining W as the cutting tools fail at increased cutting speed and process temperature.

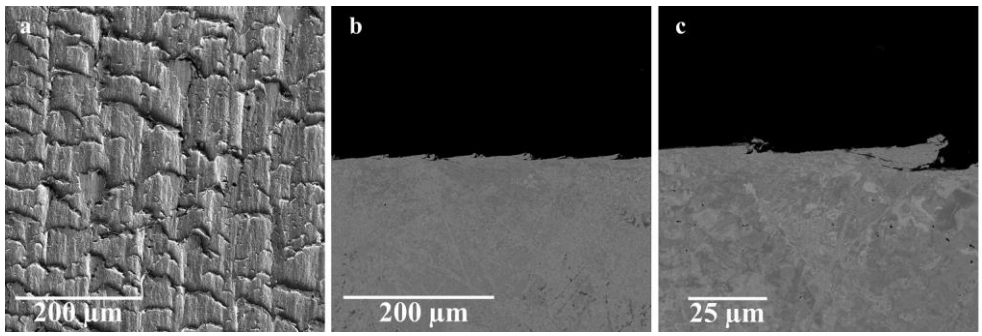

Figure 3.25. (a) BUE formation covering the machined surface (feed direction) for induction-assisted condition (v_c = 125 m/min); (b) cross-section view of multiple BUE formations on the machined surface (speed direction); (c) view of BUE at increased magnification.

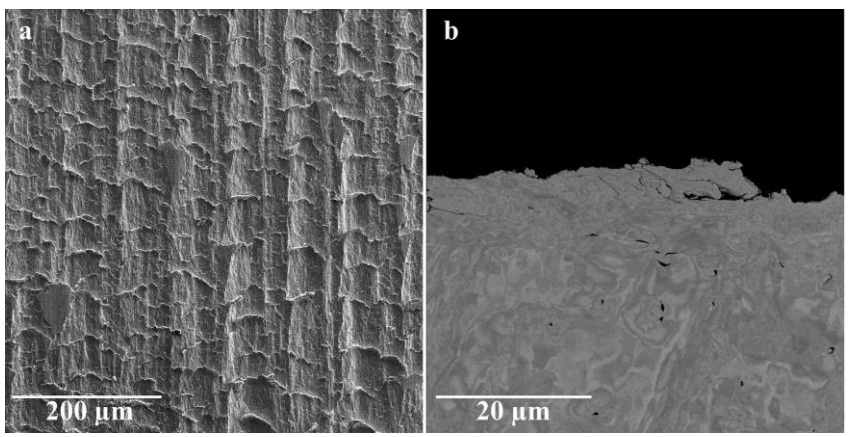

Figure 3.26. (a) BUE formation covering the machined surface (feed direction) under dry cutting condition (v_c = 160 m/min); (b) cross-section view of formed BUE (speed direction).

3.3 Machining-Induced Subsurface Deformation and Defects

3.3.1 Deformation

Deformations can be identified in three zones as described in Section 2.5. Figure 3.27 shows the results from a quick-stop test in copper with three zones, ε. The deformation zone ε_{III} of the newly machined surface will be further analyzed below. The deformation of the machined surface depends on various factors such as workpiece material, tooling solution, tool wear, and cutting parameters. The influence of some of these parameters is discussed and presented below.

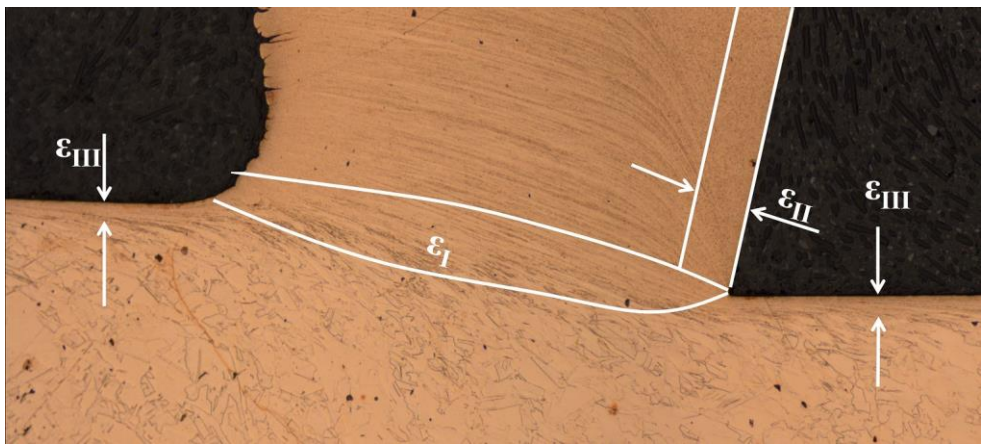

Figure 3.27. Deformation zones in a cutting process.

3.3.1.1 Depth and extent

Subsurface deformation was studied in Papers I [74] and III [75] and analyzed with optical microscopy and hardness measurements. Subsurface deformation was studied in different ways depending on the machined material. Cross sections in the feed direction of the machined material were prepared to study the influence of cutting parameters, tooling solutions, and tool wear. Machining of high ductility material such as OFC and Nb results in relatively deep subsurface deformations. Deformations can be divided into different deformation zones depending on the extent of the affected zone and the distance from the machined surface [79]. The top layer zone ($\varepsilon_{IIIsevere}$) is strongly affected by mechanical loads (frictional force) and thermal loads during machining. It is characterized by heavily deformed microstructure as a result of work hardening. The overall depth of deformed layer (ε_{III}) is identified by bending and shear strain of the grain boundaries or presence of

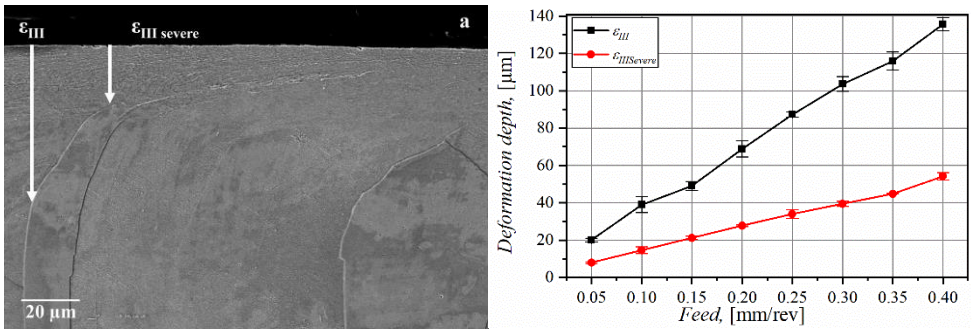

Figure 3.28. (a) SEM image and illustration of deformation depths ε_{III} and $\varepsilon_{III\ severe}$ for OFC; (b) observed deformation depths at different feeds.

slip lines. Deformation zones ε_{III} and $\varepsilon_{IIIsevere}$ are shown in Figure 3.28a from machining OFC at v_c = 150 m/min and f = 0.15 mm/rev. Figure 3.28b shows observations of ε_{III} and $\varepsilon_{IIIsevere}$ at different feeds. The observations show a clear relation between increased feed and deformation depth.

Like OFC, Nb also shows both types of subsurface deformation, which can be divided into ε_{III} and $\varepsilon_{IIIsevere}$. The influence of two tooling solutions, PCD and TiAlN – TiSiN coated CC, on subsurface deformations using different cutting parameters was evaluated, because these tooling solutions maintain sufficient surface roughness and tool life. Figure 3.29 shows that the deformation was more pronounced and deeper when using PCD tools compared to TiAlN – TiSiN coated tools. The results from the visual observations can be seen in Figure 3.30a. The largest deformation depth was observed for the TiAlN – TiSiN tool at v_c = 100 m/min and feed f = 0.025 mm/rev. This exception can be related to a size effect reflecting the ratio between edge radius of the tool ($r_\beta \approx 28$ µm) and the low feed, which can result in a plowing effect instead of cutting. Furthermore, the presence of BUE can contribute to severe deformation, which relates to the poor surface roughness at lower feed (Figure 3.14b). The results show a higher degree of deformation at lower cutting speeds compared to increased cutting speeds. The fact that lower cutting speeds produce better surface quality with the PCD tool is negated by the larger subsurface deformations. A decrease in deformation with increased cutting speed can be explained by the similar behavior of the cutting forces, see Figure 3.30b [75]. The influence of feed is not as clear as in the case of OFC, although the feed test range was not as wide as for OFC, which makes it difficult to compare the results.

In contrast to OFC and Nb, W is a brittle and hard material, which affects the subsurface deformations differently. There is far less deformation than with ductile materials and the deformation affects only the top layer closest to the machined surface. The machined surface was visually analyzed for subsurface deformations as a function of the degree of tool wear in new, semi-worn, and worn PCD tools

during machining. Machining W with a new tool results in a deformation depth of ~2.5 µm. As the tool wears, the deformation depth increases to 9 µm. When the tool wear is close to the tool life criterion of VB_{max} = 300 µm, the deformation depth is close to 12.5 µm (Figure 3.31). Previous publications have studied the degree of tool wear and its influence on increased subsurface deformations during machining of Inconel 718 [84, 85]. When the tool wear increases, the thermal and mechanical loads increase thus affecting the subsurface deformations.

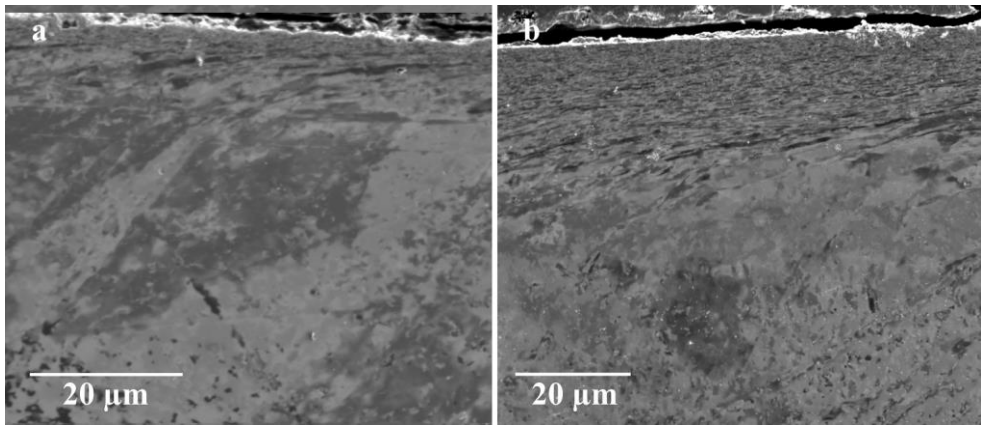

Figure 3.29. SIM electron channeling contrast images of subsurface deformation for (a) TiAlN – TiSiN and (b) PCD tooling (v_c = 100 m/min, f = 0.075 mm/rev) when machining Nb.

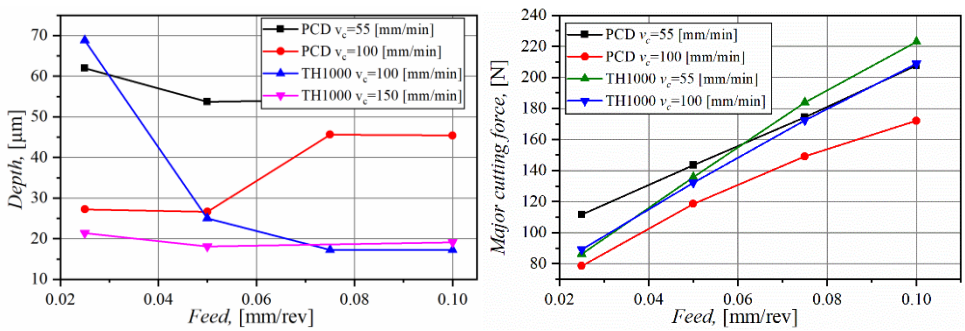

Figure 3.30. (a) Influence of tool materials and cutting conditions on the depth of deformation ε_{III} during machining of Nb; (b) dependence of the cutting force F_c on tool materials and cutting conditions.

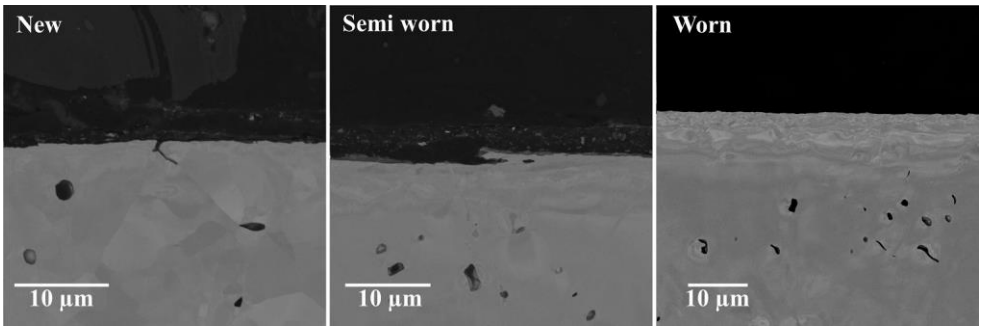

Figure 3.31. Subsurface deformations and the influence of tool wear of the machined W surface.

3.3.1.2 Microhardness variations

Nanoindentation can be used to measure microhardness variations on a very small scale. Small loads are applied to measure the hardness of the material in a localized area, which makes it suitable to measure variations in hardness due to local work hardening. The indentation was carried under a force of 10 mN and was used to create several matrices with 3 columns and 25 rows at different locations on the samples.

Figure 3.32 shows the hardness of OFC samples for different feeds. Unlike with microscopy images, it is not feasible to differentiate $\varepsilon_{IIIsevere}$ with nanoindentation. However, the results show that the degree of work hardening and deformation depth in the bulk material increases with the feed. Discrepancies in hardness can be observed in the near-surface region between the samples. This is due to the higher degree of deformation for the sample machined at f = 0.35 mm/rev. The results correspond to the results from the visual observations in Figure 3.28b. Furthermore, the nanoindentation technique is more accurate than visual observations, a fact that is reflected in the higher values of deformation depth.

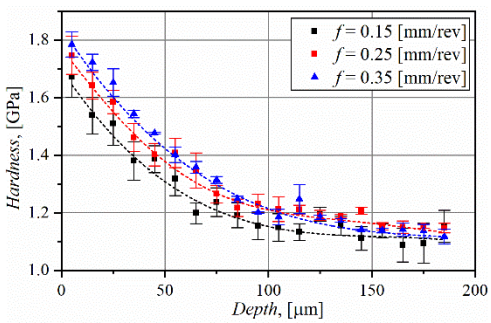

Figure 3.32. Subsurface hardness profile for OFC samples machined at different feeds.

Nanoindentation measurements were performed with two different tooling solutions at two different cutting speeds and four feeds respectively on the Nb samples. Comparing the results from low to high cutting speed for both tools (Figure 3.33a and c) shows that the gradient of decreasing hardness is lower and further to the right for the samples machined at low cutting speed. When the cutting speed increases, the gradient of decreasing hardness increases, and there is a lesser subsurface deformation than at lower cutting speeds (Figure 3.33b and d). This result can be explained by the decrease in cutting force (Figure 3.30b) when the cutting speed increases. In contrast to OFC machining, the influence of feed on the deformation depth for the Nb samples is difficult to detect. The feed range tested is lower than in the OFC machining, although the increase in feed is relatively high between the feeds tested. When machining at low feeds, the machined surface and deformations can be affected by the deformations produced by the next revolution of the workpiece [11]. Furthermore, given the results in section 3.2.3, the surface can be affected by different types of surface damage such as BUE formation. Surface damage negatively influences surface roughness, as can be seen when machining at f = 0.025 mm/rev (Figure 3.14b). This can also explain the high values of hardness for f = 0.025 mm/rev close to the machined surface, and the deviation from lower deformation depths at lower feeds as seen in the OFC machining.

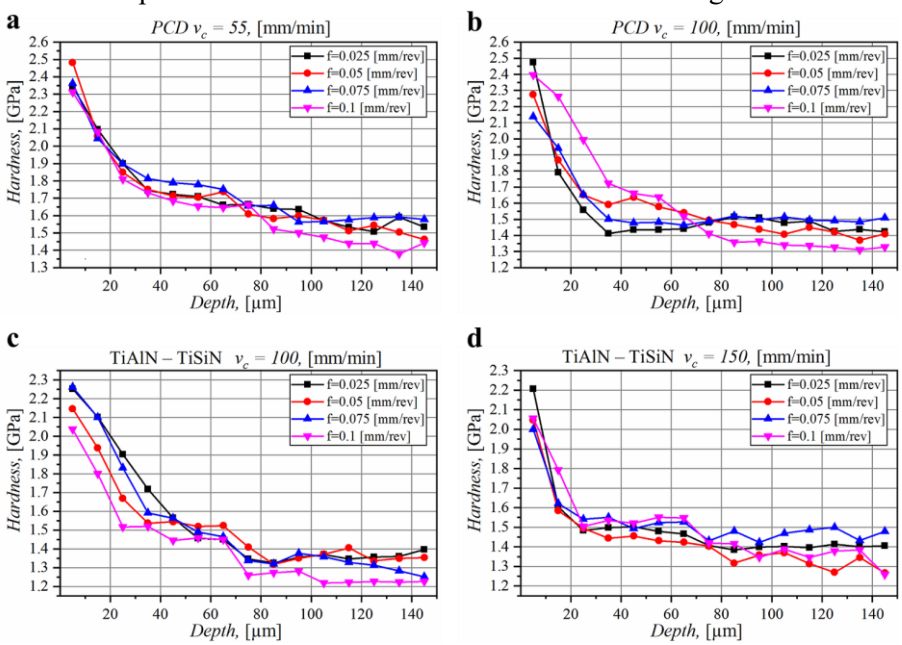

Figure 3.33. Nanoindentation results on the subsurface work hardening for PCD tooling (a) v_c = 55 m/min; (b) v_c = 100 m/min; TiAlN – TiSiN coated tooling; (c) v_c = 100 m/min, (d) v_c = 150 m/min.

3.3.2 Defects

Surface defects were mainly visible on W after the machining. The density of the machined W rod in the experimental tests was 95 %, which results in residual porosity within the microstructure as seen in Figure 2.11b. The porosity (voids) is also observed on the extracted samples of the machined subsurface in Figure 3.34a–b. The voids can serve as crack initiation sites where a crack can propagate along the grain boundary (Figure 3.34b) due to the stresses caused in the shear zone, in some cases linking voids together (Figure 3.34c).

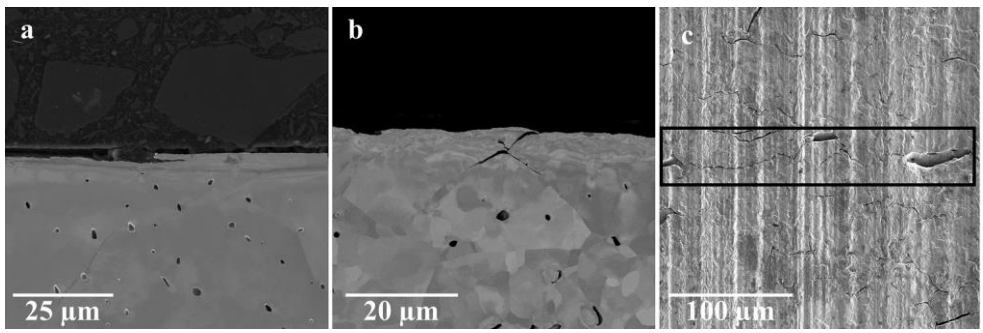

Figure 3.34. SEM images of surface and subsurface damage when machining with a PCD tool at v_c = 300 m/min. (a) BUE formation on the machined surface; (b) crack formation and severe subsurface deformation of the machined surface; (c) network of voids and cracks on the machined surface.

3.3.3 Impact of cutting data on material properties

The relationship between increased subsurface deformation and increased feed observed above was further investigated by machining and testing tensile test rods in OFC. Yield strength data (Rp 0.2) and elongation at break were acquired for tensile rods machined at v_c = 150 m/min and f = 0.05 – 0.40 mm/rev. Selected results from the tensile tests and data collected at different feeds are shown in Figure 3.35a–b. The results from the tensile tests, yield strength and elongation at break, are plotted against the feed in Figure 3.36a–b. The yield strength increases with feed, but elongation at break appears to be inversely related to feed with the exception of feed f = 0.30 mm/rev. One of the test rods at feed 0.30 mm/rev showed significantly lower elongation at break that decreased the average result. Similar behavior of increased yield strength and decreased elongation at break and vice versa have previously been reported during different heat treatments and forming processes of Inconel 718 [86-88], and at different percentages of alloying content of Zn-Al-Cu alloy [89]. The change in material properties is closely related to the microstructure of the material, as the size of the grains or grain refinements, degree of work hardening (material processing), and dislocations influence to the material properties.

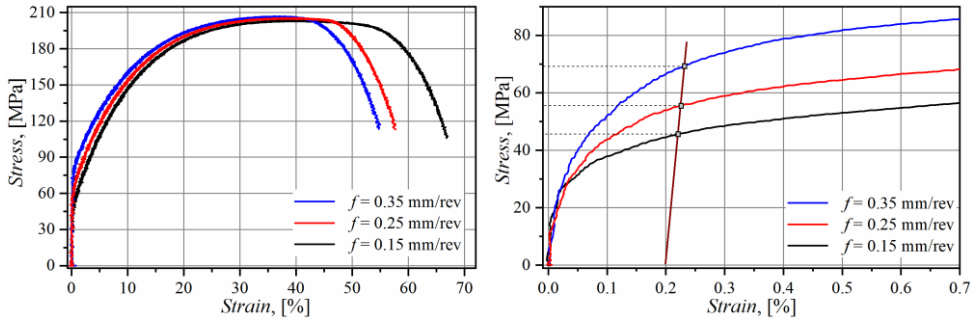

Figure 3.35 (a) Stress-strain curves for OFC samples machined with various feeds; (b) detail of the stress-strain curves in the elastic region.

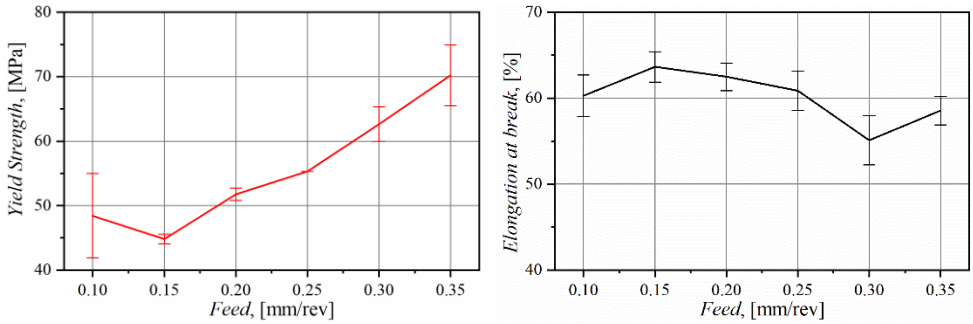

Figure 3.36. (a) Average yield strength for OFC test rods at different feeds; (b) average elongation at break.

As in other machining operations [90], grain refinement was found for both OFC and Nb machining on the newly machined surface (Figure 3.37a–b). This phenomenon is typically associated with dynamic recrystallization (DRX) [85, 90]. When machining at low feeds the deformation on the newly machined surface can be affected by deformation at the next revolution. This could be the case during machining of OFC at $f \leq 0.15$ mm/rev. This could also explain why the yield strength decreases for cases from feed 0.10 to 0.15 mm/rev. At feed 0.10 mm/rev, the surface is more exposed to multiple deformations and the work hardening gradient is higher than at 0.15 mm/rev, which can result in a harder top layer. However, the deformation depth could still be less at feed 0.10 compared to 0.15 mm/rev, as is also indicated in the observed results in Figure 3.36a. The yield strength can still be higher at lower feed because of the harder and deformed top layer. A decrease in yield strength and increase in elongation at break could be the result of a surface that was exposed to less deformation in the previous revolution. When feed increases above $f = 0.15$ mm/rev, the machined surface is not as affected by multiple deformations at different revolutions as at lower feeds. Instead, the deformation depth and resulting yield strength increases due to work hardening of the workpiece.

The resulting increased yield strength with increased feed corresponds to the observed deformation depth in Figure 3.28b and the increased hardness with feed in Figure 3.32.

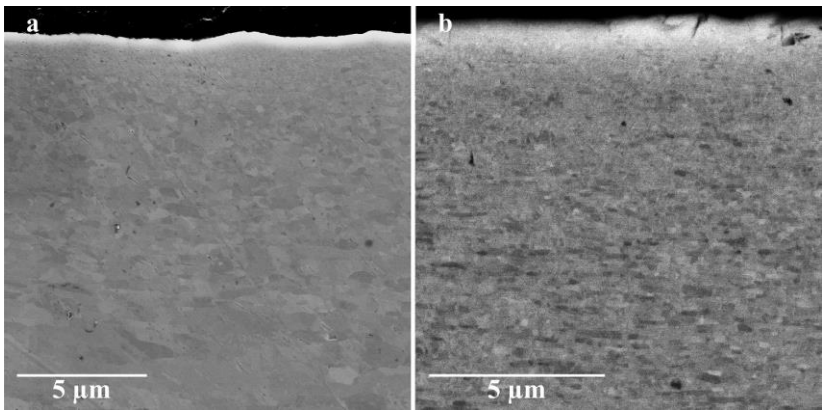

Figure 3.37. Grain refinement at the newly machined surface for (a) OFC and (b) Nb.

3.4 Analysis of Tool Wear

3.4.1 Wear morphology

3.4.1.1 Niobium

The tool is mainly subjected to flank wear with adhesion of Nb on the rake and flank faces during machining. Figure 3.38 compares new and used tools. Further analysis with SEM imaging shows that the worn-out tool can be divided into three sectors on the rake (see Figure 3.39a). In Sector 1 (Figure 3.39b), the tool morphology is as-sintered with Co binder covering the tungsten carbide (WC) particles. This part of the tool has not been subjected to wear. In Sector 2, which is still outside the tool-chip region, the surface shows evidence of adhered Nb on the tool surface. The Co binder and WC particles have been plucked out (Figure 3.39c). The pluck-out is probably due to the Nb chips that adhere and tear off the particles from the surface. However, in Sector 3 within the tool-chip contact zone, pluck-out of particles is not visible due to strong adhesion of multiple layers of Nb on the tool, which acts as a protective layer (Figure 3.39d) [58]. The positive effect of a protective Nb layer is further investigated in section 3.4.2.

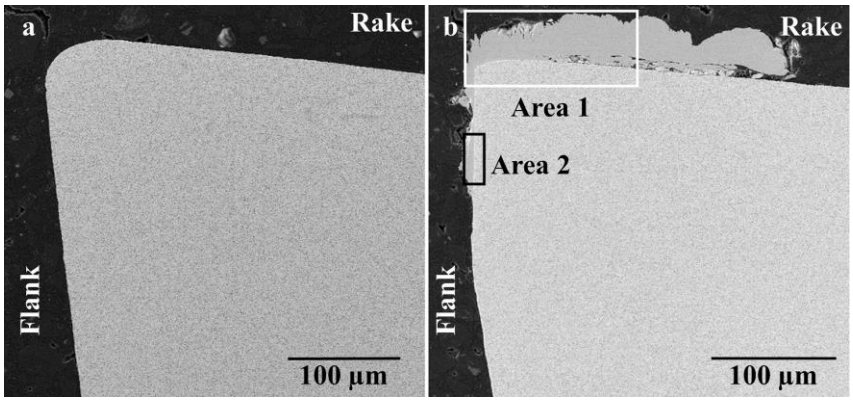

Figure 3.38. SEM images of cross sections of (a) new tool and (b) worn tool with observed Nb adherent layer on the rake and worn flank.

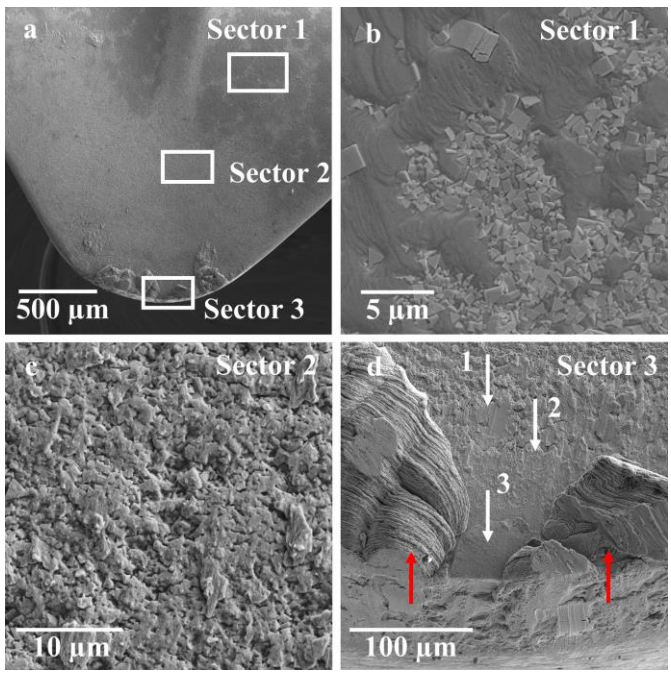

Figure 3.39. (a) Overview of the worn tool rake and details of (b) unworn surface of the tool; (c) adhesion and tool material pluck-out outside tool-chip contact region; (d) strong adhesion of Nb within the contact region (numbered arrows indicate layered build-up of Nb on the tool rake).

3.4.1.2 Tungsten

Several different tooling solutions were tested and evaluated in terms of tool wear and performance when machining W. The majority of the tested tools suffered from

severe tool wear or tool failure in a very short engagement time. Ceramic and cermet tools had the worst performance, as can be seen in Figure 3.40a. Whereas Si_3N_4 and cermet suffered from tool failure, SiAlON, Al_2O_3 – TiC and Al_2O_3 – SiC_W tools suffered from severe but gradual tool wear. The SEM images in Figure 3.40b of the Al_2O_3 – TiC and Al_2O_3 – SiC_W tools show similar wear morphology on the flank and crater wear on the rake. Cutting forces for the Al_2O_3 – SiC_W tool showed a gradual increase (Figure 3.41a), in contrast to the Si_3N_4 tool, which demonstrated high cutting forces almost at tool engagement (Figure 3.41b).

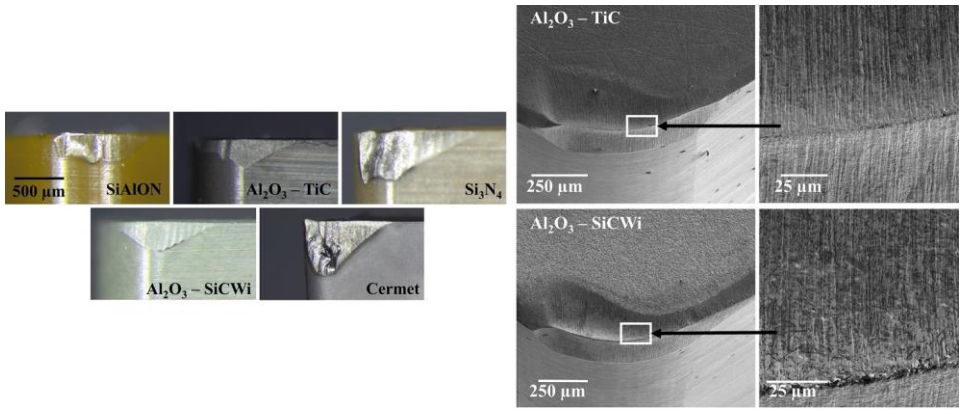

Figure 3.40. (a) Optical images of worn ceramic and cermet cutting tools under best performing conditions: SiAlON, Si_3N_4, and cermet at v_c = 195 m/min, Al_2O_3 – TiC and Al_2O_3 – SiCw at v_c = 40 m/min; (b) SEM of worn Al_2O_3 – TiC and Al_2O_3 – SiCw at v_c = 125 m/min

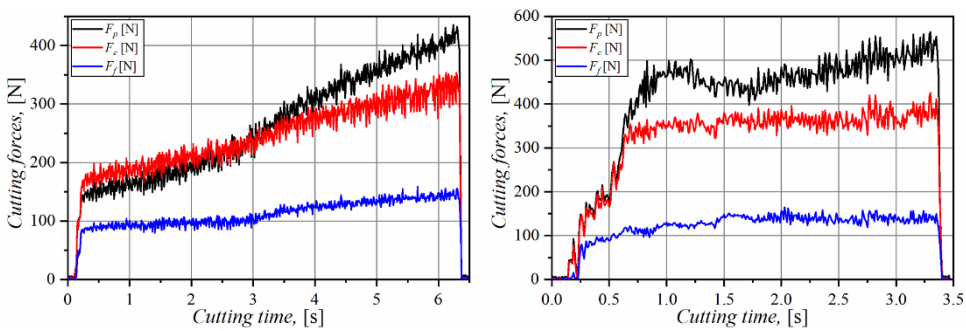

Figure 3.41. Cutting forces at v_c = 195 m/min for (a) Si_3N_4; (b) Al_2O_3 – SiCw tool.

Three different grades of cemented carbide tools were tested: uncoated, (CVD) TiCrN – Al_2O_3 – TiN, and (PVD) TiAlN – TiSiN coated ones. These tools also exhibited intensive wear on the flank and the rake wear, yet flank wear was less for the CVD- and PVD-coated tools compared to the ceramic tools. The uncoated and ceramic tools had similar results. Signs of plastic deformation occurred at speed of

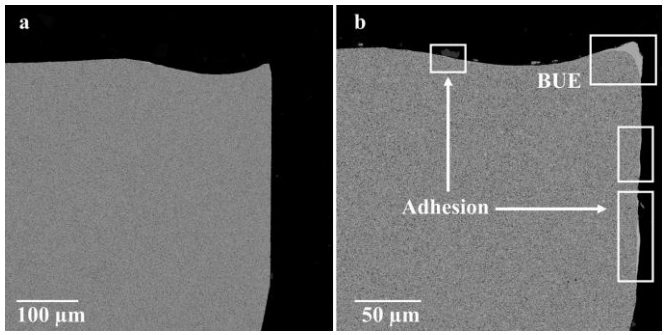

Figure 3.42. Backscatter electron images of carbide tool cross section worn at (a) low cutting speed of v_c = 40 m/min and (b) high speed of v_c = 125 m/min.

v_c = 195 m/min and tool failure occurred at above cutting speeds. Further analysis and cross sectioning was performed for the uncoated CC tools. Figure 3.42 shows there is no adhered W on the tool machined at v_c = 40 m/min; however, substantial crater and flank wear is visible. At increased cutting speed v_c = 125 m/min, BUE along the edge line and adhered W on the flank and rake are visible [76].

SEM images of the uncoated (Figure 3.43) and PVD-coated (Figure 3.44) tools show the resulting flank wear and crater wear on the rake. Adhesion of W in the form of BUE (Figure 3.43b and 3.44b) can be seen along the edge line; however, for the PVD-coated tool, the presence of adhered W is not visible further up on the rake (see Figure 3.44c). Furthermore, wear tracks on the minor cutting edge corresponding to the feed are visible on the flank face of the PVD (Figure 3.44a) and CVD-coated tools. Such wear tracks are typically attributed to superficial plastic deformation of the tool material on the minor cutting edge against the side-flow or other machined surface defects, abrasion [91], or adhesive wear. At cutting speeds exceeding v_c = 250 m/min, the cutting temperature increases, which results in plastic deformation, chipping, and tool fracture [92-94].

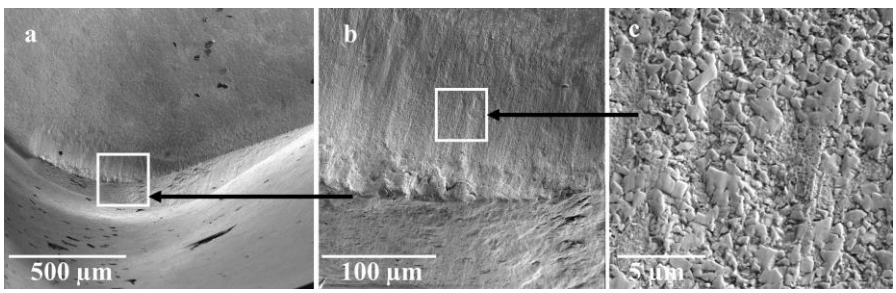

Figure 3.43 (a) SEM overview of a worn uncoated carbide tool (v_c = 125 m/min); (b) increased magnification view of rake and flank wear; (c) high magnification image of the wear scar inside the crater.

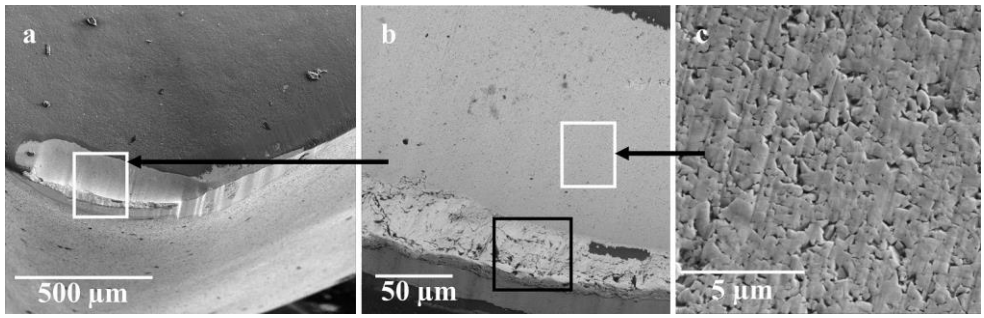

Figure 3.44. (a) SEM image of the worn-out PVD-coated tool (v_c = 160 m/min); (b) higher magnification of crater showing adhesion of W BUE (black rectangle); (c) detailed view of the wear scar in the crater.

Two different PcBN grades with low (CBN 010) and high (CBN 200) cBN content were tested. Like the ceramic tools, the CBN 010 tool suffered from severe tool wear. The CBN 200 tool showed better results with reduced flank wear compared to CBN 010. Further analysis with SEM imaging of the CBN 200 revealed significantly less crater wear compared to the other tool materials (see Figure 3.45a). Figure 3.45b shows large BUE formation along the edge line, which is also seen in the cross section of the tool. Here, the chamfer of the tool is still visible underneath the adhered BUE, which protects the edge line from further wear.

Of all the tested tools, the PCD tool showed the best results in terms of tool life. The flank wear is uniform, but signs of flaking or microchipping of the tool were noticed (Figure 3.46a). Moreover, SEM images reveal significant cratering and irregular adhesion of W (see Figure 3.46b). Macro and micro grooves were also seen on the worn flank [76].

Based on the results from the screening test, the tool life of the PVD TiAlN – TiSiN coated tool was further evaluated with different machining strategies including cryogenic coolant (LN_2), induction-assisted heating (IAM), flood coolant, and dry.

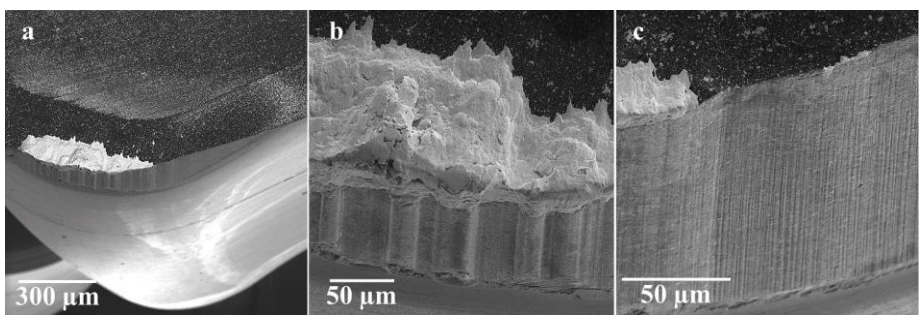

Figure 3.45 (a) SEM image of worn-out CBN200 tool (v_c = 195 m/min); (b) adhered W and BUE formation on the rake; (c) abrasive scratches on the flank of minor cutting edge

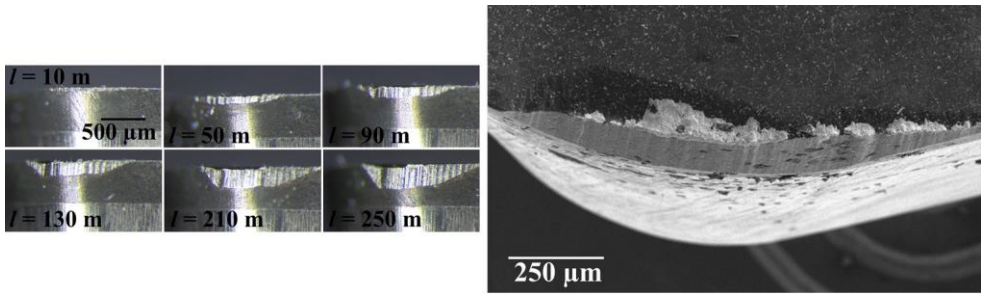

Figure 3.46. (a) Progression of flank wear of PCD at different cutting lengths (v_c = 300 m/min); (b) SEM image on rake side of worn PCD tool (v_c = 195 m/min).

Figure 3.47a shows an overview of the worn-out tool after cryogenic machining at v_c = 160 m/min. Adhered W in the form of BUL covers the crater on the rake side, and the size of the crater is larger compared to that with high pressure (HP) coolant (Figure 3.44). The central part of the crater has unstable adherence of W. Signs of adhesive pluck-out of WC fragments are visible in the centrat part of the crater (see Figure 3.47c–d). At the tool nose, adhesion of BUE is visible and also the edge chipping, which is the result of continuous build-up and removal of BUE (Figure 3.47a). On the flank side, grooves proportional to the feed are also found on the minor cutting edge as in the case of HP machining.

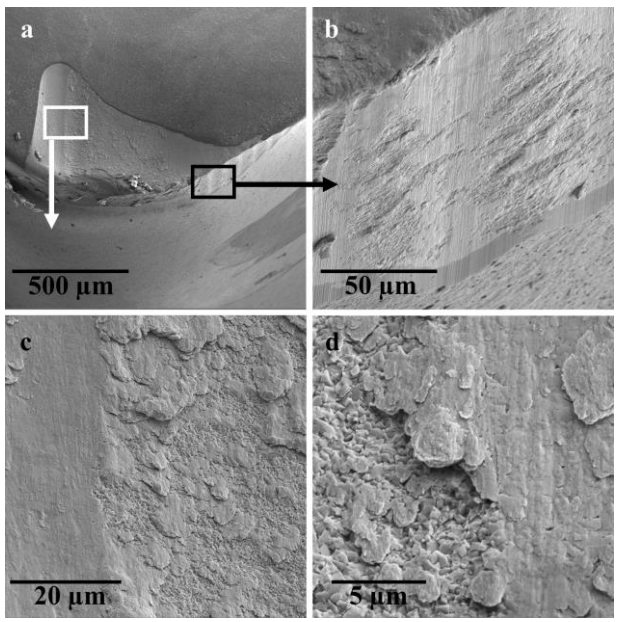

Figure 3.47. (a) Overview of a worn-out TiAlN – TiSiN-coated tool at v_c = 160 m/min; (b) increased magnification of flank wear on the minor cutting edge; (c–d) close-up view of tungsten adhesion and adhesive WC grain pluck-out within the crater.

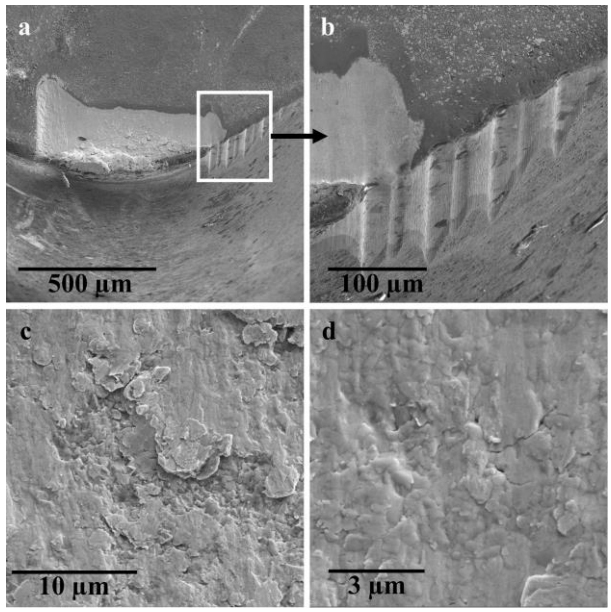

Figure 3.48. (a) Overview of a worn-out PVD coated tool for hybrid induction-assisted machining at v_c = 125 m/min; (b) higher magnification view of flank wear on the minor cutting edge; (c–d) wear surface within the crater reflecting uniform adhesion and adhesive pluck-out of tool material.

SEM images of the worn-out tool at v_c = 125 m/min and IAM condition are shown in Figure 3.48. Strong formation of BUE in the tool nose region can be seen in Figure 3.48a. In comparison to LN_2 machining, the length and the depth of the crater on the rake are smaller in size. The crater is more uniformly covered with adhered W, which can be a result of the increased ductility of the workpiece due to the higher process temperature. Furthermore, the adhesive pluck-out of WC grains is limited (Figure 3.48c). Flank wear on the major cutting edge is smaller compared to LN_2. However, the grooves formed on the flank side are more distinct in comparison (Figure 3.48b).

As with induction-assisted machining (IAM), the ductility and process temperature increases in the W workpiece when machining in dry conditions without a coolant. For dry machining case, the formation of BUE on the tool nose region and adhesion of W in the crater are similar to IAM (Figure 3.49a). However, pluck-out of WC particles due to adhesion is more pronounced. On the flank, grooves on the minor cutting edge and wear on the major cutting edge are similar to IAM.

Flood coolant shows similar results to HP coolant (see Figure 3.50a–b). BUE is clearly seen at the tool nose, as are the grooves on the flank. The surface in the crater is smooth, the WC grains are clearly visible, and there is only small amount of adhered W (Figure 3.50c).

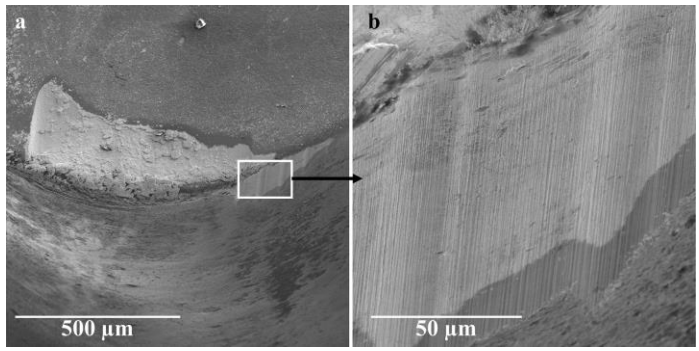

Figure 3.49. (a) Overview of a worn-out PVD-coated tool at v_c = 160 m/min in dry cutting; (b) increased magnification view of flank wear on the minor cutting edge.

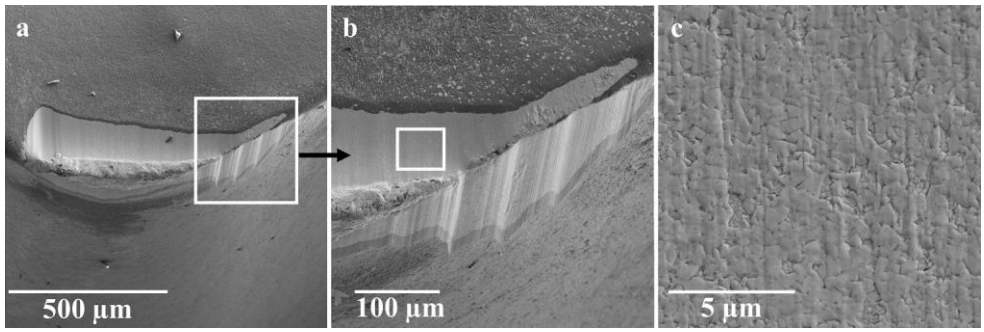

Figure 3.50. (a) Overview of a worn-out PVD-coated tool using flood coolant at v_c = 195 m/min; (b) increased magnification of flank wear region; (c) wear surface of the crater at the rake.

3.4.2 Wear mechanisms

3.4.2.1 Niobium

Further attention was directed to the adhered Nb on the flank side that was seen in Area 2 of Figure 3.38b, because the dominant wear of the tool occurred in this region. Grain refinement due to severe plastic deformation is seen in the adhered layer of Nb (Figure 3.51a). The flow direction at the tool/workpiece interface is also visible, which indicates that the adhered Nb is being continuously replaced throughout the cutting process. However, no signs of WC grain pluck-out are visible on the flank as opposed to the rake, thus excluding an adhesive mechanism of the flank wear.

A TEM lamella was extracted in the area of adhered Nb on the flank for further examination. A thin layer (~50 nm) was identified between the bulk of Nb and WC grains (see the circle in Figure 3.51b). The results from the electron diffraction

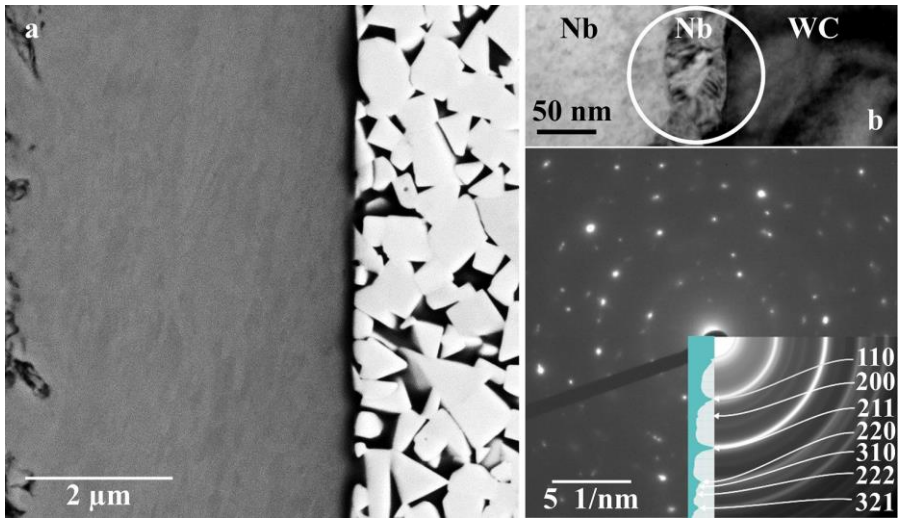

Figure 3.51. (a) Backscatter image of adhered Nb on the wear land; (b) bright field TEM image of the WC and Nb interface on the flank wear land and respective selected area diffraction.

(SAED) pattern showed a BCC symmetry and lattice parameters equivalent to Nb. This layer is probably formed at tool disengagement and cooling, resulting in recrystallized Nb or alternatively in a solid solution of Nb and W, as both share BCC lattice type. Furthermore, the appearance of the WC grains is smooth, which implies that the main wear mechanism on the flank is diffusional dissolution of WC and Co in the adhered Nb.

On the rake, the surface appears to be rough under the adhered Nb, as seen in Figure 3.39. Figure 3.52a shows a magnified view of Area 1 in Figure 3.38b. In the area marked with a black rectangle, there are blocks in a mix of crushed WC grains, Co, and Nb under the lowest adhered layers of Nb (Figure 3.52b). These blocks were presumably plucked out at tool engagement due to adhesive wear and transported further back along the rake in the chip flow direction until they were re-welded on the tool and covered in later layers of adhered Nb. The pluck-out and adhesion wear process slows down when several layers of adhered Nb are formed and eventually protect the tool from further adhesive wear. Closer inspection of the rake in Zone 1 in Figure 3.52a shows a continuous interaction layer of approximately 400 nm thickness at the interface between tool and adhered Nb (see Figure 3.53a). There is a similar interrupted interaction layer of approximately 600 nm thickness (Figure 3.53b) further back on the rake in Zone 2.

This interaction layer was analyzed in a TEM combined with XEDS mapping. The TEM image shows a layer between the adhered Nb and the Co binder of the tool (Figure 3.54a). Together with the XEDS data, the interaction layer shows an overlap of carbon in Nb, indicating the formation of niobium carbide (NbC) (Figure 3.54c).

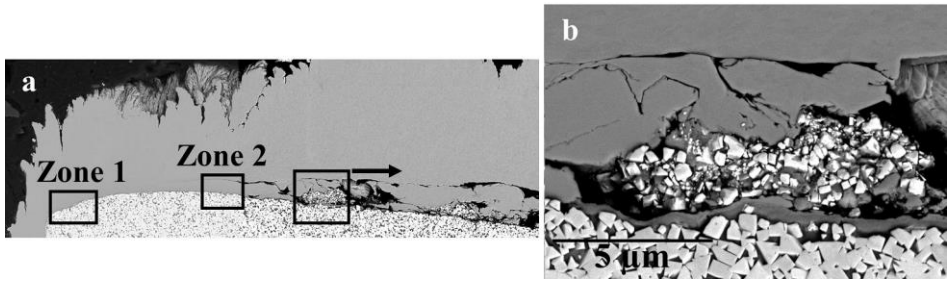

Figure 3.52. (a) SEM image of overview of Nb adhesion layer on the tool rake; (b) locked cemented carbide particles between adhered layers of Nb.

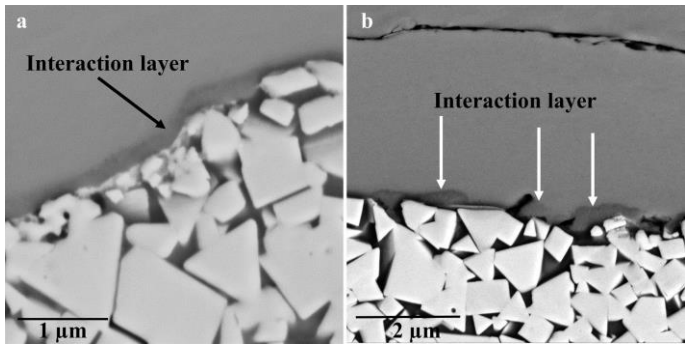

Figure 3.53. Backscatter image of (a) continuous interaction layer (dark gray) in the vicinity of edge radius; (b) semi-interrupted interaction layer (dark gray) in the upper region of the rake.

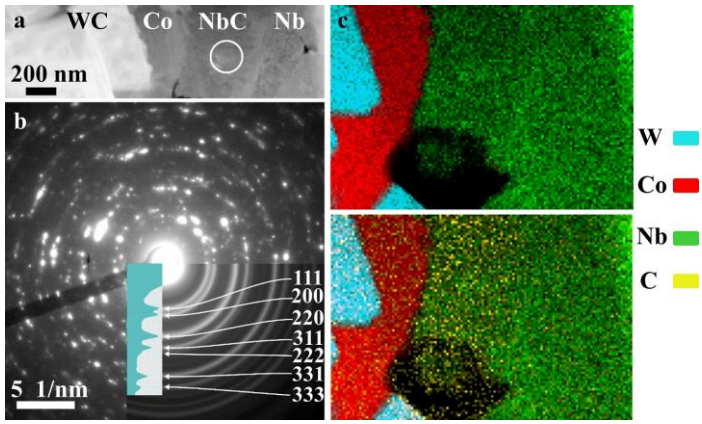

Figure 3.54. (a) Bright field TEM image of the interaction layer between WC and adhered Nb on the tool rake; (b) respective selected area diffraction of the NbC reaction product; (c) XEDS mapping of interaction layer.

The formation of NbC also agrees with the SAED pattern of FCC symmetry and lattice parameters. After this NbC layer has formed on the rake, the wear progression reduces significantly and the NbC layer acts as a barrier and blocks any further diffusional wear. Thus, chemical wear mechanism is active in the formation of a NbC tool protective layer (TPL), where the WC grains act as a source for carbon [58]. Formation of TPL has previously been reported during machining of materials such as Inconel 718 [95], Ti-6Al-4V [96, 97], Al-Si-SiC metal matrix composite [98], Si-brass [99], and Al-alloyed white cast iron [100].

The question is why a TPL layer can be formed on the rake and not on the flank. The extracted cross-sectioned tool sample was further polished and examined with SEM. After adjusting the image brightness and contrast, a more distinct pattern of material flow in the adhered Nb became visible, from the tool edge and over the rake (see Figure 3.55). At the beginning of the cut, crushed WC particles are plucked out and transported over the rake as described above. Over time, an adhered layer of Nb stagnates and creates a steady state interface next to the tool surface where the material flow is non-existent or close to zero. In this layer, the concentration of carbon as a result of diffusion from the WC will continue until saturation when NbC is formed (Figure 3.53a). The same phenomenon is seen further back on the rake, between Zones 1 and 2 in Figure 3.53b, where a no-flow zone exists without any signs of material flow. In the next adhered layers, the material will continue to flow over the stagnation layer, which is clearly seen in the flow zone in Figure 3.55. On the flank side, a continuous flow of adhered Nb was seen, and thus the carbon concentration cannot saturate to form a protective NbC layer. Therefore, diffusional dissolution will continuously wear out the tool on the flank [58].

NbC formation is highly dependent on the temperature and the carbon activity in the cemented carbide. Temperature measurements of the machining process during machining of Nb showed that temperatures may be above 1000 °C on the tool/chip interface. Calculations using Thermo-Calc and database TCFE9 showed that the carbon activity increases with increased temperature. Figure 3.56 shows the driving

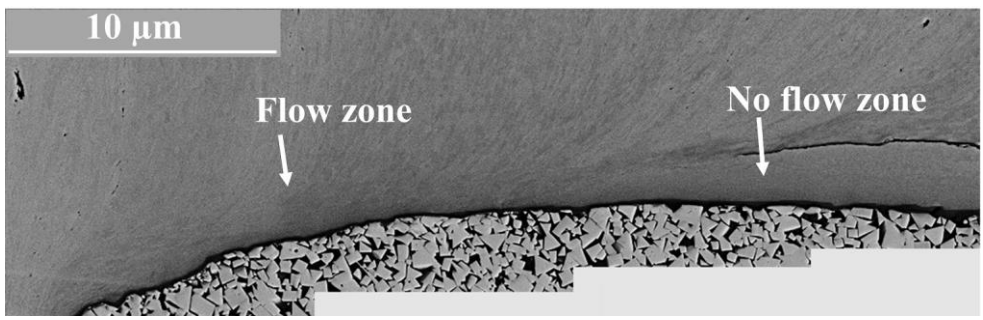

Figure 3.55. Backscatter electron image of Nb material flow on the rake face of the tool.

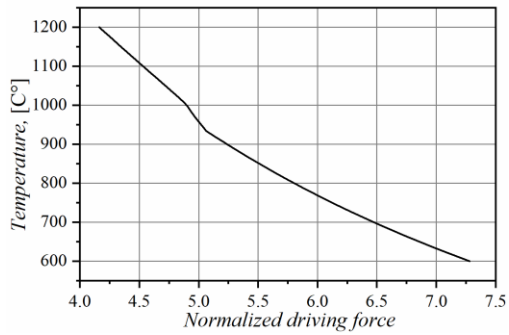

Figure 3.56. Normalized driving force for NbC formation in the Nb workpiece.

force (DGM) for NbC formation calculated as a function of temperature by applying the carbon activity in CC on pure Nb . It can be seen that the driving force decreases with temperature. However, the driving force for NbC formation is very high, and thus NbC will form at all temperatures. The formation rate of NbC is also dependent on the carbon flux from the CC to the Nb workpiece. In this case, the carbon transport will mainly be from diffusion of C in the Co binder, although C can also be transported from dissolution of WC. The calculations for carbon flux can be found in Paper IV [58].

Diffusion couple samples were made to further study the interaction between Nb and uncoated CC. The samples was prepared according to Ref. [101], and details of the high pressure and high temperature (HP-HT) treatment process can be found in Paper IV [58].

Figure 3.57 shows that there are two regions of interest with different interaction types at the CC base on the cross-sectioned sample. In Region 1, an interaction layer of approximately 300–400 nm thickness was found (Figure 3.58a) that is visually similar to the NbC layer on the tool (Figure 3.53a). Figure 3.58b shows that when combining STEM and XEDS data, the TEM sample has large WC grains and

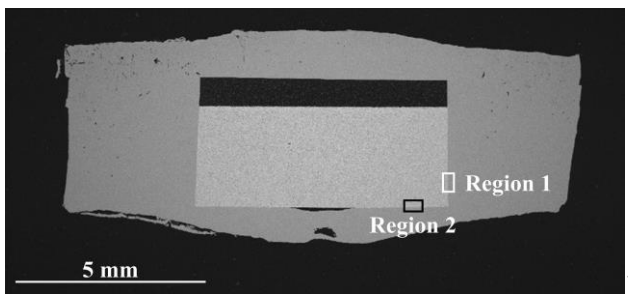

Figure 3.57. Backscatter image of the diffusion couple cross section.

crushed WC grains covered by Co binder in contact with a NbC interaction layer. This is in line with the results from the NbC interaction layer formed on the tool. 1D Dictra [102] simulations were performed for the diffusion couple in Region 1. The results show that a NbC layer can form at the specific temperature and pressure of the diffusion couple (see Figure 3.59). However, the thickness of the NbC layer (approximately 3 µm) is larger than the experimentally observed values.

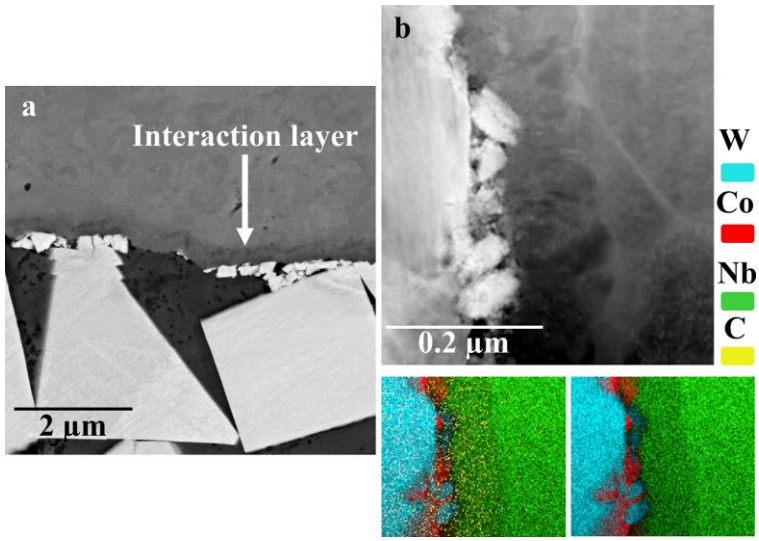

Figure 3.58. (a) Backscatter image of the interaction zone for Region 1; (b) STEM HAADF image of the interaction layer from Region 1 of the diffusion couple and XEDS mapping.

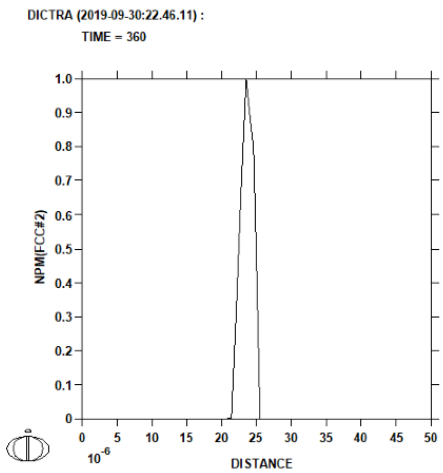

Figure 3.59. 1D diffusional Dictra simulations predicting formation of NbC in Region 1 of the diffusion couple.

Region 2 shows not only an interaction layer comparable with the interaction layer on the tool (Figure 3.53a), but also a layer of needle- or platelet-shaped particles (Figure 3.60). Further TEM analysis shows that the interface between the CC tool and adhered Nb can be divided into five separate zones: (i) original CC (WC – Co); (ii) nanocrystalline WC platelets in Co matrix; (iii) nanocrystalline WC platelets in Co_3W_3C η – phase matrix; (iv) NbC reaction product; and (v) recrystallized Nb (Figure 3.61). The formation of WC nanoplatelets, Co_3W_3C η – phase matrix, and the intensive dissolution of original WC grains could be interpreted as indicative of potential formation of liquid phase in Region 2, likely due to lower temperature eutectic between interacting elements [58]. The question is why the reactions are different in Region 1 and 2 of the same diffusion couple. The reactions in Region 2 show signs of increased temperature compared to Region 1. Examining the cross-sectioned sample in Figure 3.57 shows that there are signs of a slight axial compression of the capsule, which shortens the distance between the graphite heater and the underside of the Nb capsule. Temperature calculations showed that there is a temperature difference of possibly as much as 30 °C between the cylindrical and bottom surface due to the axial distortion. The difference in temperature distribution can explain the different interactions in Region 1 and 2. Furthermore, the results indicate that there is an upper limit of the NbC TPL where a liquid phase might form. This can lead to a loss of mechanical strength or the formation of a Co_3W_3C η – phase, which is known for its low toughness [58].

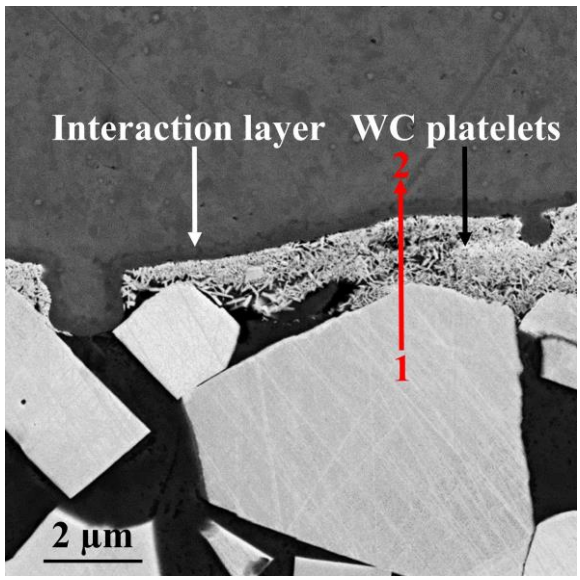

Figure 3.60. Backscatter image of the interaction zone for Region 2.

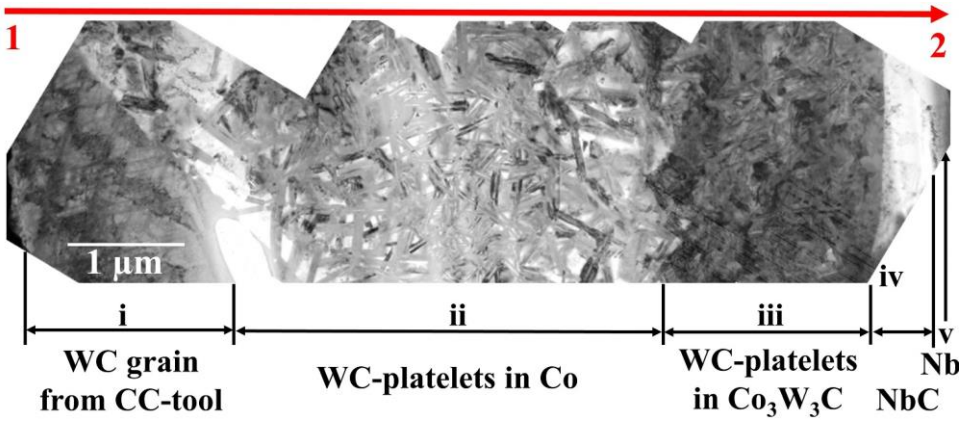

Figure 3.61. STEM LAADF overview image of five different interaction zones within Region 2 of the diffusion couple.

3.4.2.2 Tungsten

Several different tooling solutions were tested as described above while machining W. Tool wear mechanisms were further analyzed for most of the tools that did not suffer immediate tool breakage.

Figure 3.40b shows images of Al_2O_3 –TiC and Al_2O_3 – SiCw worn tools. Macroscopic grooves along the chip flow direction can be seen on both the flank and rake side of the tool, which indicates an abrasion wear mechanism. The presence of such grooves is usually correlated with hard inclusions in the workpiece material [103]. W is a hard and abrasive metal, and the dimension of the grooves are comparable with the grains size of W shown in Figure 2.11b. At increased magnification, the presence of small localized packets of grooves in submicron size affecting the Al_2O_3 matrix can be seen (Figure 3.62). However, these microscopic grooves are not directly the result of abrasion as their scale is too fine compared to the size of abrasive material. There have been reports of tool degradation due to superficial plastic deformation of alumina-based ceramics [104-106]. Therefore, abrasion combined with plastic deformation are two likely mechanisms forming the grooves.

Further analysis of the Al_2O_3 – SiCw tool in Figure 3.62 reveals cavities on the tool surface, which is a result of degradation of SiC whiskers. SiC whiskers are 50 % harder than the Al_2O_3 matrix [11] and degradation due to abrasion is unlikely. A previous study showed degradation of SiC whiskers due to oxidation and diffusional dissolution during machining of ferrous alloys [91]. The solubility of Si in Fe is high, leading to diffusional dissolution of Si into the workpiece material and Fe into the SiC whiskers. However, the solubility of Si in W in the temperature range 1000–1100 °C is insignificant, or close to non-existent. Accordingly, the dominant wear

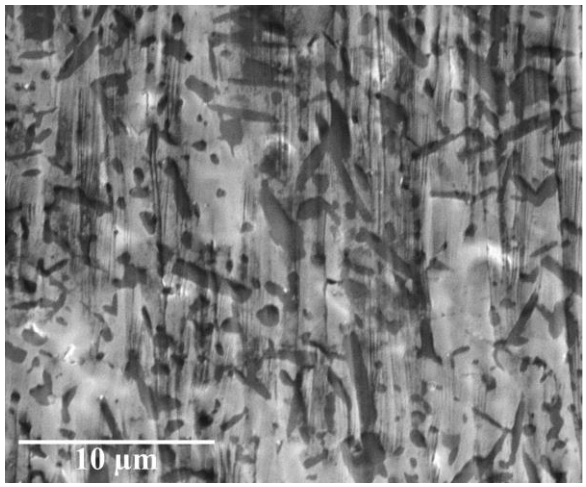

Figure 3.62. High magnification SEM image of the crater of Al_2O_3 – SiCw tool (v_c = 125 m/min).

mechanism of ceramic tools is oxidation of the SiC whiskers and abrasion of the Al_2O_3 matrix.

Grooves are not as clearly visible on the worn tool surface in the SEM images of the uncoated CC tool as for the ceramic tools. Due to the lower hardness of the tool material, an abrasion mechanism could be expected. However, other mechanisms are most likely also present.

Examination of the cross section of the worn-out tool reveals that the tool material loss is lower in the BUE region compared to the tool crater and flank (see Figure 3.63a). Furthermore, material flow can be seen in the upper region of the BUE with W grain texturing. There is stagnation of the adhered workpiece material with grain refinement and lack of flow pattern closer to the tool–BUE interface, which results in retardation of the diffusional wear mechanism (Figure 3.63b) [76]. The same pattern was also found during machining of Nb. Analysis of the rake and flank also reveals fragmentation of WC particles at the tool surface (see Figure 3.63b–d). The fragmentation can be a result of the presence of adhesive wear during BUE build-up and detachment of adhered material. Detachment of tool fragments can also be a result of diffusional loss of the Co binder, weakening the WC grain bonding [99]. Furthermore, fragmentation of WC particles can also occur when the tool is subjected to dynamic impact of discontinuous chips during machining [107].

The texturing of the W grains on the flank side shows a flow pattern of the adhered W (see Figure 3.63c–d). Cracking and fragmentation of WC grains is present, and the fragments are transported away by the adhered metal, thus indicating an adhesive wear mechanism [96]. The morphology of the fragments appears smooth with rounded edges, indicating coexistence of a diffusional mechanism.

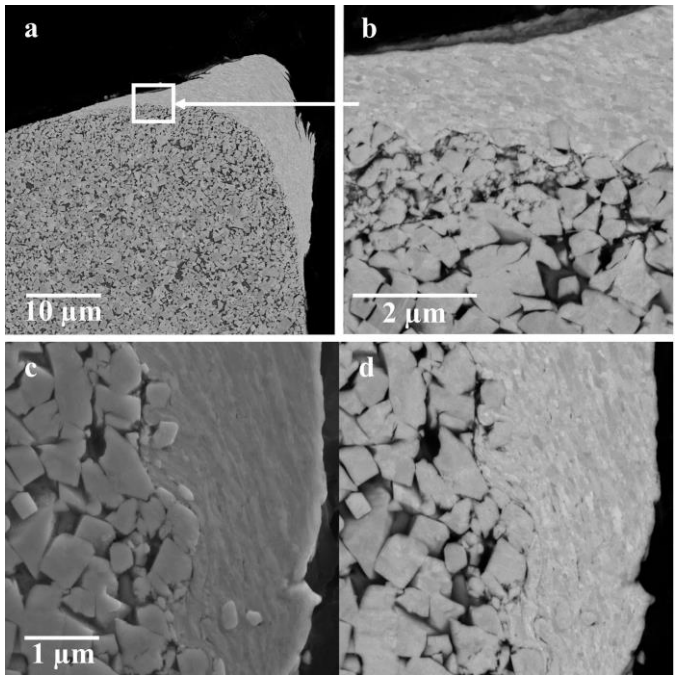

Figure 3.63. Backscatter electron images of (a) BUE region and (b) detailed view of tool–BUE interface on the rake; (c) secondary and (d) backscatter electron images of adhered W on the flank wear land.

The region with adhered W on the flank was further analyzed by extracting a TEM lamella with the FIB lift-out technique. Figure 3.64a shows three regions that potentially point to different tool wear mechanisms. In Region 1, the Co binder between two adjacent WC grains is subjected to diffusional dissolution and the WC grains also show signs of partial diffusional dissolution. Examples of cracking and deformation of WC grains can be seen in Region 2 (Figure 3.64b). Due to the coverage of adhered W on the flank, an abrasion mechanism is unlikely to be active. Instead, plastic deformation and shearing under excessive contact stresses are likely to occur under such conditions. Sheared and fragmented WC grains surrounded by adhered W can be seen in Region 3 (Figure 3.65a).

Further XEDS analysis of this region not only reveals loss of Co binder but also an increase in oxygen content in the WC grains in the near-surface region (see Figure 3.65b). Single-point spectrum scans also confirm a more than doubled concentration of oxygen in the WC grains closest to the adhered W compared to the adjacent WC grains (see Figure 3.66a–b). Oxidation wear mechanisms are also present in the degradation of CC tools [76]. Oxidation also affects the mechanical properties of cemented carbide [108-110], enabling an increase in cracking and fracturing of WC grains.

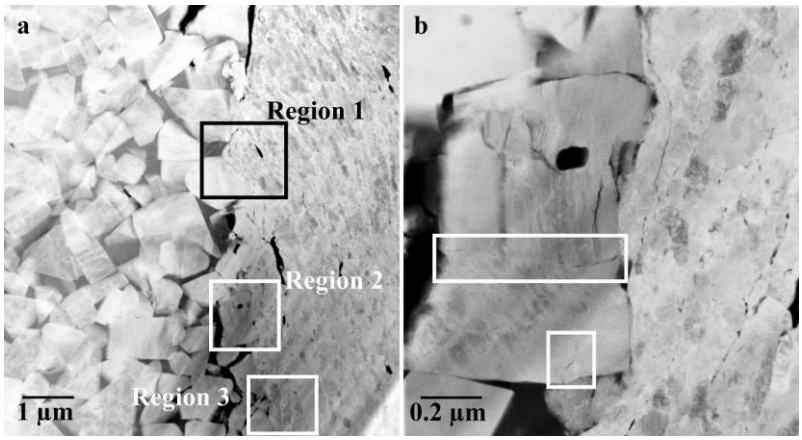

Figure 3.64. (a) HAADF-STEM image of interface between the flank wear land and adhered W where three regions of interest are shown; (b) detailed view of Region 2 where crack initiation in WC grains is highlighted.

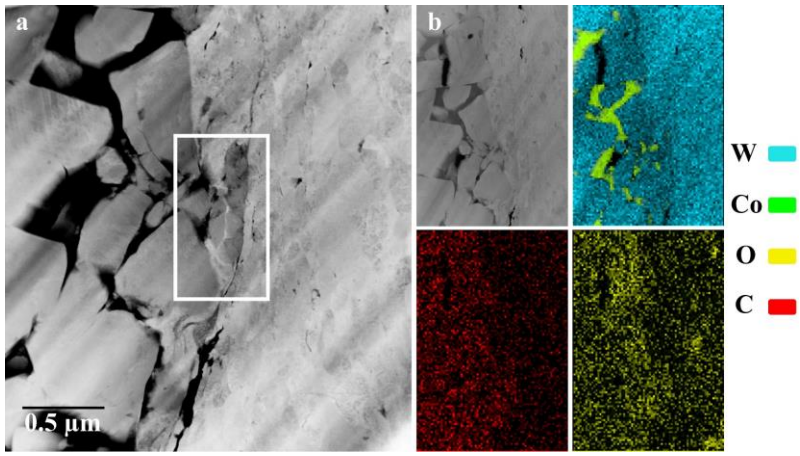

Figure 3.65. (a) HAADF-STEM image of Region 3 under increased magnification, showing fragmented WC grains; (b) XEDS map of Region 3 showing loss of Co and ingress of oxygen in the WC grains closest to the tool surface.

As reported in section 3.4.1.2, the PVD TiAlN – TiSiN coated tool showed the best results of the CC tools. The tool has limited adhesion of W further up on the rake as was the case with uncoated carbide tools. Moreover, the worn WC grains in the crater of the rake are smoother in appearance compared to those in uncoated CC tools. This can be explained by the difference in microstructure, with the PVD-coated tool having ultrafine grains and a higher toughness than the uncoated tool. This, in combination with the presence of microscopic grooves along the chip flow direction, implies that the major wear mechanisms are diffusion and abrasion.

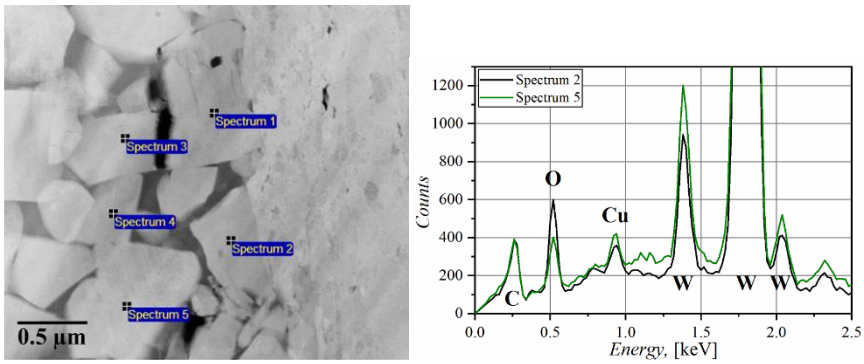

Figure 3.66. (a) STEM image of tool-workpiece interface with marked XEDS point analysis of WC grains; (b) Spectrum 2 and 5, showing increased O content in the surface WC grains.

As with the CC tools, microgrooves were seen on the flank on the minor cutting edge of the CBN200 tool, indicating an abrasive wear mechanism. As was reported in section 3.4.1.2, adhered BUE was present on the tool nose protecting the edge line underneath from abrasion and diffusion wear. The CBN 200 tool was cross-sectioned with wire-EDM, polished and subjected to analysis by SEM microscopy. Further XEDS analysis of the tool–BUE interface shows a gradual decrease in the concentration of boron and nitrogen starting from ~0.3 µm implying the diffusion of these elements into the adhered W. The concentration of boron and nitrogen drops to a negligible level about 0.2–0.3 µm into the adhered W (see Figure 3.67a–b). This information confirms that a diffusional mechanism together with abrasion causes tool wear on the cBN tool.

Figure 3.68 shows that grooves were found on the minor cutting edge of the PCD tool for most of the tools tested. SEM images reveal an interesting area of difference in contrast between Co pools on the rake, dividing the tool from the area inside the worn crater to the area outside of the contact zone, as shown by the dashed

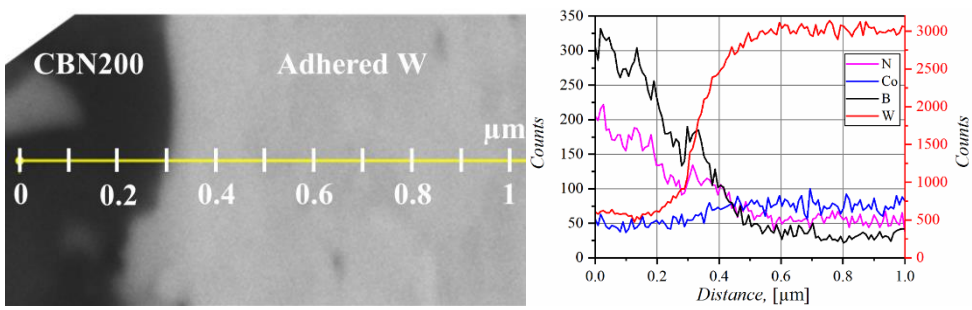

Figure 3.67. (a) SEM image and superimposed XEDS line scan across the interface between CBN200 and adhered W; (b) XEDS line scan data showing diffusion of nitrogen and boron from the tool into the adhered W.

separation line in Figure 3.68b. The increased contrast of the pools inside the crater indicates that the Co binder has been replaced by W (Figure 3.68c). Further analyses of a TEM lamella and STEM (HAADF-STEM) data (Figure 3.69a) show that diffusional dissolution of Co occurs as W covers the top layer of the Co pools. The same was seen for the PVD-coated CC tool in Region 1 (Figure 3.64a). The increased magnification in Figure 3.69b shows that the W grains are deformed in the chip flow direction. Moreover, there is also diffusion of the diamond grains, but at a lower rate. This explains the higher performance of the PCD tools compared to the PVD-coated CC tools where dissolution of WC and Co takes place at similar rates [76]. As a result of diffusional removal of Co, the PCD tool can potentially suffer from flaking and microchipping [111].

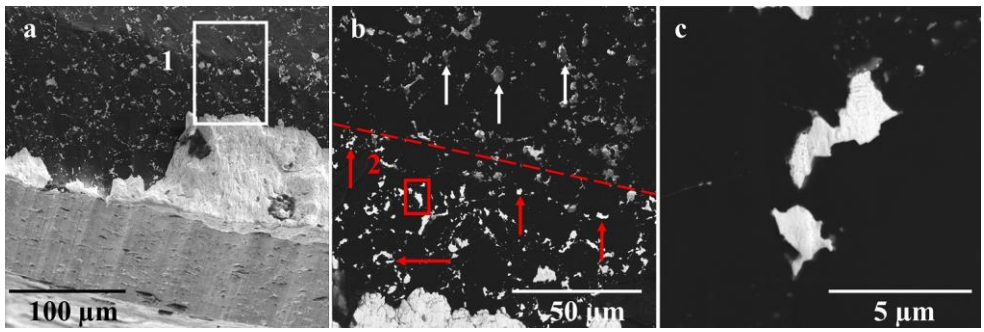

Figure 3.68. (a) Backscatter electron image showing the details of flank wear and cratering of a PCD tool (v_c = 195 m/min); (b) details of Z contrast between unaffected Co grains (white arrows) and grains affected by adhered W (red arrows); (c) increased magnification of a binder pool where Co is replaced by adhered W.

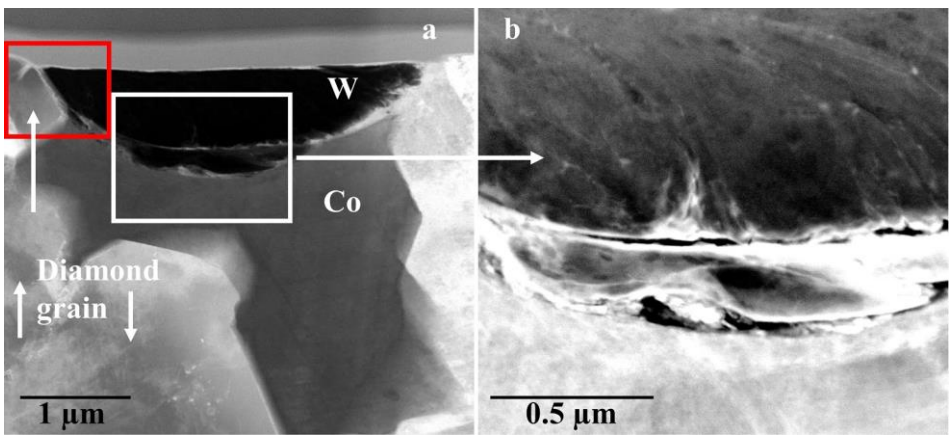

Figure 3.69. (a) HAADF-STEM image of the sample showing a diffusional dissolution of Co grain (dark gray) by W (black area); (b) LAADF-STEM detailed view of deformation of W along the chip flow direction.

3.4.3 Wear management

The performance of the tools was gauged by measuring the total cutting length l (m) until the tool life criterion of maximal tool wear VB_{max} = 300 µm was reached. The machining tests were stopped at different stages to measure the wear progression using an optical light microscope.

3.4.3.1 Niobium

As stated in section 3.2, pure Nb is a soft and ductile material, which results in surface quality problems during machining. Surface quality analysis shows that acceptable surface roughness is achieved at $v_c \geq 280$ m/min, therefore machining tests in this section are conducted at v_c = 300 m/min. In this research, machining tests were mainly conducted using high pressure (HP) and flood coolant. However, surface quality and tool life during machining with LN_2 coolant was also evaluated. The reason for using LN_2 coolant was to determine whether it is possible to decrease the ductility of Nb during machining to improve the surface quality. Nb has a ductile to brittle transition temperature (DBTT) between -130 and -200 °C [112]. LN_2 has the potential to reduce the temperature to -196 °C, which could counteract the problems with excessive ductility.

The results from the tool wear tests are presented in Figure 3.70a. It is clear that the LN_2 coolant did not demonstrate any positive effect on the tool life compared to flood and HP machining. With LN_2 coolant, the tool reached a cutting length of l = 1800 m before tool life criterion VB_{max} = 300 µm was reached. For flood and HP coolant, the tool wear tests was stopped at the cutting length l = 3000 m when the flank wear had reached VB_{max} = 244 µm for flood and VB_{max} = 103 µm for HP coolant (see Figure 3.70b). The corresponding cutting forces also reflect the results of the tool wear. The cutting forces during LN_2 machining showed wide variation and a higher average force compared to the other two conditions. Adhesion of Nb was present on the rake and flank side of the tools for all cutting conditions. Nb behaved as a ductile material throughout the machining tests, even when LN_2 was applied, indicating that the DBTT was not reached.

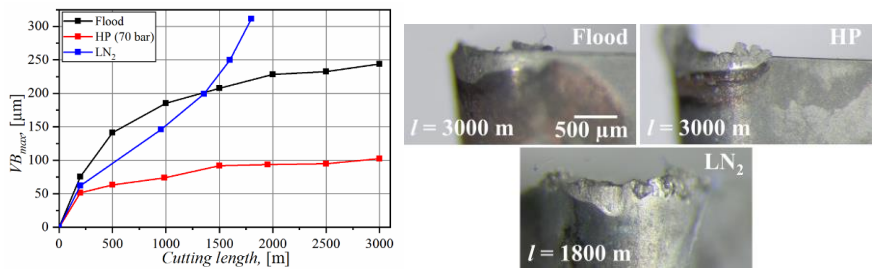

Figure 3.70. (a) Development of tool wear for different cooling strategies; (b) optical micrographs of worn tools at different cutting lengths.

3.4.3.2 Tungsten

Paper V reports on a large screening test during machining of W with HP coolant [76]. The ceramic and cermet tools tested showed sufficiently long tool life only at low cutting speed. Still, the best performing ceramics only reached a cutting length of l = 20 m. These tools were not selected for any extended tests.

Unlike the ceramic tools, CC tools showed the best results at higher cutting speeds. For the uncoated tool, the maximum cutting length was l = 10 m at cutting speed v_c = 125 m/min. However, for the PVD- and CVD-coated tools, the cutting length increased by more than three times compared to ceramics. The best performance was reached at v_c = 250 m/min for both of the tools. Further increase in cutting speed resulted in plastic deformation and breakage of the tool as shown by the X in Figure 3.71a–b.

The tool with lower cBN grade CBN010 had a cutting length comparable with the ceramics. This could be because of the similar matrix or reinforcement of the tool materials, resulting in similar wear progression. The CBN200 tool, which has a higher content of cBN and stronger metallic binder, showed increased wear resistance compared to CBN010 with ceramic binder. Unlike the CC tools, the wear resistance was better at lower cutting speeds (see Figure 3.72a). However, the resulting length was significantly lower than that of the PVD-coated tool.

The PCD tool had the best performance compared to the other tool materials at all tested cutting speeds. The tool wear is reduced at higher cutting speeds, and the best result was attained at v_c = 300 m/min with a cutting length l = 250 m (see Figure 3.72b).

The results of extended machining tests of the PVD-coated tool with alternative cutting conditions and coolant methods are reported in Paper VI. Cryogenic coolant, induction assisted machining (IAM), dry and flood coolant were evaluated and compared to the HP coolant.

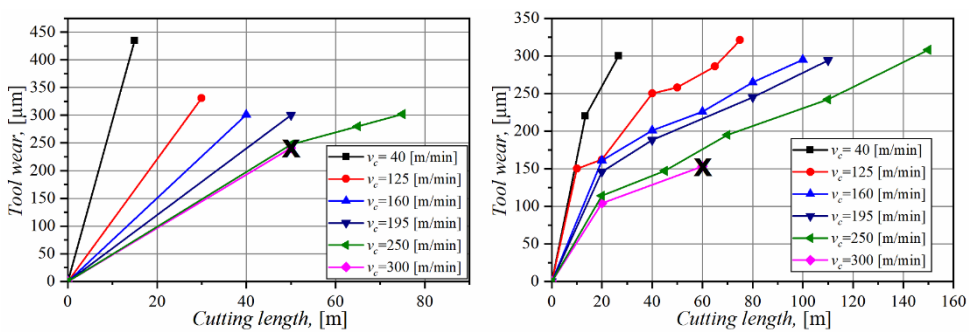

Figure 3.71. (a) Influence of the cutting speed on wear progression of TiCrN – Al_2O_3 – TiN-coated tool; (b) influence of the cutting speed of flank wear development of the TiAlN – TiSiN-coated carbide tool.

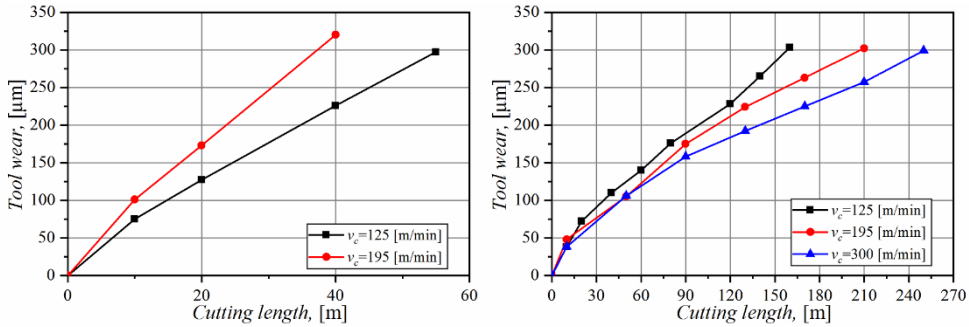

Figure 3.72. (a) Progression of tool wear of CBN200 at different cutting speeds; (b) evolution of tool wear of PCD at different cutting speeds.

Figure 3.73a shows that cryogenic machining increased the cutting length (l = 450 m), exceeding HP tests by ~450 % at v_c = 160 m/min. Cryogenic coolant shows better results at all the tested cutting speeds. However, at v_c = 195 m/min and above, the tool suffers from spontaneous breakage at different cutting lengths. The recorded cutting forces show variations during engagement of the tool, resulting in sudden drops in cutting forces. Adhesion of W and the formation of BUE on the tool are the most likely cause of the abrupt force variations (Figure 3.73b).

The literature mentions wear mechanisms such as fragmentation of WC grains [76] due to fatigue and impact by discontinuous brittle chips [111] as active wear mechanisms. The results presented above show that tool life increases with increased cutting speed, which indicates that an increase in process temperature slows down the tool degradation process. This can be explained by the DBTT, as the ductility of W increases in the temperature range 200–400 °C [113-116]. The W workpiece was preheated by induction heating to reach this temperature range.

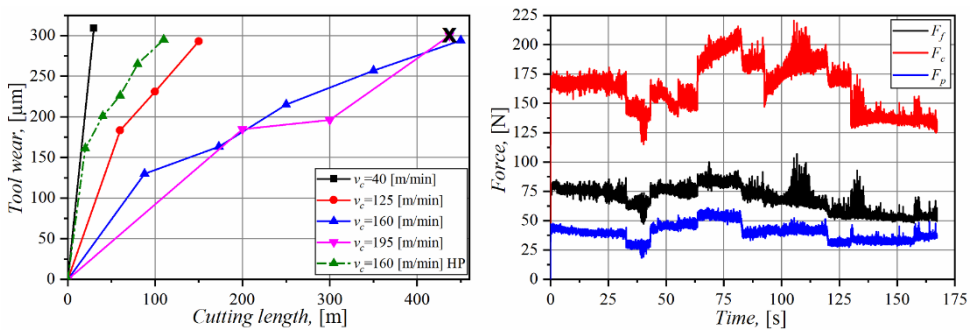

Figure 3.73. (a) Evolution of tool wear when machining with LN_2 at different cutting speeds and (b) cutting forces (v_c = 160 m/min).

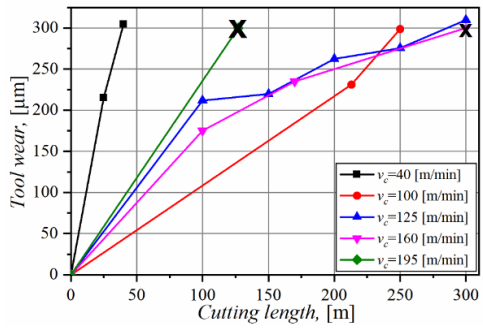

Figure 3.74. Evolution of tool wear when hybrid induction-assisted machining of W at different cutting speeds.

Figure 3.74 shows that a cutting length of l = 300 m was reached at cutting speeds v_c = 125 and 160 m/min with hybrid IAM process. However, at cutting speeds of v_c = 160 m/min and above, spontaneous breakage occurred. The recorded cutting forces were ~70 % lower and did not fluctuate as with cryogenic machining. The reduction in cutting forces may be the result of a reduction in material strength due to preheating.

The best performance of each of the five tested machining strategies at their respective cutting speeds is summarized in Figure 3.75a. When machining under dry conditions, the cutting length was similar to that at the IAM heated condition. However, the best result was achieved when the cutting speed was one step higher (see Figure 3.75a–b). Similar cutting lengths were also achieved for HP and flood coolant. The results obtained using the different machining strategies show that the best cutting speed increases from IAM heated machining to HP coolant, if LN_2 coolant is excluded (see Figure 3.75b). When the cutting speed is further increased, plastic deformation of the CC tools occurs in all of the machining strategies.

The best machining performance was found at the highest and lowest process temperatures, which can be linked to the DBTT. Previous research on cryogenic machining of porous W showed enhanced tool life due to the brittle behavior of the workpiece [107, 117]. As seen in Figure 3.73a, during cryogenic machining and for all other machining strategies, the best results are found at the highest possible cutting speed before tool breakage. However, the cryogenics results contradict the results from the other machining strategies about the benefit of a higher process temperature. Explanations for this phenomenon based on earlier observations of oxidation of WC grains can be negated as the use of LN_2 which creates a protective nitrogen atmosphere and prevents the oxidation wear process. If this is the case, then the results showing an increase in cutting length with increased cutting speed due to

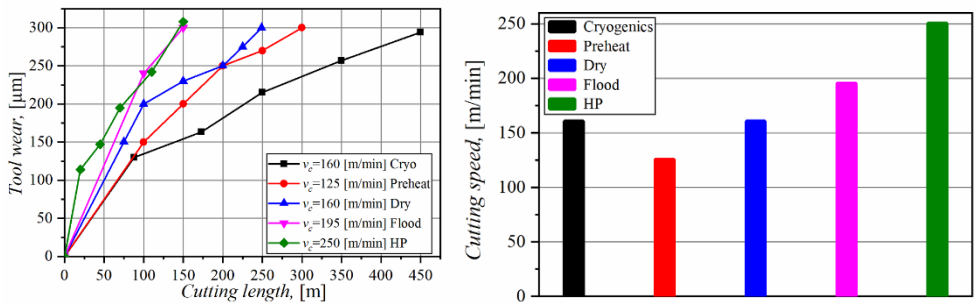

Figure 3.75. (a) Summary of tool wear for each of the machining strategies at respective best performance cases and cutting speeds; (b) cutting speed at which best machining performance is achieved for each cutting strategy.

higher process temperature are correct. This also explains why IAM, with the highest possible process temperature, followed by dry machining, have been found to result in the best performance in terms of tool life compared to HP machining. At elevated temperatures, there is a decrease in hardness and increase in the ductility of the W workpiece. An increase in ductility also affects the chip formation: preheating the workpiece up to 350 °C results in long continuous chips, while at 200 °C the chips are shorter (see Figure 3.76). Machining with coolant or LN_2 results in even smaller dust-like chip formation or smaller fragments. Furthermore, an increase in the adhered layer of W or BUL on the tool surfaces can be seen on the tools machined at higher process temperatures, thus slowing down the diffusion rate [76].

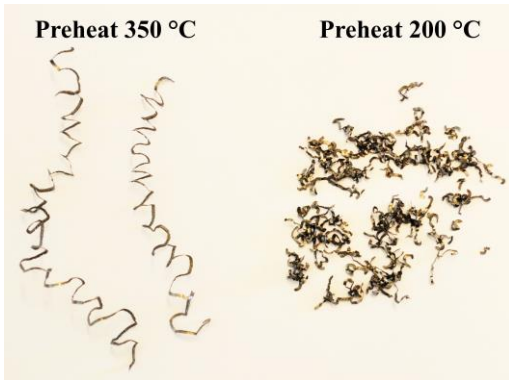

Figure 3.76. Chip morphology for machining with different induction-assisted preheating temperatures.

4 Summary and Conclusions

The following chapter summarizes the six papers appended to this thesis. The main objective of this work has been to investigate the wear mechanisms of different tooling solutions and obtain relevant cutting parameters for machining selected workpiece materials. Surface integrity parameters related to material properties were also studied to find ways to increase the quality of the machined surface and products. The conclusions of the results from the appended papers are presented. The last subsection suggests future research.

4.1 Summary of Appended Publications

The influence of process parameters on the resulting surface quality and the impact of wear mechanisms on tool life were investigated for several single-phase materials (SPM) materials. Paper I studied the influence of feed on the tensile properties of OFC. The influence of feed and cutting depth on burr formation of OFC were further investigated in Paper II. Different aspects of surface integrity and related surface quality during machining of Nb and W were examined in Papers III and VI. Wear mechanisms during machining Nb and W were studied in Papers IV and V.

4.1.1 Paper I

Tensile test rods of OFC ≥ 99.95 % were machined by longitudinal turning with different cutting parameters in order to investigate the influence of feed on material properties. In addition to tensile tests, SEM imaging observations and nanoindentation hardness tests were performed to measure the process-induced subsurface deformation. The results show an increase in yield strength of up to 55 % and increased work hardening depth with increased feed. The correlation coefficient between subsurface deformation and tensile properties was R = 0.983. The results show that it is possible to control the degree of subsurface deformation by careful control of the cutting parameters during machining.

4.1.2 Paper II

This paper deals with radial burr formation during longitudinal turning of OFC ≥ 99.95 % with different cutting parameters. The influence of depth of cut, feed, and major cutting edge angle on radial burr formation is presented. In addition to machining tests with variations in cutting data, FE simulations were performed for further comparison. The results show a decrease in radial burr formation with a decrease in depth of cut and major cutting edge angle together with a feed of $f = 0.2$ mm/rev. Machining tests and FE simulations showed similar results with an increase in burr height with increased cutting depth. However, the influence of feed needs further analysis. High-speed filming during machining tests revealed a five-stage cycle of burr formation.

4.1.3 Paper III

A screening test of six different tooling solutions during longitudinal turning of Nb ≥ 99.7 % was performed. Different grades of CVD, single-crystal and PCD diamond, PcBN, and also uncoated and coated cemented carbide tools were tested. The best tooling solutions were PCD and TiAlN –TiSiN coated CC, and the performance of these tooling solutions was further analyzed in terms of surface integrity and surface quality. Surface defects and subsurface deformations were analyzed using SEM imaging and nanoindentation. Despite showing the best results in terms of lower surface roughness (R_a) and fewer surface defects, PCD could not be recommended due to a higher degree of tool wear and subsurface deformation. TiAlN – TiSiN coated CC showed satisfying results in terms of surface finish and a lower degree of tool wear at a cutting speed of $v_c \geq 150$ m/min.

4.1.4 Paper IV

Tool wear development and wear mechanisms were evaluated for longitudinal turning of Nb ≥ 99.7 %, with uncoated CC tools. Experimental tests were supplemented by a diffusion couple experiment under high pressure and high temperature conditions. SEM and TEM microscopy reveal diffusion of carbon from WC and formation of NbC in the interface between the niobium and the cemented carbide. Electron microscopy of the worn tool showed rapid flank wear due to diffusional mechanism. The formation of an NbC layer on the rake acting as a tool protection layer that inhibits further tool degradation was also identified. Thermo-Calc calculations and DICTRA simulations were used for thermodynamic evaluation of the diffusion couple sample. The diffusion couple further revealed an interaction that involved formation of WC nanoplatelets in Co and the Co_3W_3C (M_6C type) η – phase.

4.1.5 Paper V

A screening test of eleven different tooling solutions including ceramics, coated and uncoated CC, cermet, PcBN, and PCD during longitudinal turning of 99.95 % W rod was conducted. Seven of the tooling solutions suffered from excessive tool wear or breakage. The tool wear mechanism and surface quality of the two tools showing the best results (PCD and TiAlN – TiSiN coated CC) were further analyzed. Scanning and transmission electron microscopy of the worn-out CC tool revealed the presence of abrasion, oxidation, and cracking of WC grains, and diffusional dissolution of WC and Co. The main wear mechanism identified for the PCD tool was abrasion and diffusional dissolution. The surface quality was generally poor with the presence of BUE, cracking, and adhesion of W on the machined surface.

4.1.6 Paper VI

Machining performance, including tool wear and surface quality, was studied for W ≥ 99.95 % and Nb ≥ 99.7 % during longitudinal machining in different cutting conditions and machining strategies with CC tools. The impact of the ductile to brittle transition temperature on the machinability of the workpiece materials was analyzed by cooling with LN_2 and by preheating with induction heating. Use of LN_2 had a positive effect on tool life, showing the best results at cutting speed v_c = 160 m/min. The next best results for machining W were preheating, dry, and flood/high-pressure coolant. However, the surface quality of the machined surface is generally poor in every cutting condition. High-pressure coolant showed the best results in terms of lower tool wear when machining Nb. LN_2 coolant did not have a positive effect on tool wear as in the case of machining W. Surface roughness in the range R_a = 0.4–0.6 µm was achieved at cutting speeds $v_c \geq 225$ m/min for both flood and high-pressure coolant with coated and uncoated CC tools.

4.2 Conclusions

Exploring and investigating the machinability of a material is a complex task including many different parameters related to the machining process, machining conditions, and tool and workpiece material properties. It is impossible to cover all aspects of machinability in one dissertation, even if concentrating on only one material. Selected SPMs with purity of 99.7% and above were the primary interest in this research. These materials are used in specialized sectors such as research facilities and in the nuclear and military industries. The materials studied are known to be very ductile (Cu and Nb) or brittle (W), which has significant effects on machinability.

High demands to product surface integrity influenced the research performed in this thesis. Subsurface deformation and its connection to machining parameters were discussed in Papers I and III. Subsurface deformations were identified and analyzed using SEM microscopy and nanoindentation methods. The choice of feed and cutting speed were shown to influence the depth of subsurface deformation during machining. The choice of tooling solutions was also shown to influence the depth of work hardening, which can be related to a size effect between the edge radius of the tool and the thickness of the uncut chip. The deformation can be divided into a severe deformation zone where grain refinement occurs due to dynamic recrystallization and a deeper layer of deformation and work-hardening. Subsurface deformation is related to variations in material properties such as yield strength and elongation at breakage.

Machining OFC and Nb results in long continuous chips. If these are not effectively transported away from the cutting zone, they can start nesting around the workpiece and damage the surface. The chips can also re-weld on the surface as small fragments of material. Side-flow and tears were also present on the surface during machining of Nb. The frequency of these surface defects depends on the tools used during machining. In the case of Nb, surface defects appear to be less frequent when cutting with a PCD tool compared to a coated CC tool. Build up edge (BUE) is a different type of surface damage. It is commonly accepted that SPM is not prone to BUE. However, BUE was found on the surface during machining of Nb and W. Besides BUE formation, cracks and voids were present on the surface when machining W. Voids are expected because the density of the workpiece is only 95 %. However, these voids can act as a cracks initiators, linking voids together.

Tool wear mechanisms acting on the tool when machining Nb and W were analyzed in Papers IV, V, and VI. Diffusional and chemical wear mechanisms were present on the flank side of the tool when machining Nb. This interaction was also confirmed by analysis of diffusion couple samples. Adhesion of Nb was present on the rake and flank side of the tool, however, there was no sign of adhesive wear. Instead, the adhered Nb supported formation of a protective NbC layer by carbon diffusion from the WC, which protected the rake side from further wear. Although single-phase W is a brittle metal, adhesion of W was found in the form of build up layer (BUL) and BUE on the rake and flank side of the cutting tools. Depending on the tooling solution, the following active wear mechanisms affecting the tools were observed: abrasion, oxidation, diffusional dissolution of WC and Co, and cracking of WC grains.

Summarizing the research presented in this dissertation, the following answers can be given to the research questions previously stated:

RQ1. Can the parameter requirements related to surface integrity of components for radiation research facilities be met with conventional machining?

Cutting parameters and surface defects that influence the surface quality are discussed in Papers II, III, V, and VI. In terms of surface roughness, typical values for components with higher requirements range from R_a = 0.05–0.8 µm. The lowest values of surface roughness during machining Nb with flood and HP coolant are found at higher cutting speeds ($v_c \geq 225$ m/min) with coated and uncoated CC tools. The results show potential surface roughness values of $R_a \leq 0.4$ µm. Surface roughness values of $R_a \leq 0.4$ µm were consistently met during machining of OFC with uncoated CC tools with VCGT and DCGT geometry with low feed and small cutting depths. When manufacturing W components, the required R_a values are normally higher than for OFC and Nb components. Together with poor tool life, surface roughness results are significantly higher when machining W. In general, the results show values of surface roughness in the range of R_a 1.4–2.0 µm. It is possible to machine W components with conventional machining; however, the process is challenging and requires careful control.

RQ2. Is there a conventional machining strategy that allows refractory metals to be machined productively?

Machining refractory metals is associated with many different challenges, as discussed in this dissertation. In Papers III, IV, and VI, the machinability and tool life of cemented carbide tools were evaluated and shown to result in a reasonable tool life when producing Nb components. Furthermore, the results show longer tool life with HP machining compared to flood coolant. Today HP coolant is becoming a conventional method, as many new machines are equipped with the coolant supply technique. It is difficult to achieve a highly productive process for machining W due to the extremely high rates of tool wear. The results presented in Papers V and VI show that the best result achieved (VB_{max} = 300 µm) in terms of cutting length during conventional machining was l = 250 m with PVD TiAlN – TiSiN coated tool in dry cutting conditions. Such low tool life requires frequent stops or tool changes when machining W components. High dimensional accuracy will be difficult to achieve if a tool change is required during a single cutting operation.

RQ3. Can alternative machining strategies (e.g., advanced tooling, advanced cooling, and hybrid processes) overcome the limitations of conventional machining?

Advanced tooling solutions including PCD, PcBN, single-crystal diamond, and ceramics were evaluated in Papers III and V. Although there was a 70 % increase in tool life during machining of W with PCD tools, other advanced tooling solutions did not outperform conventional CC tools when evaluating tool life during machining of W and Nb with HP coolant. Trial tests of machining OFC with a single-crystal diamond tool showed great potential for surface roughness values below $R_a \leq 0.1$ µm, which is required for ultra-precision components. Alternative machining strategies for machining Nb and W were evaluated in Paper VI. The use

of LN_2 coolant does not improve tool life or surface roughness during machining of Nb. However, the use of LN_2 coolant or heating of the workpiece with induction assistance can prolong the tool life compared to conventional machining strategies when machining W. This may be related to the ductile to brittle transition temperature of refractory metals. At elevated temperatures, the hardness decreases and the ductility increases, resulting in longer tool life. When LN_2 is used, the nitrogen creates a protective atmosphere and prevents or slows down the oxidation wear process of the tool.

4.3 Future Research

It is very difficult to find published research about machining SPMs, especially niobium and tungsten. Knowledge about these materials is not very common in a normal machine shop or among tool manufacturers since the market is limited to a small section of advanced manufacturing in research facilities and nuclear or military industries. The research presented in this dissertation is a step toward a better understanding of how to machine these difficult-to-cut materials with high surface quality requirements and acceptable process performance .

Initial tests during machining of Nb and W focused on finding a tool material with a low tool wear rate and a resulting surface with high quality, mainly surface roughness. While a number of machining parameters were tested, there are still many other possible cutting parameters and variations to consider. The fact that the initial surface roughness target of $Ra \leq 0.4$ µm was met for OFC and Nb is a relevant information if further reductions are sought. The results showing the formation of a tool protective layer on the cutting tool could be of interest when exploring tool coatings suitable for machining Nb. Information on which tool wear mechanisms are acting on the tools could lead to a better understanding and selection of coatings when choosing a tooling solution. This, in combination with the information regarding machining W under different cutting conditions, would facilitate further optimization of the machining outcomes.

The experimental tests covered in this dissertation focused only on longitudinal turning and continuous machining. Other cutting methods such as milling, drilling, and threading have not been considered. Yet it is common that this variety of machining techniques to be involved when manufacturing a complex components. Major part of initial screening tests of milling and drilling in W have been conducted to support local manufacturing industries. However, these results have not yet been completely analyzed or prepared for publication.

Cost and production time optimization were not considered, yet they are of high interest for manufacturing industries. The discussion of machining parameters and

tool selection in this dissertation lays the basis for future optimization of production costs.

References

1. *Industrilandet Sverige - Fokus Industri*. 2014: IF Metall.
2. *Arbetskraftsdeltagande och sysselsättning*. 2020 2020-06-09 [cited 2020 12-07]; Available from: https://www.scb.se/hitta-statistik/temaomraden/jamstalldhet/ekonomisk-jamstalldhet/arbetskraftsdeltagande-och-sysselsattning/.
3. SCB. *Sveriges BNP*. 2020 2020-08-28 [cited 2020 12-07]; Available from: https://www.scb.se/hitta-statistik/sverige-i-siffror/samhallets-ekonomi/bnp-i-sverige/.
4. Dieter, G.E. and Bacon, D.J., *Mechanical metallurgy*. Vol. 3. 1986: McGraw-hill New York.
5. *World Machine Tool Survey.* Gardner Business Media Inc., Cincinatti, OH, USA, 2019.
6. *Economic & Statistical Toolbox second quarter.* Cecimo, European Association of the Machine Tool Industries and related Manufacturing Technologies, 2020.
7. Trent, E.M. and Wright, P.K., *Metal cutting*. 2000: Butterworth-Heinemann.
8. Immanuel, K., *Critique of pure reason*. 2013: Hardpress Limited.
9. C Montgomery, D., *Design and Analysis of Experiments*. 2012, John Wiley & Sons: Singapore.
10. Stephenson, D. and Agapiou, J., *Metal Cutting Theory and Practice Second Edition.* Journal of Manufacturing Engineering and Materials Processing, 2006. **68**.
11. Ståhl, J.-E. and Seco Tools, A.B., *Metal cutting: theories and models*. 2012: Lund Univ.
12. Vieregge, G., *Zerspanung der Eisenwerkstoffe*. Vol. 16. 1959: Verlag Stahleisen.
13. Shaw, M.C. and Cookson, J., *Metal cutting principles*. Vol. 2. 2005: Oxford university press New York.
14. Xu, L., Schultheiss, F., Andersson, M., and Ståhl, J.-E., *General conception of polar diagrams for the evaluation of the potential machinability of workpiece materials.* International Journal of Machining Machinability of Materials, 2013. **14**(1): p. 24-44.
15. Knight, W., *Application of the universal machinability chart to the prediction of machine tool stability.* International Journal of Machine Tool Design Research, 1968. **8**(1): p. 1-14.
16. Rao, R.V. and Gandhi, O., *Digraph and matrix methods for the machinability evaluation of work materials.* International Journal of Machine Tools & Manufacture, 2002. **42**(3): p. 321-330.

17. Thiele Jr, E.W., Kundig, K.J., Murphy, D.W., Soloway, G., and Duffin, B.J.S.t., *Comparative machinability of brasses, steels and aluminum alloys: CDA's universal machinability index.* 1990: p. 362-371.
18. Ezugwu, E. and Wang, Z., *Titanium alloys and their machinability—a review.* Journal of Materials Processing Technology, 1997. **68**(3): p. 262-274.
19. Ezugwu, E., Bonney, J., and Yamane, Y., *An overview of the machinability of aeroengine alloys.* Journal of Materials Processing Technology, 2003. **134**(2): p. 233-253.
20. Ezugwu, E., Wang, Z., and Machado, A., *The machinability of nickel-based alloys: a review.* Journal of Materials Processing Technology, 1999. **86**(1-3): p. 1-16.
21. Manna, A. and Bhattacharayya, B., *A study on machinability of Al/SiC-MMC.* Journal of Materials Processing Technology, 2003. **140**(1-3): p. 711-716.
22. Ghosh, S. and Rao, P.V., *Application of sustainable techniques in metal cutting for enhanced machinability: a review.* Journal of Cleaner Production, 2015. **100**: p. 17-34.
23. Taylor, F.W., *On the Art of Cutting Metals*. Vol. 23. 1906: American society of mechanical engineers.
24. Kronenberg, M., *Replacing the Taylor formula by a new tool life equation.* International Journal of Machine Tool Design Research, 1970. **10**(2): p. 193-202.
25. Colding, B.N., *The machining productivity mountain and its wall of optimum productivity*. 1980: Society of Manufacturing Engineers.
26. Colding, B., *A tool-temperature/tool-life relationship covering a wide range of cutting data.* CIRP annals, 1991. **40**(1): p. 35-40.
27. Archard, J., *Contact and rubbing of flat surfaces.* Journal of applied physics, 1953. **24**(8): p. 981-988.
28. Khrushchev, M. and Babichev, M., *Resistance to abrasive wear and the hardness of metals*. Vol. 15. 1953: US Atomic Energy Commission, Technical Information Service.
29. Burwell, J.J., *Survey of possible wear mechanisms.* Wear, 1957. **1**(2): p. 119-141.
30. Quinn, T., *Review of oxidational wear: Part I: The origins of oxidational wear.* Tribology International, 1983. **16**(5): p. 257-271.
31. Schultheiss, F., *On the Machinability of Ductile and Strain Hardening Materials-Models and Methods for Analyzing Machinability*. 2013: Lund University.
32. Davim, J.P., *Surface integrity in machining*. Vol. 1848828742. 2010: Springer.
33. Field, M. and Kahles, J.F., *Review of surface integrity of machined components*. 1971: Defense Technical Information Center.
34. Field, M., Kahles, J.F., and Cammett, J., *Review of measuring methods for surface integrity.* CIRP, 1972. **21**(2): p. 219-238.
35. ISO, *4287: Geometrical product specifications . Surface texture. Profile method. Terms, definitions surface texture parameters*. 1997, International Organization for Standardization, Geneva, Switzerland.

36. Kiessling, R. and Sandén, G., *Skärteknik.* Sveriges Mekanförbund, Stockholm, Sweden, 1980.
37. Ernst, H., *Machining of metals*. 1938: American Society for Metals.
38. De Chiffre, L., *Metal cutting mechanics and applications. DSc*. 1990, Thesis, Technical University of Denmark.
39. Jawahir, I. and Van Luttervelt, C., *Recent developments in chip control research and applications.* CIRP annals, 1993. **42**(2): p. 659-693.
40. Jawahir, I., Ghosh, R., Fang, X., and Li, P., *An investigation of the effects of chip flow on tool-wear in machining with complex grooved tools.* Wear, 1995. **184**(2): p. 145-154.
41. ISO:3685, *Tool-life testing with single-point turning tools*. 1993: International Organization for Standardization. Geneva. Switzerland.
42. Aurich, J.C., Dornfeld, D., Arrazola, P., Franke, V., Leitz, L., and Min, S., *Burrs—Analysis, control and removal.* CIRP annals, 2009. **58**(2): p. 519-542.
43. Pekelharing, A., *Why and how does the chip curl and break.* CIRP Annals, 1964. **12**(1): p. 144-147.
44. Blotter, P. and Gillespie, L., *The formation and properties of machining burrs.* Journal of Manufacturing and Science Engineering, 1976. **98**(1): p. 66-74.
45. Gillespie, L.K., *The formation and properties of machining burrs.* 1973.
46. Davis, J.R., *Copper and copper alloys*. 2001: ASM international.
47. Kuyucak, S. and Sahoo, M., *A review of the machinability of copper-base alloys.* Journal of Canadian Metallurgical Quarterly, 1996. **35**(1): p. 1-15.
48. *Material property data*. 2020 [cited 2020 11-11]; Available from: http://www.matweb.com/.
49. Hebda, J. and Chang, W. *Niobium alloys and high temperature applications*. in *Niobium science & technology: proceedings of the International Symposium Niobium*. 2001.
50. *Niob 101 Final*. 2011.
51. Bauer, W. *Fabrication of niobium cavities*. in *Proc. 1st Workshop RF Supercond., M. Kuntze, ed., Karlsruhe*. 1980.
52. Rieck, G.D., *Tungsten and its Compounds*. 2013: Elsevier.
53. Ramakrishnan, P., *Powder metallurgy: processing for automotive, electrical/electronic and engineering industry*. 2007: New Age International.
54. *Abaqus Theory Manual, Dassault Systémes, v6.12.*
55. Johnson, G.R. and Cook, W.H. *A constitutive model and data for metals subjected to large strains, high strain rates and high temperatures*. in *Proceedings of the 7th International Symposium on Ballistics*. 1983. The Netherlands.
56. Olsson, M., Persson, H., Agmell, M., Bushlya, V., and Ståhl, J.-E., *FE simulation and experimental verification of side-flow and burr formation in machining of oxygen-free copper.* Procedia CIRP, 2018. **72**: p. 1427-1432.
57. Burchenia, A., Lysakovs'kii, V., Gordeyev, S., Ivakhnenko, S., Kutsai, A., and Suprun, O., *Calculation of the temperature distribution at the HPHT growing of*

diamond single crystals in cells with two growth layers. Journal of Superhard Materials, 2017. **39**(3): p. 149-154.

58. Olsson, M., Lenrick, F., M'Saoubi, R., Larsson, H., Markström, A., Petrusha, I., Ståhl, J.-E., and Bushlya, V., *Study of wear mechanisms of cemented carbide tools during machining of single-phase niobium.* Wear, 2020: p. 203244.
59. Olsson, M., Akujärvi, V., Ståhl, J.-E., and Bushlya, V., *Cryogenic and hybrid induction-assisted machining strategies as alternatives for conventional machining of refractory tungsten and niobium.* International Journal of Refractory Metals & Hard Materials, 2021: p. 105520.
60. Hashimura, M., Chang, Y., and Dornfeld, D., *Analysis of burr formation mechanism in orthogonal cutting.* 1999.
61. Machado, A., Kaminise, A., Da Silva, M., and Ariza, R. *Study on burr formation in turning*. in *Proceedings of 17th COBEM Brazilian Congress of Mechanical Engineering, São Paulo, SP, Brazil*. 2003.
62. Toropov, A., Ko, S.-L., and Kim, B.-K., *Experimental study of burrs formed in feed direction when turning aluminum alloy Al6061-T6.* International Journal of Machine Tools & Manufacture, 2005. **45**(9): p. 1015-1022.
63. Toropov, A., Ko, S.-L., and Lee, J., *A new burr formation model for orthogonal cutting of ductile materials.* CIRP annals, 2006. **55**(1): p. 55-58.
64. Toropov, A. and Ko, S.-L., *A model of burr formation in the feed direction in turning.* International Journal of Machine Tools & Manufacture, 2006. **46**(15): p. 1913-1920.
65. Biermann, D. and Heilmann, M., *Burr minimization strategies in machining operations*, in *Burrs-analysis, control and removal*. 2010, Springer. p. 13-20.
66. Hong, S.Y., Ding, Y., and Ekkens, R.G., *Improving low carbon steel chip breakability by cryogenic chip cooling.* International Journal of Machine Tools & Manufacture, 1999. **39**(7): p. 1065-1085.
67. Abouelatta, O. and Madl, J., *Surface roughness prediction based on cutting parameters and tool vibrations in turning operations.* Journal of materials processing technology, 2001. **118**(1-3): p. 269-277.
68. Benardos, P. and Vosniakos, G.-C., *Predicting surface roughness in machining: a review.* International Journal of Machine Tools & Manufacture, 2003. **43**(8): p. 833-844.
69. Singh, D. and Rao, P.V., *A surface roughness prediction model for hard turning process.* The International Journal of Advanced Manufacturing Technology, 2007. **32**(11-12): p. 1115-1124.
70. Suresh, P., Rao, P.V., and Deshmukh, S., *A genetic algorithmic approach for optimization of surface roughness prediction model.* International Journal of Machine Tools & Manufacture, 2002. **42**(6): p. 675-680.
71. Wang, X. and Feng, C., *Development of empirical models for surface roughness prediction in finish turning.* The International Journal of Advanced Manufacturing Technology, 2002. **20**(5): p. 348-356.

72. Puhasmägi, V., *Finsvarvning med hårdmetall.* Licentiate Thesis, Department of Mechanical Enginnering, Lund University, 1973.
73. Ståhl, J.-E., Schultheiss, F., and Hägglund, S., *Analytical and experimental determination of the Ra surface roughness during turning.* Procedia Engineering, 2011. **19**: p. 349-356.
74. Olsson, M., Bushlya, V., Zhou, J., and Ståhl, J.-E., *Effect of feed on sub-surface deformation and yield strength of oxygen-free pitch copper in machining.* Procedia CIRP, 2016. **45**: p. 103-106.
75. Olsson, M., Persson, H., Bushlya, V., and Ståhl, J.-E., *Surface roughness and sub-surface deformation measurements in machining of niobium.* Procedia CIRP, 2018. **71**: p. 413-417.
76. Olsson, M., Bushlya, V., Lenrick, F., and Ståhl, J.-E., *Evaluation of tool wear mechanisms and tool performance in machining single-phase tungsten.* International Journal of Refractory Metals and Hard Materials, 2020. **94**.
77. Sadat, A. and Reddy, M., *Surface integrity of inconel-718 nickel-base superalloy using controlled and natural contact length tools. Part I: Lubricated.* Experimental mechanics, 1992. **32**(3): p. 282-288.
78. Sadat, A.B., *Surface characteristics of machined Inconel-718 nickel-base superalloy using natural and controlled contact length tools.* International Journal of Machine Tools & Manufacture, 1987. **27**(3): p. 333-342.
79. Zhou, J., Bushlya, V., and Ståhl, J.-E., *An investigation of surface damage in the high speed turning of Inconel 718 with use of whisker reinforced ceramic tools.* Journal of Materials Processing Technology, 2012. **212**(2): p. 372-384.
80. Zou, B., Chen, M., Huang, C., and An, Q., *Study on surface damages caused by turning NiCr20TiAl nickel-based alloy.* Journal of Materials Processing Technology, 2009. **209**(17): p. 5802-5809.
81. Kishawy, H. and Elbestawi, M., *Effects of process parameters on material side flow during hard turning.* International Journal of Machine Tools & Manufacture, 1999. **39**(7): p. 1017-1030.
82. Grzesik, W., Kruszynski, B., and Ruszaj, A., *Surface integrity of machined surfaces*, in *Surface integrity in machining*. 2010, Springer. p. 143-179.
83. Pawade, R., Joshi, S.S., Brahmankar, P., and Rahman, M., *An investigation of cutting forces and surface damage in high-speed turning of Inconel 718.* Journal of Materials Processing Technology, 2007. **192**: p. 139-146.
84. Sharman, A., Hughes, J., and Ridgway, K., *An analysis of the residual stresses generated in Inconel 718™ when turning.* Journal of Materials Processing Technology, 2006. **173**(3): p. 359-367.
85. Zhou, J., Bushlya, V., Peng, R.L., Johansson, S., Avdovic, P., and Ståhl, J.-E., *Effects of tool wear on subsurface deformation of nickel-based superalloy.* Procedia Engineering, 2011. **19**: p. 407-413.
86. Chen, Y.-T., Yeh, A.-C., Li, M.-Y., and Kuo, S.-M., *Effects of processing routes on room temperature tensile strength and elongation for Inconel 718.* Materials & Design, 2017. **119**: p. 235-243.

87. Guo, E., Xu, F., and Loria, E., *Effect of heat treatment and compositional modification on strength and thermal stability of alloy 718.* Superalloys 718, 625 various derivatives, 1991: p. 389-396.
88. Krook, M., Recina, V., and Karlsson, B., *Material properties affecting the machinability of Inconel 718.* Superalloys, 2005. **718**: p. 625-706.
89. Savaşkan, T. and Turhal, M.Ş.J.M.C., *Relationships between cooling rate, copper content and mechanical properties of monotectoid based Zn–Al–Cu alloys.* 2003. **51**(4): p. 259-270.
90. M'Saoubi, R., Axinte, D., Herbert, C., Hardy, M., and Salmon, P.J.C.A., *Surface integrity of nickel-based alloys subjected to severe plastic deformation by abusive drilling.* 2014. **63**(1): p. 61-64.
91. Bushlya, V., Zhou, J., Avdovic, P., and Ståhl, J.-E., *Wear mechanisms of silicon carbide-whisker-reinforced alumina (Al 2 O 3–SiC w) cutting tools when high-speed machining aged Alloy 718.* The International Journal of Advanced Manufacturing Technology Procedia CIRP, 2013. **68**(5-8): p. 1083-1093.
92. Arsecularatne, J., Zhang, L., and Montross, C., *Wear and tool life of tungsten carbide, PCBN and PCD cutting tools.* International Journal of Machine Tools & Manufacture, 2006. **46**(5): p. 482-491.
93. Bonifacio, M. and Diniz, A., *Correlating tool wear, tool life, surface roughness and tool vibration in finish turning with coated carbide tools.* Wear, 1994. **173**(1-2): p. 137-144.
94. Jawaid, A., Che-Haron, C., and Abdullah, A., *Tool wear characteristics in turning of titanium alloy Ti-6246.* Journal of Materials Processing Technology, 1999. **92**: p. 329-334.
95. Bushlya, V., Lenrick, F., Ståhl, J.-E., and M'Saoubi, R., *Influence of oxygen on the tool wear in machining.* CIRP Annals, 2018. **67**(1): p. 79-82.
96. Kaplan, B., Odelros, S., Kritikos, M., Bejjani, R., and Norgren, S., *Study of tool wear and chemical interaction during machining of Ti6Al4V.* International Journal of Refractory Metals & Hard Materials, 2018. **72**: p. 253-256.
97. Lindvall, R., Lenrick, F., Persson, H., M'Saoubi, R., Ståhl, J.-E., and Bushlya, V., *Performance and wear mechanisms of PCD and pcBN cutting tools during machining titanium alloy Ti6Al4V.* Wear, 2020: p. 203329.
98. Bushlya, V., Lenrick, F., Gutnichenko, O., Petrusha, I., Osipov, O., Kristiansson, S., and Ståhl, J.-E., *Performance and wear mechanisms of novel superhard diamond and boron nitride based tools in machining Al-SiCp metal matrix composite.* Wear, 2017. **376**: p. 152-164.
99. Bushlya, V., Johansson, D., Lenrick, F., Ståhl, J.-E., and Schultheiss, F., *Wear mechanisms of uncoated and coated cemented carbide tools in machining lead-free silicon brass.* Wear, 2017. **376**: p. 143-151.
100. Gutnichenko, O., Bushlya, V., Zhou, J., and Ståhl, J.-E., *Tool wear and machining dynamics when turning high chromium white cast iron with pcBN tools.* Wear, 2017. **390**: p. 253-269.
101. Bushlya, V., Bjerke, A., Turkevich, V., Lenrick, F., Petrusha, I., Cherednichenko, K., and Ståhl, J.-E., *On chemical and diffusional interactions between PCBN and*

superalloy Inconel 718: Imitational experiments. Journal of the European Ceramic Society, 2019. **39**(8): p. 2658-2665.

102. Borgenstam, A., Höglund, L., Ågren, J., and Engström, A., *DICTRA, a tool for simulation of diffusional transformations in alloys.* Journal of Phase Equilibria Diffusion, 2000. **21**(3): p. 269.
103. Poulachon, G., Bandyopadhyay, B., Jawahir, I., Pheulpin, S., and Seguin, E., *The influence of the microstructure of hardened tool steel workpiece on the wear of PCBN cutting tools.* International Journal of Machine Tools & Manufacture, 2003. **43**(2): p. 139-144.
104. Brandt, G., *Flank and crater wear mechanisms of alumina-based cutting tools when machining steel.* Wear, 1986. **112**(1): p. 39-56.
105. Goh, G., Lim, L., Rahman, M., and Lim, S., *Transitions in wear mechanisms of alumina cutting tools.* Wear, 1996. **201**(1-2): p. 199-208.
106. Shoja, S., Mortazavi, N., Lindahl, E., Norgren, S., Bäcke, O., and Halvarsson, M., *Microstructure investigation of textured CVD alumina coatings.* International Journal of Refractory Metals Hard Materials, 2020. **87**: p. 105125.
107. Schoop, J., Ambrosy, F., Zanger, F., Schulze, V., Balk, T., and Jawahir, I., *Cryogenic machining of porous tungsten for enhanced surface integrity.* Journal of Materials Processing Technology, 2016. **229**: p. 614-621.
108. Basu, S. and Sarin, V., *Oxidation behavior of WC-Co.* Materials Science Engineering, 1996. **209**(1-2): p. 206-212.
109. Casas, B., Ramis, X., Anglada, M., Salla, J., and Llanes, L., *Oxidation-induced strength degradation of WC–Co hardmetals.* International Journal of Refractory Metals Hard Materials, 2001. **19**(4-6): p. 303-309.
110. Voitovich, V., Sverdel, V., Voitovich, R., and Golovko, E., *Oxidation of WC-Co, WC-Ni and WC-Co-Ni hard metals in the temperature range 500–800 C.* International Journal of Refractory Metals & Hard Materials, 1996. **14**(4): p. 289-295.
111. Zhong, L., Li, L., Wu, X., and He, N., *Micro cutting of pure tungsten using self-developed polycrystalline diamond slotting tools.* The International Journal of Advanced Manufacturing Technology, 2017. **89**(5-8): p. 2435-2445.
112. Begley, R. and Bechtold, J., *Effect of alloying on the mechanical properties of niobium.* Journal of the Less Common Metals, 1961. **3**(1): p. 1-12.
113. Edstrom, C.M., Phillips, A.G., Johnson, L.D., and R.R, C., *Literature on fabrication of tungsten for application in pyrochemical processing of spent nuclear fuels*. 1980.
114. Hahn, G.T., Gilbert, A., and Jaffee, R.I., *The Effects of Solutes on the Ductile-to-brittle Transition of Refractory Metals*. Vol. 155. 1962: Defense Metals Information Center, Battelle Memorial Institute.
115. Olofson, C. and Boulger, F., *Machining of Superalloys and Refractory Metals*. 1961, BATTELLE MEMORIAL INST COLUMBUS OH DEFENSE METALS INFORMATION CENTER.

116. Schwartzberg, F., Ogden, H., and Jaffee, R.I., *Ductile-brittle transition in the refractory metals*. Vol. 114. 1959: Defense Metals Information Center, Battelle Memorial Institute.
117. Schoop, J., Ambrosy, F., Zanger, F., Schulze, V., Jawahir, I., and Balk, T., *Increased surface integrity in porous tungsten from cryogenic machining with cermet cutting tool.* Materials Manufacturing Processes, 2016. **31**(7): p. 823-831.

Printed by Media-Tryck, Lund 2021 NORDIC SWAN ECOLABEL 3041 0903

Department of Production and
Materials Engineering
Faculty of Engineering
Lund University
ISBN 978-91-7895-863-4